Multiloop Functional Renormalization Group Studies of Heisenberg Models on the Kagome Lattice

Julian Christoph Thönniß

Master Thesis

Ludwig-Maximilians-Universität München
Faculty of Physics

Supervised by
Prof. Dr. Matthias Punk

Munich, September 12, 2019

Mehrschleifige Funktionale Renormierungsgruppen-Studien von Heisenberg-Modellen auf dem Kagome-Gitter

Julian Christoph Thönniß

Masterarbeit

Ludwig-Maximilians-Universität München
Fakultät für Physik

Betreut von
Prof. Dr. Matthias Punk

München, den 12. September 2019

Abstract

In this thesis, we develop an algorithm for a multiloop functional renormalization group (mfRG) approach to the pseudo-fermion Heisenberg model on the Kagome lattice. This algorithm refines previous pseudo-fermion-fRG approaches by its generalization to multiloop corrections of arbitrary order. This can be used to compute an fRG flow that is independent of the choice of regulator which can substantially improve the quantitative reliability of fRG analyses. In the scope of this thesis, we use this algorithm to compute the phase diagram at $T = 0$ with nearest (J_1) and next-to-nearest neighbor (J_2) interactions in the one- and two-loop scheme. We find two spin liquid phases for $J_2 \approx 0$ and $J_1 \approx 0$, respectively, as well as four distinct magnetically ordered phases. By computing the magnetic susceptibility, we find indication that both spin liquid phases are Z_2 (gapped) spin liquids with an exponential decay of spin-correlations in real space. Our determined correlation length of $\xi = 1.1424$ lattice spacings for the spin liquid phase at the Heisenberg point is in excellent agreement with the literature values. Further, we investigate the effects of second-order corrections on the phase diagram and find that the phase boundaries from our (and other previous) one-loop-fRG studies are shifted towards the ones found in DMRG studies, making further investigations of higher order loop corrections very promising.

Contents

1 Introduction **7**

2 Theoretical Background **8**
2.1 Quantum Spin Liquids 8
2.2 Functional Renormalization Group 12
2.2.1 Generating Functional Approach 12
2.2.2 Multiloop Approach from Parquet formalism 15
2.3 Physical Model 17

3 Analysis **19**
3.1 Vertex Parametrization 19
3.1.1 System-specific Parametrization 19
3.1.2 Channel-specific Frequency Arguments 21
3.2 System-specific Loop and Bubble Functions 22
3.2.1 Loop Functions 23
3.2.2 Bubble Functions 24
3.3 Frequency Asymptotics 28
3.4 Symmetries 29
3.4.1 Symmetries of the 2- and 4-Point Vertex 29
3.4.2 Symmetries and Parametrization of the Kagome Lattice 33
3.5 Algorithmic Implementation 35
3.5.1 General Vertex 35
3.5.2 Bubble Functions 37
3.5.3 Vertex in Bubble Function 38

4 Results **42**
4.1 Numerical Results 44
4.1.1 One-Loop Results 44
4.1.2 Two-Loop Results 48
4.2 Discussion 51

5 Summary and Outlook **53**

6 Acknowledgement **54**

Appendices **55**

A Two-particle Vertex Flow Equations in the mfRG Scheme **55**

B Vertex Spin Parametrization **55**

C Derivation of Parametrized Bubble Functions in the t- and a-Channel **56**

D Numerical Consistency Checks **61**

7 Eigenständigkeitserklärung **67**

1 Introduction

A ubiquitous phenomenon in many branches of physics is the breaking of symmetries at low temperatures, the transition from the para- to the ferro-magnetic phase at the Curie temperature being one famous example in the context of magnetism. However, frustrated quantum magnets in which localized magnetic moments interact strongly, do not necessarily share this property and provide valuable insights into the physics of competing ground states and strongly correlated many body systems with unusual properties where, even at $T = 0$, strong quantum fluctuations persist and no symmetries are broken. These phases are called *spin liquids*.
Remarkably, spin liquid states support fractional excitations (such as *spinons* that carry spin $\frac{1}{2}$ but no charge), exhibit strong long-range entanglement and give rise to artificial gauge fields [2]. The lattice gauge theories decribing these states comprise many analogies to high energy physics, such as the Higgs mechanism and particle confinement as known from QCD [44].
The analysis of quantum magnets with competing ground states has seen numerous approaches on the analytical (e.g. large-N-expansion [43], mean-field approaches [52]) and numerical (e.g. DMRG [6], fRG [39]) side which have by now led to a good understanding and classification of spin liquid states. However, there remain open questions such as for the ground state of the spin-$\frac{1}{2}$ Heisenberg model on the Kagome lattice which we address in this thesis. Though most numerical studies seem to find evidence for a spin liquid ground state, there is still disagreement about its exact nature and the details of the phase diagram.
In this thesis, we turn our attention to these questions under use of the functional renormalization group (fRG). This method is ideally suited for quantum magnetic systems as it treats tendencies for magnetic order and disorder on an equal footing and is a priori not restricted to certain spacial dimensions. Though previous fRG studies of Heisenberg models have led to interesting results and have demonstrated the power of this technique [5, 16, 47], they have so far mostly been useful for qualitative analyses. The quantitative reliability of the standard fRG approach is limited due to its dependence on the choice of regulator that is introduced by hand. This dependence is the result of the so-called *one-loop approximation* - a truncation that is needed in order to render the flow equations solvable and with which one neglects the 6-point- and all higher-order vertices. Recently, a multiloop fRG scheme has been derived that overcomes precisely this issue and provides a framework that restores the regulator independence of the flow equations by adding corrections that mimic the effect of the 6-point vertex [22]. In this thesis, we implement this multiloop fRG scheme for the Kagome Heisenberg model (KHM) in the pseudo-fermion approach and explicitely compare the results of the one- and two-loop scheme.
It should be mentioned that previous pseudo-fermion fRG studies on the KHM have already derived and implemented effective flow equations for the 1-loop case [39, 47]. Moreover, the effect of two-loop corrections has been investigated on the square lattice in Ref. [42] but there has not yet been a systematic treatment of higher loop orders in the pseudo-fermion KHM.

This thesis is structured in the following way:
Chapter 2 is devoted to a review on the theoretical description of spin liquids, followed by a short conceptual overview over the functional renormalization group. We follow the reasoning from Ref. [23] to argue why it is important to go to higher loop orders in order to restore self-consistency and regulator-independence in the truncated flow equations and review the mfRG-scheme that is based on the parquet formalism and provides important corrections to the standard (truncated) fRG flow equations [22].
In **Chapter 3**, we present the analysis in the fRG scheme. We use the general vertex parametrization from Ref. [39] in order to derive bubble and loop functions which can be combined to reproduce the flow equations presented in Ref. [39] but contain additional important information that is vital for the implementation of higher loop orders. Furthermore, we adapt the high frequency parametrization from Ref. [54] to our system and present our algorithmic implementation of the pf-mfRG for the KHM that allows in principle to compute arbitrary loop orders.
Our physical results are presented in **Chapter 4**. We discuss our findings and relate them to previous research on this topic.
In **Chpater 5**, we summarize our findings and give an outlook to possible future applications of our algorithm.

2 Theoretical Background

Systems of localized spins with pairwise interactions offer a rich variety of phenomena and pose challenging questions which have attracted much attention during the past decades and to which possible answers have partly remained unaswered until today. The simplest quantum mechanical model describing the dynamics of interacting spins on a lattice is the Heisenberg model, given by the Hamiltonian:

$$\hat{H} = \sum_{ij} J_{ij} \vec{S}_i \cdot \vec{S}_j, \tag{1}$$

where $\vec{S}_i$ is the spin operator on lattice site i and J_{ij} are the exchange couplings.

Typically, one restricts J_{ij} to nearest neighbor, and maybe also to next-to-nearest neighbor interactions as sketched in Fig. 1 for the Kagome lattice. On this lattice, interesting effects emerge due to magnetic frustration. Magnetic frustration can either be the consequence of a spatial geometry (typically triangular-based structures) or of competing interactions that lead to a situation where it is impossible to find a spin configuration for the ground state that simultaneously minimizes the bond energies between all pairs of spins.

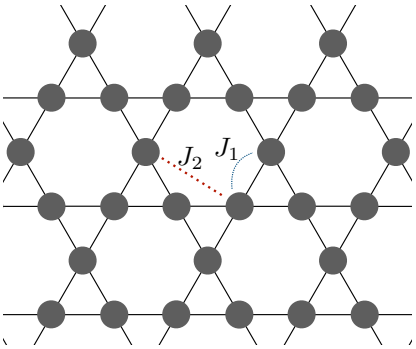

Fig. 1: The Kagome lattice is based on a corner sharing triangular geometry. The dotted lines denote nearest neighbor (J_1) and next-to-nearest neighbor (J_2) interaction between the spins residing on the lattice sites.

The simplest example for geometric frustration is the ferromagnetic Heisenberg interaction on a triangle with Ising spins on the corners as shown in Fig. 2. In this arrangement, not all spins can be aligned antiparallel which results in a six-fold degenerate ground state.
Generally, in systems where magnetic order is prevented in the ground state, the nature of the ground state can be very exotic, inluding phases of matter such as *spin liquids*; states that do not break any symmetries and exhibit long-range entanglement and fractional excitations [2, 44, 52].

Let us give a brief review on the theoretical description of spin liquids:

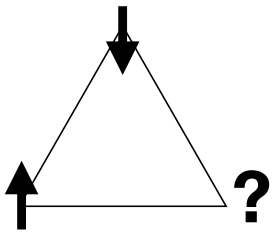

Fig. 2: Ising spins on the corners of a triangle as simple example for geometric frustration. No antiferromagnetic oder is possible. This geometry leads to a six-fold degenerate ground state [2].

2.1 Quantum Spin Liquids

Resonating Valence Bonds

A first step towards quantum spin liquids (QSLs) in the context of the spin-1/2 antiferromagnetic Heisenberg model (1) is the concept of valence bonds. Valence bonds are pairs of spins that are entangled such that they form a spin-0 singlet. The state where a lattice is completely covered with valence bonds, such that each spin is part of exactly one bond, is called valence-bond solid (VBS) and can be written as:

$$\prod_{i,j} \tfrac{1}{\sqrt{2}} \Big(|\uparrow\rangle_i |\downarrow\rangle_j - |\downarrow\rangle_i |\uparrow\rangle_j \Big), \tag{2}$$

where each site index appears exactly once. Importantly, VBS states spontaneously break the space-group symmetry whereas the Hamiltonian of which they are the ground state preserves the lattice symmetries [44]. The broken lattice symmetries can be restored by linearly superposing a broad distribution of different possible VBS states. These states have first been proposed by Anderson in 1973 and were dubbed *resonating valence bond* (RVB) states [1]. This idea is sketched on the triangular lattice in Fig. 3. The RVB state is the prototypical spin liquid and allows for an intuitive picture of fractionalized exciations: By flipping a single spin, which amounts to a $\Delta S = 1$ triplet excitation, one can break one singlet bond. As a consequence, one obtains two spins pointing in the same direction that can move as independent

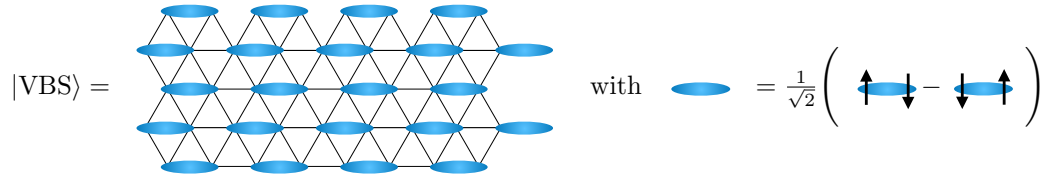

(a) Valence bond solid where the lattice is covered with spin-$\frac{1}{2}$ singlets. Lattice symmetries are broken in this state.

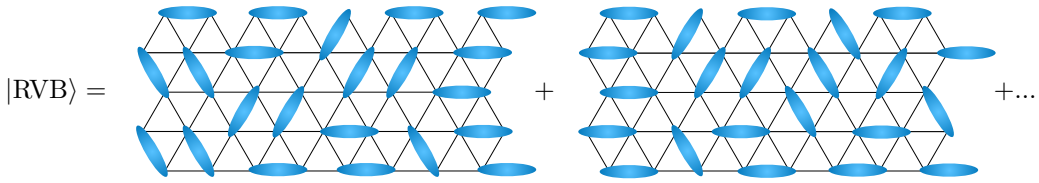

(b) Short range RVB state as superposition of all possible different singlet coverings. This state does not break lattice symmetries.

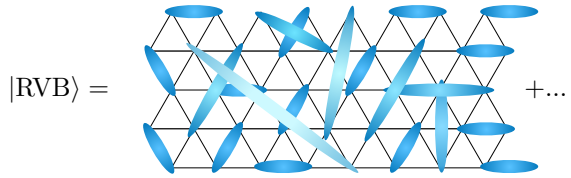

(c) Long range RVB state where singlets bonds are not restricted to nearest neighbors.

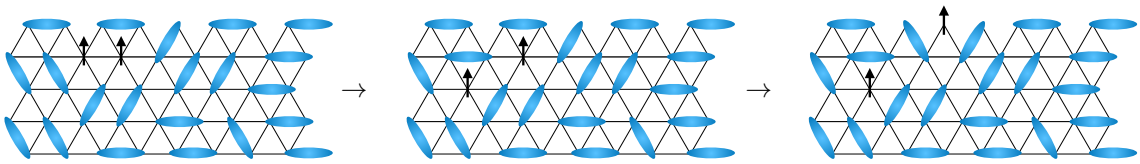

(d) Making a triplet exciation ($\Delta S = 1$) by flipping one spin breaks a singlet and creates two spinon excitations with spin $\frac{1}{2}$ but no charge that can move independently.

Fig. 3: Sketch of VBS and RVB states on the triangular lattice. Subfigure d) shows two spinons that result from a fractionalized $\Delta S = 1$ triplet excitation. Figure after Ref. [2].

exciations and carry spin $\frac{1}{2}$ but no charge, see Fig. 3d. These excitations are called *spinons* and are the result of a fractionalization of the triplet exciation.
The fact that valence bonds can be created in many different ways (in particular from short range and long range VBS states) makes it plausible that there are many different kinds of spin liquids on different lattice geometries.

Classification of Spin Liquids

One approach to their classification has been undertaken by Wen who developed a scheme to distinguish betwen different kinds of spin liquids by the type of gauge fluctuations that arise in the low-energy effective theories based on a mean-field approach [50–53]. The first step in constructing these mean-field theories is to rewrite the physical spin operators as product of "parton" operators that can either be fermionic or bosonic. In the fermionic case – the one that is used in this thesis –

the spin operators are written as:

$$\vec{S}_i = \tfrac{1}{2} \sum_{\alpha,\beta} \hat{c}^\dagger_{i,\alpha} \vec{\sigma}_{\alpha\beta} \hat{c}_{i,\beta}, \tag{3}$$

with $\sigma^\mu (\mu = 1, 2, 3)$ being the Pauli matrices. As a consequence of the parton-formulation, there is now a local $U(1)$ gauge redundancy in the physical spin operators: $\hat{c}_i \to \hat{c}_i e^{i\theta_i}$ [53]. Furthermore, it must be mentioned that the original Hilbert space containing only the states $|\uparrow\rangle$ and $|\downarrow\rangle$ is enlarged in the parton-formulation and consists now of four states:

$$\mathcal{H} = \{|\uparrow\rangle, |\downarrow\rangle\} \to \{|0\rangle, |\uparrow\rangle, |\downarrow\rangle, |\uparrow\downarrow\rangle\}.$$

The first and the last state are pure artefacts of the parton formulation and only the states with one fermion per site are physical. It is therefore necessary to enforce the contraint:

$$\sum_\sigma \hat{c}^\dagger_{i\sigma} \hat{c}_{i\sigma} = 1. \tag{4}$$

Consequently, the ground state $|\Psi_{\mathrm{MF}}\rangle$ of the mean-field Hamiltonian must be projected onto the subspace of physical states to yield a physical spin wave function. This projection is equivalent to including gauge fluctuations in the mean field theory which imposes condition (4) and delivers a valid low-energy effective theory of the spin liquid in which the gauge redundancy from the parton construction is implemented as gauge invariance [52, 53].

From this reasoning, Wen developed the *Projective Symmetry Group* (PSG) which serves as a classification scheme for different mean field approaches in this "parton"-formulation[1] and is defined as set of all transformations $G_X X$ that leave a specific mean field ansatz (e.g. $\chi_{ij} = \langle \hat{c}^\dagger_{i,\alpha} \hat{c}_{j,\alpha} \rangle$) invariant. Each such transformation is the combination of a symmetry transformation X, e.g. a lattice translation, combined with a corresponding gauge transformation G_X. It is precisely the gauge transformations G_X that allow to distinguish between different ansätze that share the same space-group symmetry: All elements of the PSG that are pure gauge transformations also form a group, called *Invariant Gauge Group* (IGG), that is associated with the gauge group that characterizes the spin liquid phase. Importantly, the PSG is a property of the mean field ansatz and is therefore independent of the Hamiltonian. If the corresponding mean field states are stable against fluctuations, this classification applies to real physical spin liquids [52]. Let us elucidate this point in more detail and present two types of spin liquids that will be important for our analysis:

U(1) and $\mathbf{Z_2}$ Spin Liquids

In this section, we outline how to obtain $U(1)$ and Z_2 spin liquid states from a mean field approach. The idea is to use the Higgs mechanism in order to break a $SU(2)$ lattice gauge theory down to a $U(1)$ or a Z_2 gauge theory that describes physical spin liquid states. We sketch only the idea and refer to Refs. [51–53] for details.

Writing the Heisenberg Hamiltonian in the parton-formulation yields (up to a constant):

$$H = \sum_{i,j} -\tfrac{1}{2} J_{ij} \Big(\hat{c}^\dagger_{i,\alpha} \hat{c}_{j,\alpha} \hat{c}^\dagger_{j,\beta} \hat{c}_{i,\beta} + \tfrac{1}{2} \hat{c}^\dagger_{i,\alpha} \hat{c}_{i,\alpha} \hat{c}^\dagger_{j,\beta} \hat{c}_{j,\beta} \Big). \tag{5}$$

In addition to the mean field ansatz $\chi_{ij}\delta_{\alpha\beta} = \langle \hat{c}^\dagger_{i,\alpha} \hat{c}_{j,\beta} \rangle$ introduced above, we define a pairing term, $\eta_{ij}\epsilon_{\alpha\beta} = -2\langle \hat{c}_{i,\alpha} \hat{c}_{j,\beta} \rangle$, that allows for the condensation of fermion pairs. Making the following definitions:

$$U_{ij} = \begin{pmatrix} \chi^\dagger_{ij} & \eta_{ij} \\ \eta^\dagger_{ij} & -\chi_{ij} \end{pmatrix} = U^\dagger_{ji} \qquad \text{and} \qquad \hat{\psi} = \begin{pmatrix} \hat{c}_\uparrow \\ \hat{c}_\downarrow \end{pmatrix},$$

one obtains the following Hamiltonian on the mean field level [52]:

$$H_{\mathrm{MF}} = \sum_{ij} \tfrac{3}{8} J_{ij} \Big[\tfrac{1}{2} \mathrm{tr}(U^\dagger_{ij} U_{ij}) - (\hat{\psi}^\dagger_i U_{ij} \hat{\psi}_j + h.c.) \Big] + \sum_i a^l_0 \hat{\psi}^\dagger_i \tau^l \hat{\psi}_i, \tag{6}$$

[1] However, the PSG classification is not exhaustive since there exist ansätze that fall in the same PSG-class but can give rise to different states upon variation of the parameters in the ansatz [52].

where the last term enforces the constraint $\langle\psi_i^\dagger\tau^l\psi_i\rangle = 0$ (which is equivalent to constraining the Hilbert space to one fermion per site on average). Here, $l = 1, 2, 3$, where τ^l are the Pauli matrices and a_0^l are Lagrange multipliers. This formulation has the great advantage that the invariance of the Hamiltonian under local $SU(2)$ gauge transformations W_i,

$$\hat{\psi}_i \to W_i\hat{\psi} \tag{7}$$

$$U_{ij} \to W_i U_{ij} W_j^\dagger, \tag{8}$$

becomes visible. In fact, this is a consequence of the parton formulation which has a $SU(2)$ redundancy that is more general than the above mentioned $U(1)$ gauge redundancy. Dropping the constant term in front and including phase fluctuations of U_{ij} around the mean field:

$$U_{ij} = \bar{U}_{ij}e^{ia_{ij}^l\tau^l},$$

one obtains the following Hamiltonian that describes spinons coupled to $SU(2)$ lattice gauge fields [51]:

$$H_{\mathrm{MF}} = \sum_{ij} -\tfrac{3}{8}J_{ij}(\hat{\psi}_i^\dagger\bar{U}_{ij}e^{ia_{ij}^l\tau^l}\hat{\psi}_j + h.c.) + \sum_i a_0^l\hat{\psi}_i^\dagger\tau^l\hat{\psi}_i. \tag{9}$$

Again, τ^l for $l = 1, 2, 3$ are the Pauli matrices. The 2×2 matrices $a_{ij}^l\tau^l$ describe the gauge fluctuations. Now comes the important point: To describe a physical spin liquid state, we need a way to construct a *stable* mean-field theory in which interactions induced by fluctations vanish at low energies. This can be achieved by giving the gauge fluctuations a finite gap through the Higgs mechanism which breaks the $SU(2)$ gauge structure down to a $U(1)$ or a Z_2 gauge structure, depending on the form of the mean field ansatz [44,53]. To understand this, it is helpful to first realize that the energy of a configuration is a function of the mean field ansatz U_{ij}, i.e. $E(\bar{U}_{ij}, e^{ia_{ij}^l\tau^l})$ [53]. Let us distinguish between two cases:

1. $\underline{\eta_{ij} = 0 \text{ and } \chi_{ij} \neq 0}$: In this case, one can choose: $\bar{U}_{ij} \propto e^{i\phi_{ij}\tau^3}$ [53]. Hence, the global $U(1)$ gauge transformation $e^{i\theta\tau^3}$ leaves the ansatz invariant whereas it is not invariant under $e^{i\theta\tau^{1,2}}$. The $SU(2)$ gauge structure is effectively broken down to a $U(1)$ gauge structure. Knowing that the energy must be gauge invariant and setting $a_{ij}^{1,2} = 0$ for the moment, one finds [53]:

$$E(\bar{U}_{ij}, e^{ia_{ij}^3\tau^3}) = E(\bar{U}_{ij}, e^{i(a_{ij}^3+\theta_i-\theta_j)\tau^3}),$$

   i.e. a_{ij}^3 transforms as $a_{ij}^3 = a_{ij}^3 + \theta_i - \theta_j$. A mass term $\propto (a^3)^2$ would be incompatible since it is not invariant under this transformation. Hence, this state has gapless $U(1)$ gauge fluctuations. In contrast, by writing down all terms for the energy that are compatible with gauge invariance and expanding to quadratic order in the a^l (we refer to Ref. [53] for details), one finds that a^2 and a^3 do acquire as mass such that these gauge bosons are gapped.

2. $\underline{\eta_{ij} \neq 0 \text{ and } \chi_{ij} \neq 0}$: In this case, it is not possible to choose a distinguished direction for the ansatz, such that the Higgs mechanism generates a mass for all a^l. The only gauge transformation that leaves the ansatz invariant is $W_i = -\tau^0$. The $SU(2)$ gauge structure has been broken down to a Z_2 gauge structure, i.e. the spin liquid state is gapped.

Let us only mention that the Higgs mechanism is realized here through the condensation of "$SU(2)$ gauge flux" which is defined as $P(C_i) = \bar{U}_{ij}\bar{U}_{jk}...\bar{U}_{li}$. The two above cases can just as well be distinguished in terms of this flux: If the flux for all possible loops with the basepoint i point in the same direction, e.g. $P(C) \propto \chi^0(C) + i\chi^3(C)\tau^3$, we have case 1 and the $SU(2)$ gauge structure is broken down to a $U(1)$ gauge structure. If different loops result in fluxes pointing in different directions, case 2 is realized and we obtain a Z_2 spin liquid.

Spin Liquids on the Kagome Lattice

The Kagome lattice (see Fig. 1) is a geometry that features strong geometric frustration due to its triangular corner-sharing structure combined with a small coordination number of 4 and it is therefore a promising candidate for a quantum spin liquid ground state. On the experimental side, the interest for spin liquids on the Kagome lattice was spurred by the synthesization of the mineral

herbertsmithite $ZnCu_3(OH)_6Cl_2$ in 2005 which is a perfect realization of the Kagome lattice with a strong spin-1/2 antiferromagnetic nearest neighbor interaction [46]. In addition to the Heisenberg interaction, it has an exchange anisotropy and Dzyaloshinkii–Moriya interaction which is a consequence of spin orbit coupling and comes from a broken mirror symmetry [10, 28]. Measurements of the magnetization in herbertsmithite show indeed no sign of magnetic order down to very low temperatures [46].

Though theoretical studies of pure Heisenberg systems on the Kagome lattice strongly support the hypothesis of spin liquid ground states for certain paramater regimes, there is still no consensus about their exact nature. Numerical analyses hint particularly at two possible types of spin liquids on the Kagome Heisenberg model (KHM) which are precisley the ones introduced in the previous subsection, namely:

- Z_2-spin liquid with a finite gap[2] and hence exponential decay of spin-correlations in real space [5, 6, 47, 50, 55],
- Gapless $U(1)$-Dirac-spin liquid with fermionic excitations and power-law decay of real space spin-corrrelations [11, 12, 14].

In this thesis, we are going to address the question for the ground state with the help of the functional renormalization group that we will briefly explain in the following section.

2.2 Functional Renormalization Group

2.2.1 Generating Functional Approach

In the analysis of strongly correlated systems in Condensed Matter Physics, one often deals with models where different physical phenomena and different types of collective excitations emerge on very different energy scales. The functional renormalization group (fRG) is a versatile framework to renormalize such theories which allows to analyze phenomena that are not accessible with standard perturbative methods in which all energy scales are treated at once which often leads to divergencies and unphysical results. Conceptually, fRG is closely related to the Wilson-RG approach in the sense that it is based on successively integrating out high energy degrees of freedom in order to obtain an effective low energy theory. However, instead of considering the flow of coupling constants, it allows to compute the flow of n-particle vertex functions, $\Gamma^{(n)}(\{\mathbf{k}_i\}, \{\omega_i\})$, with their full momentum and frequency dependence. In its exact representation, the fRG-flow is very compactly encoded in the *Wetterich equation*, a flow equation for a generating functional $\Gamma[\phi]$ called *effective action*. This functional differential equation being unsolvable in practice, it is is often times useful to expand it in the fields ϕ to obtain an infinite hierarchy of coupled first order differential equations for all n-particle vertex functions that is a good starting point for approximations. In the following, we will briefly sketch the conventional fRG approach (for computational details we refer to Refs. [3, 21, 29]) which will allow to motivate the multiloop fRG (mfRG) approach that has recently been been derived in the framework of the parquet formalism in Ref. [22] (see also Sec. 2.2.2) and that we implemented for our analysis.

Starting from the standard generalized many body action $S[\psi, \overline{\psi}] = -(\overline{\psi}, G_0^{-1}\psi) + V[\psi, \overline{\psi}]$ with Grassmann fields ψ and $\overline{\psi}$, we define the generating functional for connected Green's functions as:

$$\mathcal{G}[\eta, \overline{\eta}] = -\log\Big(\int \mathcal{D}[\overline{\psi}, \psi] e^{-S[\psi,\overline{\psi}]+(\overline{\eta},\psi)+(\overline{\psi},\eta)}\Big), \tag{10}$$

with $(\overline{\eta}, \psi) = \int_k \overline{\eta}_k \psi_k$ as notational simplification which implies integration over continuous and summation over discrete quantum numbers that are contained in the general multiindex k. This multiindex could for instance contain a fermionic Matsubara frequency ω, a momentum vector $\mathbf{k}$,

[2] Though finite, the gap is expected to be small in a potential Z_2-spin liquid: $\frac{\Delta}{J_1} < 0.17$ in Ref. [55], $\frac{\Delta}{J_1} = 0.13(1)$ in Ref. [6].

and a spin σ, i.e. $k = (\omega, \mathbf{k}, \sigma)$. The connected n-particle Green's functions for the fields ψ and $\overline{\psi}$ are given by

$$G^{(2n)}(k_{1'}, .., k_{n'}; k_1, .., k_n) = (-1)^n \frac{\delta^n}{\delta\overline{\eta}_{k_{n'}} ... \delta\overline{\eta}_{k_{1'}}} \frac{\delta^n}{\delta\eta_{k_n} ... \delta\eta_{k_1}} \mathcal{G}[\eta, \overline{\eta}]\Big|_{\eta=\overline{\eta}=0}. \tag{11}$$

Moreover, it is convenient to introduce new Grassmann fields ϕ and $\overline{\phi}$ that are defined by:

$$\phi = -\frac{\delta\mathcal{G}[\eta, \overline{\eta}]}{\delta\overline{\eta}} \qquad \overline{\phi} = \frac{\delta\mathcal{G}[\eta, \overline{\eta}]}{\delta\eta}. \tag{12}$$

From this, one can define the *effective action* $\Gamma[\phi, \overline{\phi}]$ as Legendre transform of $\mathcal{G}[\eta, \overline{\eta}]$:

$$\Gamma[\phi, \overline{\phi}] = (\overline{\eta}, \phi) + (\overline{\phi}, \eta) + \mathcal{G}[\eta, \overline{\eta}], \tag{13}$$

where $\eta[\phi]$ and $\overline{\eta}[\phi]$ depend on the Grassmann fields ϕ and $\overline{\phi}$ since they are determined by the inversion of Eq. (12). Importantly, the functional derivatives of $\Gamma[\phi, \overline{\phi}]$ that are defined in analogy to Eq. (11) – now with respect to ϕ and $\overline{\phi}$ – yield the one-particle irreducible vertex functions. These are related to the n-particle connected Green's functions by the generic properties of the Legendre transform which result in particular in the important relation:

$$\Gamma^{(2)}(k'; k) = \frac{\partial\Gamma[\phi, \overline{\phi}]}{\partial\overline{\phi}_{k'}\partial\phi_k}\bigg|_{\overline{\phi}=\phi=0} = G_0^{-1}(k'; k) - \Sigma(k'; k), \tag{14}$$

where Σ denotes the self energy and, for a systems with translation and spin rotation invariance, the bare propagator is given by

$$G_0(k'; k) = \frac{1}{i\omega - (\epsilon_{\mathbf{k}} - \mu)} \delta_{\omega\omega'} \delta_{\mathbf{k}\mathbf{k}'} \delta_{\sigma\sigma'}.$$

Here, $\epsilon_{\mathbf{k}}$ denotes the single particle energy and μ is the chemical potential.
More generally, one finds the reciprocal correspondence:

$$\underbrace{\begin{pmatrix} \frac{\partial^2\Gamma}{\partial\overline{\phi}_{k'}\partial\phi_k} & \frac{\partial^2\Gamma}{\partial\overline{\phi}_{k'}\partial\overline{\phi}_k} \\ \frac{\partial^2\Gamma}{\partial\phi_{k'}\partial\phi_k} & \frac{\partial^2\Gamma}{\partial\overline{\phi}_{k'}\partial\overline{\phi}_k} \end{pmatrix}}_{\mathbf{\Gamma}^{(2)}[\phi,\overline{\phi}]} = \underbrace{-\begin{pmatrix} \frac{\partial^2\mathcal{G}}{\partial\overline{\eta}_k\partial\eta_{k'}} & \frac{\partial^2\mathcal{G}}{\partial\overline{\eta}_k\partial\overline{\eta}_{k'}} \\ \frac{\partial^2\mathcal{G}}{\partial\eta_k\partial\eta_{k'}} & \frac{\partial^2\mathcal{G}}{\partial\overline{\eta}_k\partial\overline{\eta}_{k'}} \end{pmatrix}^{-1}}_{\left(\mathbf{G}^{(2)}[\eta,\overline{\eta}]\right)^{-1}}. \tag{15}$$

The effective action $\Gamma[\phi, \overline{\phi}]$ has a very distinct advantage over the action $S[\psi, \overline{\psi}]$: Since the original action $S[\psi, \overline{\psi}]$ is fixed by the microscopic model, its equations of motion for the fields ψ and $\overline{\psi}$ describe the classical dynamics of the system. In $\Gamma[\phi, \overline{\phi}]$ however, the quantum fluctuations have been fully accounted for and are therefore implicitly contained in all quantities that are derived from the effective action. It is thus clear that it is most convenient to formulate the flow equations in terms of $\Gamma[\phi, \overline{\phi}]$ in order to capture the quantum effects of the theory.
In order to introduce a scale dependence to the effective action, one implements an infrared cutoff in the bare Greens function $G_0^{(2)}(k'; k) \equiv G_0(k'; k)$ such that

$$G_0(k'; k) \to G_{0,\Lambda}(k'; k) \text{ with } \begin{cases} G_{0,\Lambda}(k'; k) = G_0(k'; k) & \text{for } \Lambda \to 0 \\ G_{0,\Lambda}(k'; k) = 0 & \text{for } \Lambda \to \infty. \end{cases} \tag{16}$$

There are different ways to implement a regulator that fulfills these conditions and in practice, the nature of the problem makes one or the other choice more favorable. One possibility is to introduce a mass term to the Greens function that suppresses the low energy modes:

$$G_{0,\Lambda}^{-1}(k'; k) = G_0^{-1}(k'; k) - f_\Lambda^{reg}(k'; k),$$

where $f_\Lambda^{reg}(k'; k)$ is a frequency or momentum-dependent regulator that can freely be chosen as long as the conditions in Eq. (16) are met. Another possibility (which we will use in our analysis) is a multiplicative regulator, e.g.:

$$G_{0,\Lambda}(k'; k) = \Theta(|\omega| - \Lambda) G_0(k'; k).$$

In principle, however, the exact flow equations are independent of the realization of the regulator and any regulator fullfilling Eq. (16) is valid.
Implementing a regulator automatically introduces a Λ-dependence to $\mathcal{G}_\Lambda[\eta,\overline{\eta}]$ and by Eq. (12) also to $\eta \to \eta_\Lambda$ and $\overline{\eta} \to \overline{\eta}_\Lambda$. Replacing all constituents of Eq. (13) by their scale dependent version and taking the derivative on both sides with respect to Λ yields the flow equation for $\Gamma_\Lambda[\phi,\overline{\phi}]$, the well-known *Wetterich equation*[3]:

$$\boxed{\frac{d}{d\Lambda}\Gamma_\Lambda[\phi,\overline{\phi}] = -\Big(\overline{\phi},(\tfrac{d}{d\Lambda}G_{0,\Lambda}^{-1})\phi\Big) - \frac{1}{2}\mathrm{tr}\left[(\tfrac{d}{d\Lambda}\mathbf{G}_{0,\Lambda}^{-1})\Big(\mathbf{\Gamma}_\Lambda^{(2)}[\phi,\overline{\phi}]\Big)^{-1}\right]}, \tag{17}$$

with

$$\mathbf{G}_{0,\Lambda}^{-1}(k';k) = \begin{pmatrix} G_{0,\Lambda}^{-1}(k';k) & 0 \\ 0 & -G_{0,\Lambda}^{-1}(k;k') \end{pmatrix}.$$

It is worth making the connection between $\Gamma[\phi,\overline{\phi}]$ and $S[\phi,\overline{\phi}]$ more precise in order to understand more intuitively what these objects mean:

At the initial energy scale of the flow Λ_0, where effects from quantum fluctuations are suppressed, the effective action reduces to the regularized bare action:

$$\Gamma_{\Lambda_0}[\phi,\overline{\phi}] = S_{\Lambda_0}[\phi,\overline{\phi}].$$

In the limit $\Lambda \to 0$, the effective action simply becomes the unregularized effective action since the regulator vanishes in this limit, i.e. $\Gamma_\Lambda[\phi,\overline{\phi}] \overset{\Lambda\to 0}{\longrightarrow} \Gamma[\phi,\overline{\phi}]$. Physically, variation of Λ thus corresponds to tuning between the regularized bare action and the unregularized effective action which describes the effective low energy theory sought-after[4].
It remains to insert the power expansion of the vertex functions,

$$\Gamma[\phi,\overline{\phi}] = \frac{(-1)^n}{(n!)^2}\sum_{\substack{k_1..k_n \\ k_{1'}..k_{n'}}} \Gamma_\Lambda^{(2n)}(k_{1'},...,k_{n'};k_1,...,k_n)\overline{\phi}_{1'}\cdots\overline{\phi}_{n'}\phi_1\cdots\phi_n, \tag{18}$$

and Eq. (15) into the Wetterich equation (the latter is necessary in order to handle the inverse vertex function on the right hand side). Identifying terms of equal power in the fields, one obtains a hierarchy of coupled flow equations for all n-particle vertex functions. With the definition of the *single scale propagator* S_Λ as

$$S_\Lambda = \frac{d}{d\Lambda}G_\Lambda\bigg|_{\Sigma=const.}, \tag{19}$$

they can graphically be represented as shown in Fig. 4.
In order to obtain a closed set of equations, it is necessary to truncate the hierarchy of flow equations at some order. In practice, already computation of the 6-point vertex, $\Gamma^{(6)}$, is beyond the numerically feasible which motivates the very widely used *one-loop approximation* in which the 6-point vertex in the flow equation for $\Gamma^{(4)}$ is left out and all flow equations for higher order vertices are neglected.

[3] To arrive at this compact result, it is essential to use the identities in Eq. (12). For a rigorous treatment in full detail, we refer in particular to Refs. [3, 21].

[4] In the literature, it is also common practice to define the flow equation in terms of the *average effective action* $\Gamma_\Lambda^{\mathrm{Wet}}[\phi,\overline{\phi}]$ (c.f. Ref. [3]) which is related to the effective action above by: $\Gamma_\Lambda^{\mathrm{Wet}}[\phi,\overline{\phi}] = \Gamma_\Lambda[\phi,\overline{\phi}] - (\overline{\phi},f_\Lambda^{reg}\phi)$ if a regulator f_Λ^{reg} is introduced as a mass term: $G_{0,\Lambda}^{-1} = G_0^{-1} - f_\Lambda^{reg}$. The functional $\Gamma_\Lambda^{\mathrm{Wet}}[\phi,\overline{\phi}]$ reduces to the unregularized bare action $S[\phi,\overline{\phi}]$ at the initial energy scale and thus tunes smoothly between the macroscopic action and the renormalized action at the end of the flow. However, this comes at the cost of a less natural definition of $\Gamma_\Lambda^{\mathrm{Wet}}[\phi,\overline{\phi}]$ which is no longer a simple Legendre transform of $\mathcal{G}_\Lambda[\eta_\Lambda,\overline{\eta}_\Lambda]$ as it was our case (c.f. Eq. (13)).

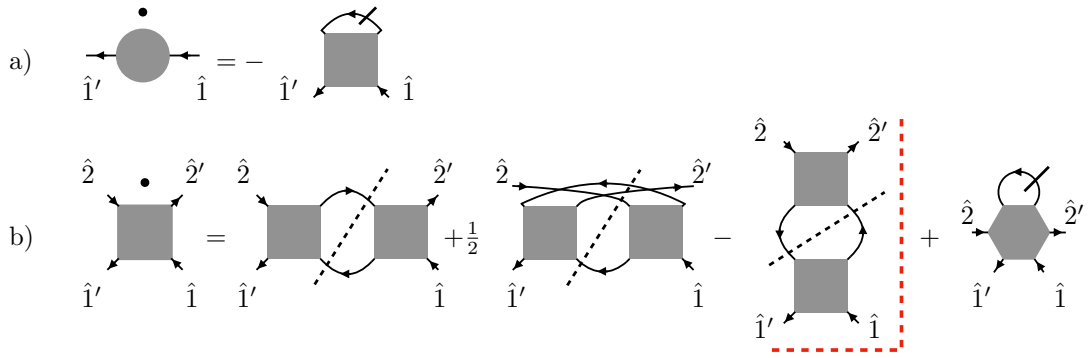

Fig. 4: Lowest order fRG flow equations. a) Self energy flow. The crossed fermion line represents the single scale propagator. b) Flow of the 2-particle vertex function. In the conventional *one-loop* approach, the hierarchy is truncated before the six-point vertex as indicated by the red line. The black dashed lines indicate that the two internal propagators are differentiated w.r.t. Λ at constant self energy, i.e. $\partial_\Lambda (G_\Lambda \cdot G_\Lambda)\Big|_{\Sigma=const.} = S_\Lambda \cdot G_\Lambda + G_\Lambda \cdot S_\Lambda$.

2.2.2 Multiloop Approach from Parquet formalism

The truncation described above is a necessary step to render the flow equations solvable. However, there is space for improvements that can partially compensate for the error introduced by the uncontrolled approximation of truncating the flow equations at order $n = 2$. In the literature, a very common approach for including corrections is the *Katanin substitution* which consists of adding a term to all differentiated propagators that mimics some of the higher order vertex contributions that are discarded by the truncation:

$$S_\Lambda \to \partial_\Lambda G_\Lambda = S_\Lambda + G_\Lambda (\partial_\Lambda \Sigma) G_\Lambda .$$

Although this leads to significant improvement in some cases, there remains a major issue in the RG-flow described by the truncated equations which prevents quantitative reliability of the data: The truncation destroys the total derivative that is present in the (exact) Wetterich equation. Consequently, the flow of $\Gamma^{(2)}$ and $\Gamma^{(4)}$ is no longer independent of the choice of regulator which is introduced by hand. The main advantage of the *multiloop fRG* (mfRG) approach is its ability to restore this total derivative on the right side of the flow equations. In the following, we will briefly sketch the derivation of the multiloop flow equations presented in Ref. [22], relate them to the one-loop equations and clarify their physical meaning.
The mfRG approach builds on the *parquet formalism* which provides a natural classification scheme for two-particle reducible (2PR) four-point vertices that is used to construct self consistent equations for general four-point vertices. The classification amounts to the identification of any possible two-particle-vertices either as reducible in a specific channel $r \in \{a, p, t\}$ or as two-particle-irreducible (2PI). The three two-particle-reducible channels are denoted as "a" (anti-parallel), "p" (parallel), and "t" (transverse) according to the way in which one needs to cut two internal fermionic lines to split the diagram into two parts. Moreover, the mfRG method used in this thesis is based on the approximation of the totally irreducible four-point vertex R as bare vertex, i.e. $R = \Gamma^0$, which is known as *parquet approximation*. The *parquet equations* for the two-particle vertex are very compactly stated as:

$$\Gamma = R + \sum_r \gamma_r , \tag{20}$$

$$I_r = R + \underbrace{\sum_{r' \neq r} \gamma_{r'}}_{\equiv \gamma_{\bar{r}}} , \tag{21}$$

$$\gamma_r = I_r \circ \Pi_r \circ \Gamma , \tag{22}$$

where γ_r (I_r) are all diagrams that are 2PR (2PI) in channel r and Π_r are two full propagators that connect two vertices such that they form a bubble that is 2PR in channel r. Starting from these relations, it is straightforward to introduce a scale dependence by replacing all propagators by their scale dependent version in the same manner as in Eq. (16). This results in a scale dependence of also all other constituents in the parquet equations besides the totally 2PI vertex $R = \Gamma^0$ (in the parquet approximation) which makes it safe to suppress all Λ-dependencies in the notation of the following. The parquet approximation is the only approximation that is made in the mfRG scheme and it is also the only input that one needs to specify at the beginning of the flow.
The last step towards the flow equations consists of taking the derivative with respect to the flow parameter Λ on both sides of Eq. (22). Carefully employing the Leibniz rule and reshuffling identities that result from differentiating also the other parquet relations [5], one arrives at a differential equations for γ_r:

$$\dot{\gamma}_r = \underbrace{\Gamma \circ \dot{\Pi}_r \circ \Gamma}_{\dot{\gamma}_r^{(1)}} + \underbrace{\dot{I}_r \circ \Pi_r \circ \Gamma}_{\dot{\gamma}_r^{(\mathrm{L})}} + \underbrace{\Gamma \circ \Pi_r \circ \dot{I}_r \circ \Pi_r \circ \Gamma}_{\dot{\gamma}_r^{(\mathrm{C})}} + \underbrace{\Gamma \circ \Pi_r \circ \dot{I}_r}_{\dot{\gamma}_r^{(\mathrm{R})}}, \tag{23}$$

and thus at the compactly written flow equation for the general vertex Γ:

$$\dot{\Gamma} = \sum_r \dot{\gamma}_r. \tag{24}$$

The right side of Eq. (23) can be constructed iteratively as shown diagrammatically in Fig. 24 in Appendix A. From Eq. (23), it becomes clear what the term "multiloop" precisely means in this context: It refers to the fact that one iteratively computes multiple higher order corrections to the flow equations which are separately all of the one-loop structure. These higher order contributions are important corrections that are missed with the conventional one-loop truncation as will become clear in the following.
In order to compute the bubbles in Eq. (23) at different values for Λ, it is necessary to gain knowledge about the evolution of the self energy Σ during the flow. Knowing the Schwinger-Dyson equation which relates the self energy to the two-particle-vertex,

$$\Sigma = -(\Gamma^0 + \Gamma^0 \circ \Pi_p \Gamma) \cdot G,$$

one can again find a flow equation by making all propagators (also those implicitly contained in Γ) scale dependent and then taking the derivative with respect to Λ on both sides. Although this is conceptually straight forward, casting the right side into a form that contains only known objects at a specific Λ during the flow becomes quite involved. Hence, we only state the result for the parquet approximation $R = \Gamma^0$ and refer to Ref. [22] for all details:

$$\dot{\Sigma} = \underbrace{[-\Gamma \cdot S]}_{\dot{\Sigma}_{\mathrm{std}}} + \underbrace{[-\dot{\gamma}_t^{(C)} \cdot G]}_{\dot{\Sigma}_{\bar{t}}} + \underbrace{[-\Gamma \cdot (G \cdot \dot{\Sigma}_{\bar{t}} \cdot G)]}_{\dot{\Sigma}_t}. \tag{25}$$

The first contribution is the standard term from the self energy flow that was derived in Sec. 2.2, whereas the last two contributions stem from the multiloop contributions in the vertex. The vertex $\dot{\gamma}_t^{(C)}$ was defined in Eq. (23). The diagrammatic representation of the flow equation is shown in Fig. 5.

[5] The derivation is explained in detail in Ref. [22]

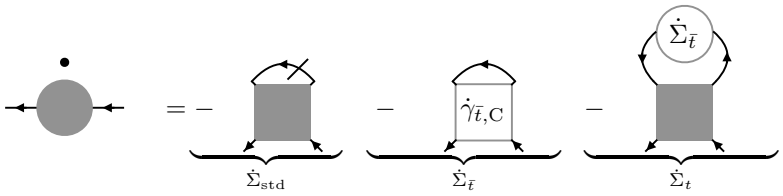

Fig. 5: Extended self energy flow in the mfRG scheme. The last two contributions are computed iteratively from the first self energy contribution and the vertex flow. The crossed fermion line in the first contribution represents the single scale propagator.

It is worth mentioning that there is a relation that connects the irreducible vertex of the t-channel, I_t, to a functional derivative of the self energy [22]:

$$\frac{\delta\Sigma}{\delta G} = -I_t.$$

Understanding variation with respect to the flow parameter Λ, one can rewrite this as an equation containing only regular partial derivatives:

$$\dot{\Sigma} = -I_t \cdot \dot{G} = -\Gamma \cdot S, \tag{26}$$

which is precisely $\dot{\Sigma}_{\mathrm{std}}$. However, solving this equation in the fRG flow is only consistent with the functional derivative if the expression on the right hand side of $\dot{\Sigma}$ constitutes a total derivative of diagrams which is not the case since the mfRG flow equations for Σ in the parquet approximation must also include contributions from $\dot{\Sigma}_{\bar{t}}$ and $\dot{\Sigma}_t$ that are missing in Eq. (26). In fact, in order to simultaneously satisfy the functional derivative relation and the Schwinger-Dyson-equation, one would require the exact solution. With the flow equation in Eq. (25), the self energy flows towards the Schwinger-Dyson solution computed with the parquet vertex, i.e. $R = \Gamma^0$ [22].
We stress that, as a result of the construction, the solution of the mfRG flow is equivalent to the parquet solution with $R = \Gamma^0$ [22]. The great advantage of mfRG as opposed to a direct parquet approach is the possibility to enter parameter regimes that are otherwise intractable as they lead to divergencies. In particular, we will also be interested in phase transitions at $\Lambda > 0$ which are never accessible with the direct parquet approach which is only equivalent to the mfRG result at $\Lambda = 0$.
Relating mfRG to the conventional one-loop-approach, one can understand the additional higher order corrections in the vertex and in the self energy flow equations as partial compensation for the diagrammatic contributions that are lost by performing the truncation. Most importantly, they restore the total derivative within the parquet approximation scheme which makes the flow independent of the choice of regulator.

2.3 Physical Model

Our model is given by the Heisenberg interaction in the pseudo-fermion representation, $S_i^\mu = \frac{1}{2}\sum_{\alpha,\beta} \hat{c}_{i,\alpha}^\dagger \sigma_{\alpha\beta}^\mu \hat{c}_{i,\beta}$:

$$\hat{H} = \sum_{i,j} J_{ij} \vec{S}_i \cdot \vec{S}_j = \sum_{\alpha,\beta,\gamma,\delta} \sum_{i,j} \frac{1}{4} \sigma_{\alpha\beta}^\mu \sigma_{\gamma\delta}^\mu J_{ij} \hat{c}_{i,\alpha}^\dagger \hat{c}_{i,\beta} \hat{c}_{j,\gamma}^\dagger \hat{c}_{j,\delta}. \tag{27}$$

Note that this Hamiltonian is particle-hole-symmetric. Using the anticommutation relation of the fermionic operators, $\{\hat{c}_{i,\alpha}^\dagger, \hat{c}_{j,\beta}\} = \delta_{i,j}\delta_{\alpha,\beta}$, to rewrite the Hamiltonian in its normal ordered form in the grand canonical ensemble, $\hat{H} - \sum_i \mu_i \hat{n}_i$ with $\hat{n}_i = \sum_\alpha \hat{c}_{i\alpha}^\dagger \hat{c}_{i\alpha}$, one obtains:

$$\hat{H} = \underbrace{\sum_{\alpha,\beta,\gamma,\delta} \sum_{i,j} \frac{1}{4} \sigma_{\alpha\beta}^\mu \sigma_{\gamma\delta}^\mu J_{ij} \hat{c}_{i,\alpha}^\dagger \hat{c}_{j,\gamma}^\dagger \hat{c}_{j,\delta} \hat{c}_{i,\beta}}_{H_{\mathrm{int}}} - \sum_{i,\alpha} \underbrace{\left(-\frac{3}{4} J_{ii} + \mu_i\right)}_{\equiv \tilde{\mu}_i} \hat{c}_{i,\alpha}^\dagger \hat{c}_{i,\alpha}.$$

The chemical potential μ_i must be tuned such that the condition:

$$\sum_{\alpha} \left\langle \hat{c}^{\dagger}_{i,\alpha} \hat{c}_{i,\alpha} \right\rangle = \langle \hat{n}_i \rangle = 1 \tag{28}$$

is met which imposes that every site is only singly occupied on thermodynamic average. This constraint is necessary due to the enlargement of the Hilbert space in the parton formulation (see Sec. 2.1). We will return to this matter in Sec. 3.2.1.

In the following diagrammatic derivations of the specific mathematical expressions that enter the fRG flow equations for the considered system, the signs and overall factors are to be understood with respect to the general many-body action:

$$S = -\sum_{\hat{1}\hat{1}'} \bar{c}_{\hat{1}'} \underbrace{G_0^{-1}(\hat{1}';\hat{1})}_{=G_0^{-1}(i\omega_1)\delta_{\hat{1}\hat{1}'}} c_{\hat{1}} - \frac{1}{4\beta} \sum_{\hat{1}',\hat{1},\hat{2}',\hat{2}} \Gamma^0(\hat{1}'\hat{2}',\hat{1}\hat{2}) \bar{c}_{\hat{1}'} \bar{c}_{\hat{2}'} c_{\hat{2}} c_{\hat{1}}, \tag{29}$$

where the multiindices with a hat include frequency, spin and a site index and the bare vertex[6] $\Gamma^0(\hat{1}'\hat{2}',\hat{1}\hat{2})$ is separately anti-symmetric under the exchange of $(\hat{1} \leftrightarrow \hat{2})$ and $(\hat{1}' \leftrightarrow \hat{2}')$. The absence of dispersion in the fermionic Hamiltonian results in a particularly simple form of the bare Greens function[7]:

$$G_0(i\omega) = \frac{1}{i\omega}.$$

Moreover, the two- and four-point Greens functions are defined as:

$$G^{(2)}_{\hat{1}\hat{1}'} = -\langle c_{\hat{1}} \bar{c}_{\hat{1}'} \rangle \tag{30}$$

$$G^{(4)}_{\hat{1}\hat{2}\hat{1}'\hat{2}'} = \langle c_{\hat{1}} c_{\hat{2}} \bar{c}_{\hat{2}'} \bar{c}_{\hat{1}'} \rangle . \tag{31}$$

In order to obtain the self energy and the four-point vertex, one needs to eliminate all disconnected diagram from Eqs. (30) and (31), respectively, and amputate the external legs.

The flow parameter Λ is introduced by a regulator in G_0. In our analysis, we wish to compute the phase diagram of the ground state, i.e. we perform all Matsubara sums in the limit $T \to 0$. Consequently, all Matsubara sums become integrals with continuous frequencies,

$$\frac{1}{\beta} \sum_{\omega} \xrightarrow{T\to 0} \int_{-\infty}^{\infty} \frac{d\omega}{2\pi},$$

which makes some regulators more tractable than others. Since the vertex functions are nested in the higher order corrections, sharp regulators result in integrands with many discontinuities which are numerically unfavorable. Hence, we use a smoothened version of the step function as multiplicative regulator:

$$G_{0,\Lambda}(\omega) = \left(1 - e^{-\left(\frac{|\omega|}{\Lambda}\right)^2}\right) G_0(\omega). \tag{32}$$

Since all analytical calculations are performed in the Matsubara formalism, we present all calculations in this thesis for the general case with sums over discrete Matsubara frequencies and take the limit $T \to 0$ only for the actual implementation.

We undertake our analysis on the Kagome lattice which is shown in Fig. 1. The spin operators of the original Heisenberg Hamiltonian (27) reside on the individual lattice sites and interact with energies J_1 for nearest neighbors and J_2 for next-to-nearest neighbors.

[6] In the following part of this thesis, the term *"vertex"* always refers to the *"two-particle vertex function"* unless specified differently.

[7] The Fourier transform of the Grassmann fields has been chosen such that the Greens functions are always free of factors of β which corresponds to: $c_{i,\alpha}(\tau) = \frac{1}{\sqrt{\beta}} \sum_{\omega} e^{-i\omega\tau} c_{i,\alpha}(i\omega)$ and $\bar{c}_{i,\alpha}(\tau) = \frac{1}{\sqrt{\beta}} \sum_{\omega} e^{+i\omega\tau} \bar{c}_{i,\alpha}(i\omega)$.

3 Analysis

3.1 Vertex Parametrization

3.1.1 System-specific Parametrization

Since the Hamiltonian of the theory (27) lacks a kinetic term, it follows immediately that the propagators of this theory are diagonal in real space. Hence, each vertex depends only on two lattice sites. Due to the fermionic nature of our degrees of freedom, each vertex must be antisymmetric under the exchange of the two external arguments which motivates the following real space parametrization (as introduced in Ref. [39]):

$$\Gamma(\hat{1}'\hat{2}';\hat{1}\hat{2}) = \Gamma^{\asymp}_{i_1 i_2}(1'2';12)\delta_{i_1 i_{1'}}\delta_{i_2 i_{2'}} - \Gamma^{)(}_{i_1 i_2}(1'2';12)\delta_{i_1 i_{2'}}\delta_{i_2 i_{1'}}. \tag{33}$$

The multiindices without a hat include only frequency and spin.

This parametrization can diagramatically be represented as:

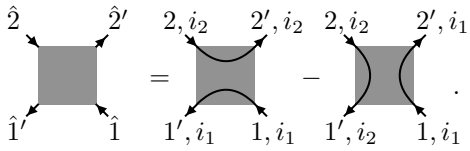

Note that this diagrammatic convention has the feature that the frequency and spin arguments are always at the same position and only the lattice site arguments differ.
It is convenient to formulate the equations entirely in terms of vertices with horizontal fermion lines, $\Gamma^{\asymp}_{i_1 i_2}(1'2';12)$, such that one does not need to distinguish between two different types in the equations and can thus drop the corresponding superscript. In order to achieve this, the translation from diagrammatics to mathematical expressions requires the extensive use of the identities:

Full vertex:

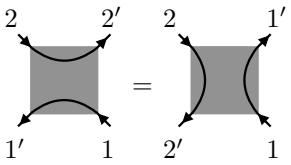

i.e. $\Gamma^{\asymp}_{i_1 i_2}(1'2';12) = \Gamma^{)(}_{i_1 i_2}(2'1';12)$

a-reducible:

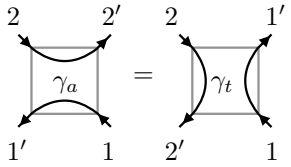

i.e. $\gamma^{\asymp}_{a,i_1 i_2}(1'2';12) = \gamma^{)(}_{t,i_1 i_2}(2'1';12)$

p-reducible:

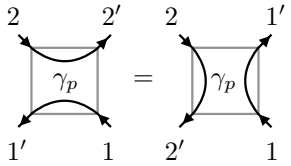

i.e. $\gamma^{\asymp}_{p,i_1 i_2}(1'2';12) = \gamma^{)(}_{p,i_1 i_2}(2'1';12)$

t-reducible:

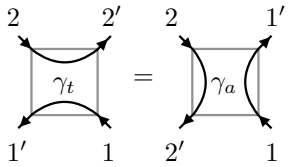

i.e. $\gamma^{\asymp}_{t,i_1 i_2}(1'2';12) = \gamma^{)(}_{a,i_1 i_2}(2'1';12)$

While the relation is straight forward for the full vertex and vertices reducible in the p-channel, it maps the t and the a-channel onto each other. This can be derived by considering the crossing relation,

$$\gamma_a(\hat{1}'\hat{2}',\hat{1}\hat{2}) = -\gamma_t(\hat{2}'\hat{1}',\hat{1}\hat{2}), \tag{34}$$

and rewriting both sides in their site-resolved form:

$$\text{l.h.s.} \;= \gamma^{\smile}_{\widetilde{a},i_1i_2}(1'2';12)\delta_{i_1i_{1'}}\delta_{i_2i_{2'}} - \gamma^{)(}_{a,i_1i_2}(1'2';12)\delta_{i_1i_{2'}}\delta_{i_2i_{1'}} \tag{35}$$

$$\text{r.h.s.} \;= -\gamma^{\smile}_{\widetilde{t},i_1i_2}(2'1';12)\delta_{i_1i_{2'}}\delta_{i_2i_{1'}} + \gamma^{)(}_{t,i_1i_2}(2'1';12)\delta_{i_1i_{1'}}\delta_{i_2i_{2'}}. \tag{36}$$

By comparing the proportionalities in real space (for the t-channel relation, one needs to exchange $(1' \leftrightarrow 2')$ in Eqs. (34-36) which leaves the site indices unaffected), one can identify the relations:

$$\gamma^{\smile}_{\widetilde{a},i_1i_2}(1'2';12) = \gamma^{)(}_{t,i_1i_2}(2'1';12) \tag{37}$$

$$\gamma^{\smile}_{\widetilde{t},i_1i_2}(1'2';12) = \gamma^{)(}_{a,i_1i_2}(2'1';12). \tag{38}$$

Since we want to keep the following derivations as general as possible such that they are valid, irrespective of whether the appearing vertices are reducible in a specific channel or not, we mark each general vertex that has been translated from a site-resolved vertex with vertical lines with a tilde[8], implying that the mapping between the a- and the t-channel needs to be performed for these objects, i.e.

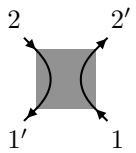

$$= \underbrace{\tilde{\Gamma}_{i_1i_2}(2'1',12)}_{\text{or } \tilde{\Gamma}_{i_2i_1}(1'2',21)} \overset{\rightrightarrows}{=} \begin{cases} \Gamma_{i_1i_2}(2'1',12) & \text{if } \Gamma = \text{full vertex} \\ \gamma_{t,i_1i_2}(2'1',12) & \text{if } \Gamma = \gamma_a \\ \gamma_{p,i_1i_2}(2'1',12) & \text{if } \Gamma = \gamma_p \\ \gamma_{a,i_1i_2}(2'1',12) & \text{if } \Gamma = \gamma_t. \end{cases}$$

where the expression in the underbrace is an equivalent translation that is related to the upper one by the generic identity of all two-particle vertices:

$$\Gamma_{i_1i_2}(1'2',12) = \Gamma_{i_2i_1}(2'1',21).$$

It is worth mentioning that in the one-loop-approximation, only full vertices appear in the equations for which this subtlety is irrelevant. In that case, all tildes in the flow equations can simply be dropped and there is no need to mark whether a vertex has been obtained from a diagram with vertical or horizontal fermion lines. In the multiloop corrections, however, one deals with nested bubble functions where only certain reducible parts of vertices are fed into higher order functions which requires a careful treatment following the procedure described above.

Further, by realizing that the only $SU(2)$ invariant spin interactions[9] that do not violate conservation properties are given by terms $\propto \delta_{\alpha\beta}\delta_{\gamma\delta}$ and $\propto \delta_{\alpha\delta}\delta_{\beta\gamma}$, one could in principle make a similiar decomposition as for the real space parametrization in Eq. (33) and formulate all equations in terms of two different vertex parts belonging to these two proportionality classes. However, it is convenient to adopt a more natural spin parametrization that makes a distinction between a *spin-interaction* part, Γ^s and a *density-interaction* part, Γ^d, of the vertex [39]:

$$\Gamma_{i_1i_2}(1'2';12) = \left\{\Gamma^s_{i_1i_2}(\omega_{1'}\omega_{2'};\omega_1\omega_2)\sigma^\mu_{\sigma_{1'}\sigma_1}\sigma^\mu_{\sigma_{2'}\sigma_2} + \Gamma^d_{i_1i_2}(\omega_{1'}\omega_{2'};\omega_1\omega_2)\delta_{\sigma_{1'}\sigma_1}\delta_{\sigma_{2'}\sigma_2}\right\}.$$

In Appendix B, we demonstrate the exact relation between these two approaches and explain how the names "spin-" and "density-" vertex are motivated.
Writing the bare vertex function in Eq. (29) in its fully parametrized form and comparing it to the Hamiltonian, one can identify the initial conditions for the vertex as:

$$\begin{cases} \lim\limits_{\Lambda\to\infty} \Gamma^s_{i_1i_2}(\omega_{1'}\omega_{2'};\omega_1\omega_2) = \Gamma^{0,s}_{i_1i_2}(\omega_{1'}\omega_{2'};\omega_1\omega_2) & = -\frac{1}{2}J_{i_1i_2}\delta_{\omega_1+\omega_2,\omega_{1'}+\omega_{2'}} \\ \lim\limits_{\Lambda\to\infty} \Gamma^d_{i_1i_2}(\omega_{1'}\omega_{2'};\omega_1\omega_2) & = 0. \end{cases} \tag{39}$$

[8] Note that in Ref. [42] which carries out a two-loop-analysis, *all* vertices in the explicit real space parametrization carry a tilde which has no further meaning. The tilde in our notation has nothing to do with theirs and indeed encodes important information about the mapping.

[9] It should be emphasized that the $SU(2)$ invariance is a direct consequence of the pseudo-fermion decomposition of the spin operators. However, this symmetry does not imply anything about the gauge structure of the effective low-energy theory (which refers to the type of present gauge fluctutations in the ground state) and thus does not conflict with a possible Z_2- or $U(1)$-spin liquid ground state. See Ref. [52] for a detailed clarification of this matter.

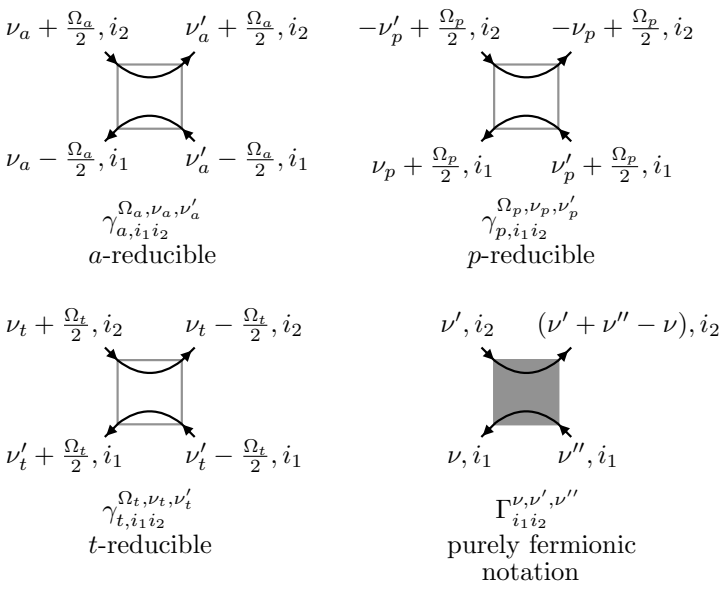

Fig. 6: Definition of the natural frequencies in the three channels and in a purely fermionic notation. Each vertex is characterized by one bosonic and two fermionic frequencies.

3.1.2 Channel-specific Frequency Arguments

Whenever specific frequency arguments are needed in the following, they refer to the natural frequencies in the individual channels as shown in Fig. 6 – the bosonic frequency Ω is always the transfer frequency of the respective channel. We chose this convention such that the asymptotics of the vertex functions are always centred around $\nu_r = \nu'_r = 0$ which will be elucidated more thoroughly in Sec. 3.3. Note that the full vertex can be expressed in any of the three mixed conventions, i.e.

$$\begin{aligned}
\Gamma^{\Omega_a,\nu_a,\nu'_a}_{i_1i_2} &= \Gamma_{i_1i_2}(\nu_a - \tfrac{\Omega_a}{2}, \nu'_a + \tfrac{\Omega_a}{2}; \nu'_a - \tfrac{\Omega_a}{2}, \nu_a + \tfrac{\Omega_a}{2}) \\
\Gamma^{\Omega_p,\nu_p,\nu'_p}_{i_1i_2} &= \Gamma_{i_1i_2}(\nu_p + \tfrac{\Omega_p}{2}, -\nu_p + \tfrac{\Omega_p}{2}; \nu'_p + \tfrac{\Omega_p}{2}, -\nu'_p + \tfrac{\Omega_p}{2}) \\
\Gamma^{\Omega_t,\nu_t,\nu'_t}_{i_1i_2} &= \Gamma_{i_1i_2}(\nu'_t + \tfrac{\Omega_t}{2}, \nu_t - \tfrac{\Omega_t}{2}; \nu'_t - \tfrac{\Omega_t}{2}, \nu_t + \tfrac{\Omega_t}{2}).
\end{aligned}$$

Labels "s/d" for the spin- and density parts have been suppressed here since the frequency parametrization is independent of the spin parametrization.
For reference, the conversion between the frequency arguments in the respective channels is given in Table 1.

In the following, we will often drop the channel labels for the frequencies (Ω, ν, ν') understanding that all quantities that are associated with one of the three channels are always labeled with their natural frequency arguments, i.e. frequency arguments on an a-bubble are always $(\Omega_a, \nu_a, \nu'_a)$ for instance. With this, the bubbles are readily parametrized as shown in Fig. 7.

	a-channel $(\Omega_a, \nu_a, \nu'_a)$	p-channel $(\Omega_p, \nu_p, \nu'_p)$	t-channel $(\Omega_t, \nu_t, \nu'_t)$
a-channel	$\Omega_a = \Omega_a$ $\nu_a = \nu_a$ $\nu'_a = \nu'_a$	$\Omega_p = \nu_a + \nu'_a$ $\nu_p = (-\nu'_a + \nu_a - \Omega_a)/2$ $\nu'_p = (\nu'_a - \nu_a - \Omega_a)/2$	$\Omega_t = \nu_a - \nu'_a$ $\nu_t = (\nu_a + \nu'_a + \Omega_a)/2$ $\nu'_t = (\nu_a + \nu'_a - \Omega_a)/2$
p-channel	$\Omega_a = -\nu_p - \nu'_p$ $\nu_a = (-\nu'_p + \nu_p + \Omega_p)/2$ $\nu'_a = (\nu'_p - \nu_p + \Omega_p)/2$	$\Omega_p = \Omega_p$ $\nu_p = \nu_p$ $\nu'_p = \nu'_p$	$\Omega_t = \nu_p - \nu'_p$ $\nu_t = (-\nu_p - \nu'_p + \Omega_p)/2$ $\nu'_t = (\nu_p + \nu'_p + \Omega_p)/2$
t-channel	$\Omega_a = \nu_t - \nu'_t$ $\nu_a = (\nu_t + \nu'_t + \Omega_t)/2$ $\nu_a = (\nu_t + \nu'_t - \Omega_t)/2$	$\Omega_p = \nu_t + \nu'_t$ $\nu_p = (\nu'_t - \nu_t + \Omega_t)/2$ $\nu'_p = (\nu'_t - \nu_t - \Omega_t)/2$	$\Omega_t = \Omega_t$ $\nu_t = \nu_t$ $\nu'_t = \nu'_t$
fermionic	$\Omega_a = \nu' - \nu$ $\nu_a = (\nu + \nu')/2$ $\nu'_a = \nu'' + (\nu' - \nu)/2$	$\Omega_p = \nu' + \nu''$ $\nu_p = \nu - (\nu' + \nu'')/2$ $\nu'_p = (\nu'' - \nu')/2$	$\Omega_t = \nu - \nu''$ $\nu_t = \nu' - (\nu - \nu'')/2$ $\nu'_t = (\nu + \nu'')/2$

Table 1: Frequency conversions between the three mixed conventions and the purely fermionic notation.

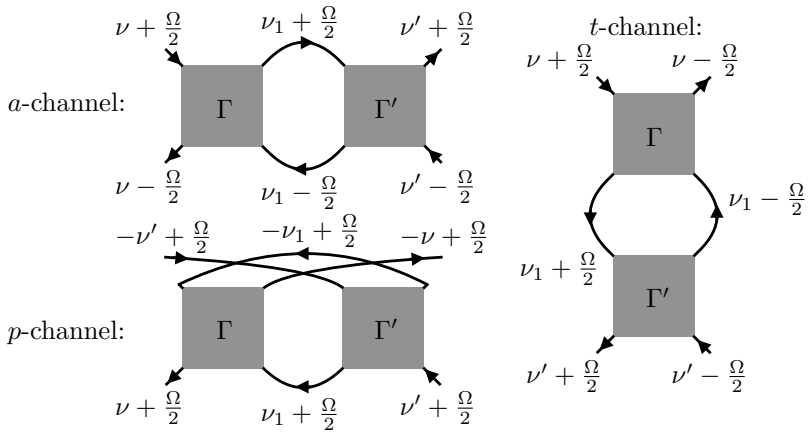

Fig. 7: Frequency label convention of bubble functions in all three channels with their natural frequencies.

3.2 System-specific Loop and Bubble Functions

The basic computational constituents of the flow equations fall into two classes: Bubble functions that connect two vertices in the vertex flow equations and loop functions that close fermionic loops in the self energy flow equation. However, their implementation depends strongly on the parametrization of the vertices which must be chosen appropriately for the underlying system. In our case, the spin parametrization leads to nontrivial combinatorial factors in the flow equations and the mapping identities in Eqs. (37,38) lead to further subtleties that become important for the mutliloop corrections as explained in Sec. 3.1.1. Since the flow equations with the combinatorial factors have been stated in the literature only without general consideration for the channel mapping (e.g. Ref. [36] for the one-loop case, Ref. [42] for the two-loop case), we consider it sensible to sketch the derivation of general bubble and loop functions that take care of this in the most general fashion and from which one can build up the flow equations at arbitrary loop order, reproducing also those in the mentioned references.

3.2.1 Loop Functions

We define a general loop function $L(\Gamma, G)$ as a general vertex Γ of which the upper frequency legs are connected by a fermionic propagator G which can be of any type (e.g. full propagator, single scale propagator, etc.). The easiest way to find this function in its fully parametrized form is to start by inserting the real space parametrization of the vertex, Eq. (33), on the diagrammatic level:

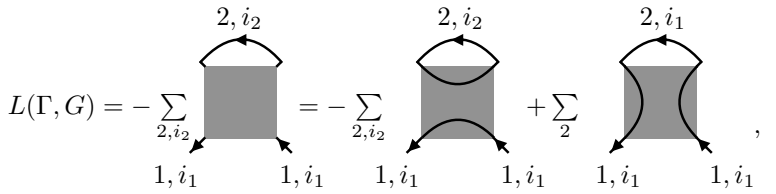

which is the diagrammatic translation of:

$$L(\Gamma, G)(\omega_1) = -\sum_{\hat{2}} \Gamma(\hat{1}\hat{2};\hat{1}\hat{2}) G(\omega_2) = -\sum_{2} G(\omega_2) \left\{ \sum_{i_2} \Gamma_{i_1 i_2}(12;12) - \tilde{\Gamma}_{i_1 i_1}(21;12) \right\}.$$

Note that the last term does not contain a summation over lattice sites due to the fact that the propagator is local which implies that the site index cannot change along fermion lines. Moreover, energy and spin conservation has been employed. The loop function carries neither a site nor a spin index since it holds for an arbitrary site i_1 and spin σ_1.
Using the spin parametrization explicitly, one finds for the individual terms on the right hand side:

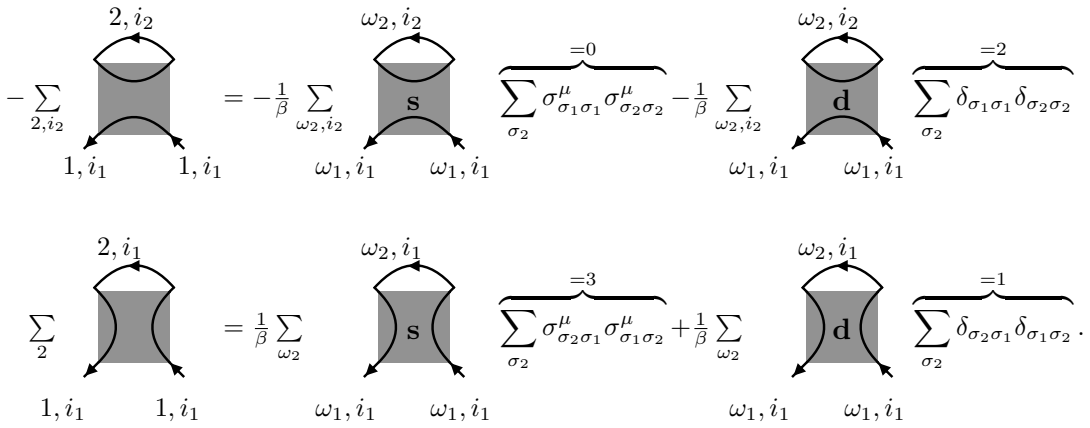

This yields nontrivial combinatorial factors for the spin and density parts of the vertex that enter the loop function. Collecting all parts, one obtains for the loop function:

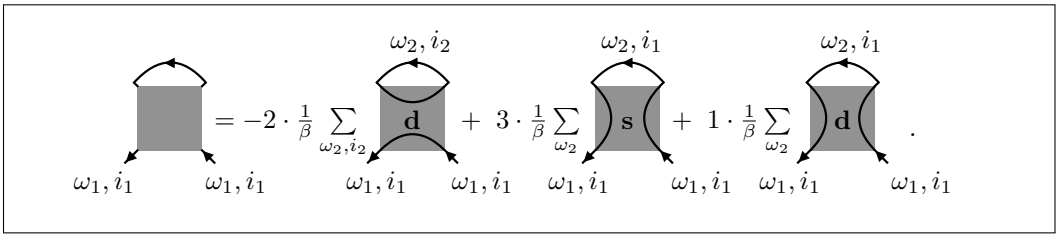

The corresponding mathematical expression reads:

$$L(\Gamma, G)(\omega_1) =$$
$$-\frac{1}{\beta} \sum_{\omega_2} G(\omega_2) \left\{ 2 \cdot \sum_{i_2} \Gamma^d_{i_1 i_2}(\omega_1\omega_2;\omega_1\omega_2) - 3 \cdot \tilde{\Gamma}^s_{i_1 i_1}(\omega_2\omega_1;\omega_1\omega_2) - \tilde{\Gamma}^d_{i_1 i_1}(\omega_2\omega_1;\omega_1\omega_2) \right\}, \qquad (40)$$

from which one can directly infer the standard contribution to the self energy flow equation by replacing $G \to S$ on the right hand side of Eq. (40). All spin indices have been summed out and are now encoded in the combinatorial factors.

Having derived the general loop function with the combinatorial factors, lets us return to the condition in Eq. (28) and to the initial condition for the self energy. In principle, the latter is given by the Fock-contribution which is frequency independent and does not change during the flow. This can be seen by integrating the differentiated self energy in a small interval at the beginning of the flow:

$$\Sigma_{\Lambda\to\infty}(\omega_1) \overset{(1)}{=} \lim_{\Lambda_0\to\infty} \int_{\infty}^{\Lambda_0} d\Lambda \dot{\Sigma}_\Lambda(\omega_1) = \tag{41}$$

$$\overset{(2)}{=} \lim_{\Lambda_0\to\infty} \int_{\infty}^{\Lambda_0} d\Lambda (-\frac{1}{\beta}) \sum_{\omega_2} S_\Lambda(\omega_2)(-3) \cdot \Gamma^0_{ii}(\omega_2\omega_1;\omega_1\omega_2) = \tag{42}$$

$$\overset{(3)}{=} -\frac{3}{2} J_{ii} \Big(\frac{1}{\beta} \sum_{\omega_2} G_{\Lambda=0}(\omega_2) - \lim_{\Lambda_0\to\infty} \int_{\Lambda_0}^{0} d\Lambda \underbrace{\frac{1}{\beta} \sum_{\omega_2} S_\Lambda(\omega_2)}_{=0} \Big) = \tag{43}$$

$$\overset{(4)}{=} -\frac{3}{2} J_{ii} \underbrace{\frac{1}{\beta} \sum_{\omega_2} G(\omega_2) e^{i\omega_2 0^+}}_{-\langle T_\tau \hat{c}_\alpha(\tau=0^-)\hat{c}^\dagger_\alpha(0)\rangle} \overset{(5)}{=} -\frac{3}{2} J_{ii} n_{\mathrm{F},\alpha}(\Sigma_{\Lambda\to\infty} - \tilde{\mu}). \tag{44}$$

In step (2), we used the limit

$$\lim_{\Lambda\to\infty} \Gamma_\Lambda = \Gamma^0$$

from Eq. (39) such that only the "spin-term" in Eq. (40) contributes to the differentiated self energy. In step (3), we used that the Matsubara sum vanishes for any finite $\Lambda \in [0, \Lambda_0]$ since $S_\Lambda(\omega) = -G_\Lambda(\omega) \cdot \left(\frac{d}{d\Lambda} G^{-1}_{0,\Lambda}(\omega) \right) \cdot G_\Lambda(\omega)$ is antisymmetric in ω with present particle-hole symmetry as will be shown explicitly in Sec. 3.4.1. Finally, in step (4), we restored the infinitesimal regularizer that is an artifact of the discreteness of the imaginary-time in the path integral formalism.
The condition from Eq. (28) and spin $SU(2)$ symmetry require that $n_{\mathrm{F},\uparrow} = n_{\mathrm{F},\downarrow} = \frac{1}{2}$ which implies that

$$\tilde{\mu} = \Sigma_{\Lambda\to\infty} = -\frac{3}{4} J_{ii} \to \mu = 0.$$

This result is not surprising since $\mu = 0$ corresponds to half filling in a particle-hole symmetric system. Consequently, half of the states are projected out on average[10] such that the condition in Eq. (28) is satisfied. Since in the full propagator, $G^{-1}(\omega) = i\omega + \tilde{\mu} - \Sigma(\omega)$, the self energy and the chemical potential enter with different signs, the constant Fock-contribution in the self energy (constant during the flow and independent of ω) and the effective chemical potential $\tilde{\mu}$ always cancel to zero and one can therefore set both quantities to zero at the beginning of the flow, i.e. the initial condition for the self energy (corresponding to $\tilde{\mu} = \mu = 0$) reads:

$$\Sigma_{\Lambda\to\infty}(\omega) = 0, \tag{45}$$

which matches the initial condition stated in Ref. [5, 39]. In fact, since $J_{ii} = 0$ in our specific case of the KHM, this statement is trivial and $\tilde{\mu} = \Sigma_{\Lambda\to\infty} = 0$ is always true.

3.2.2 Bubble Functions

An similar strategy yields the combinatorial factors for the bubble functions in the three different channels which, however, differ quite significantly in their complexity. We explain only the derivation for p-bubbles in the main text since it requires translating vertical fermion lines to horizontal

[10] This reasoning is used in Ref. [36] to obtain $\mu = 0$ immediately.

lines and marking certain vertices with a tilde which has not explicitly been stated in the literature for the general case. The a-channel is less interesting because no translation is necessary and the t-channel is a bit more intricate and does not serve as pedagogical example. Hence, both these channels are shown in Appendix C.

We define a general bubble in the p-channel as:

$$B_p(\Gamma,\Gamma')_{\hat{1}'\hat{2}',\hat{1}\hat{2}} = \tfrac{1}{2}\sum_{\hat{3}\hat{4}} \Gamma(\hat{1}'\hat{2}',\hat{3}\hat{4})\Gamma'(\hat{3}\hat{4},\hat{1}\hat{2})G(\omega_3)G(\omega_4).$$

Note that we include a factor of $\frac{1}{2}$ in the definition of a bubble in the p-channel due to the indistinguishability of the two propagators.
Again, the antisymmetry of the full vertex under the exchange of to external variables, Eq. (33), is used to parametrize the bubble function in real space on the diagrammatic level:

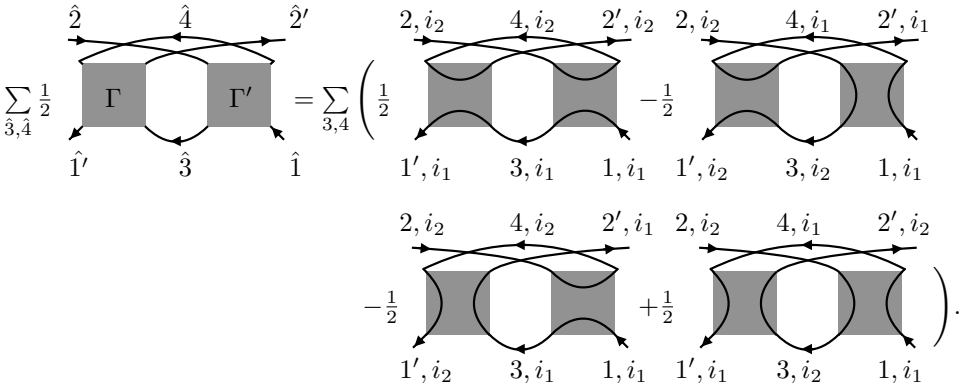

By comparing the contributions, one finds that the first and the last diagram have the same proportionality in real space, $\delta_{i_1 i_{1'}}\delta_{i_2 i_{2'}}$. The same is true for the second and the third diagram which are both proportional to $\delta_{i_2 i_{1'}}\delta_{i_1 i_{2'}}$. Identifying the respective terms with the appropriate object in the decomposed bubble function,

$$B_p(\Gamma,\Gamma')_{\hat{1}'\hat{2}',\hat{1}\hat{2}} = B^{\asymp,\Gamma,\Gamma'}_{p,i_1 i_2}(1'2',12)\delta_{i_1 i_{1'}}\delta_{i_2 i_{2'}} - B^{)(,\Gamma,\Gamma'}_{p,i_1 i_2}(1'2',12)\delta_{i_1 i_{2'}}\delta_{i_2 i_{1'}},$$

one can write the left and right side of the flow equations in this decomposed form and thus reduce the flow equations to only one proportionality class. Using the spin parametrization from above, one obtains for $B^{\asymp,\Gamma,\Gamma'}_{p,i_1 i_2}(1'2',12)$ (in the following we will always drop the horizontal lines from all bubble functions understanding that we always consider only this part):

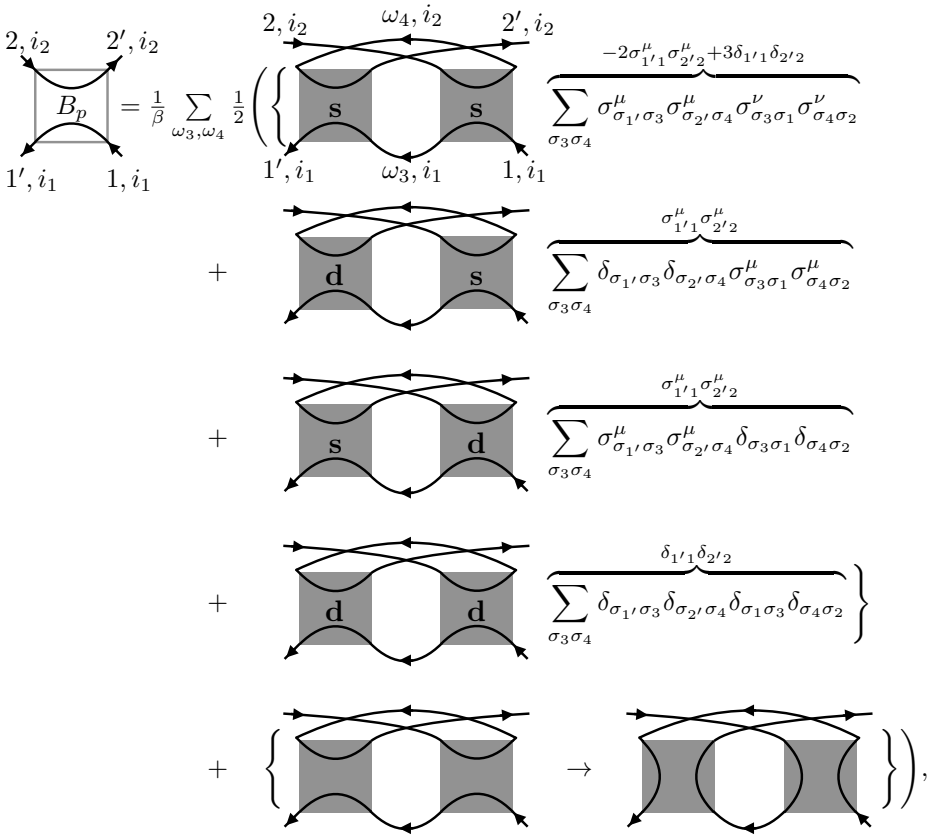

where all frequency and site indices have been suppressed in all but the first diagram on the right hand side as they are exactly the same. The abbreviation in the last line is intended to imply that the first four diagrams are repeated with a slightly different fermionic line structure but with the same index structure and hence with the same combinatorial factors (which is an effect of $SU(2)$ spin symmetry). Note that in the one-loop-scheme, the first four contributions are equivalent to the second four which can diagramatically be seen by using the identity for the full vertex:

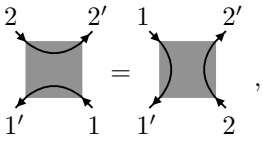

and interchanging the dummy indices $3 \leftrightarrow 4$.
After the evaluation of the spin sums, one finds the same proportionalities as in the initial spin parametrization of the full vertex. Consequently, one can rewrite the right hand side in terms of a spin vertex and a density vertex. Schematically, this leads to the rule for p-channel-bubbles in the spin-density parametrization that is shown in Fig. 8.

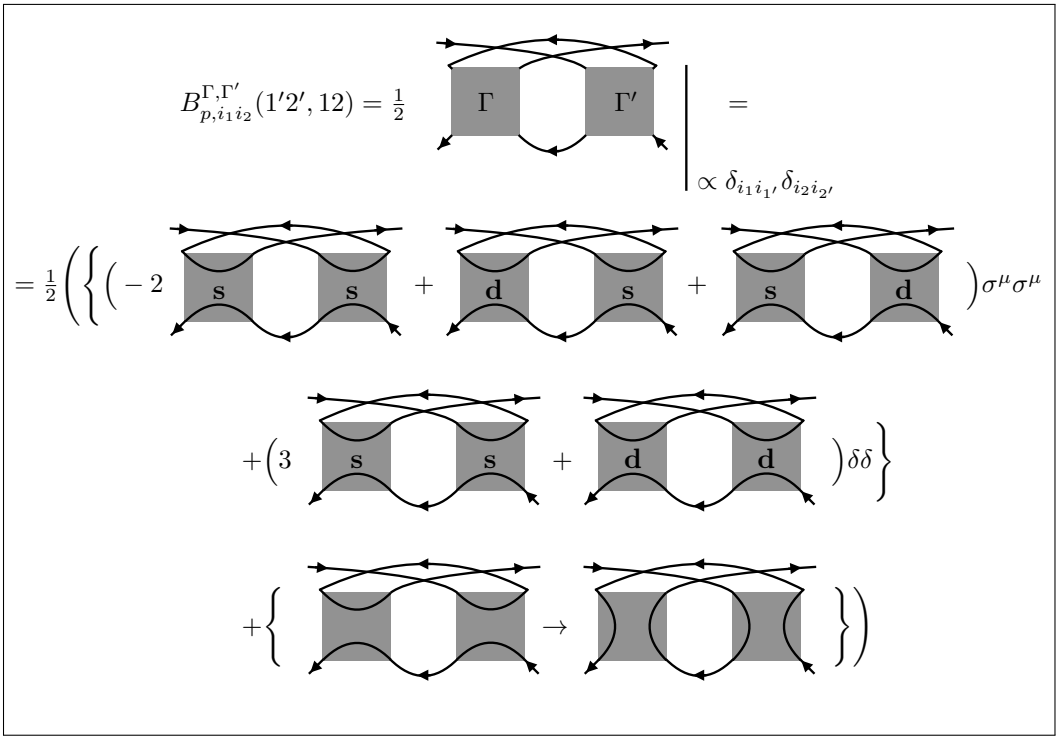

Fig. 8: Effective rule for bubbles in the p-channel.

The expression in the first bracket in Fig. 8 is the spin part of the bubble function and the second bracket encloses the density part. The mathematical translation can be made by restoring the frequency and site arguments from above:

$$
\begin{aligned}
B^{\Gamma,\Gamma'}_{p,i_1i_2}(1'2',12) = \frac{1}{2}\frac{1}{\beta}\sum_{\omega_3,\omega_4} G(\omega_3)G(\omega_4)\times \\
\times\Bigg(\Bigg\{\Big(&-2\cdot\Gamma^s_{i_1i_2}(\omega_{1'}\omega_{2'};\omega_3\omega_4)\Gamma'^s_{i_1i_2}(\omega_3\omega_4;\omega_1\omega_2) \\
&+\Gamma^d_{i_1i_2}(\omega_{1'}\omega_{2'};\omega_3\omega_4)\Gamma'^s_{i_1i_2}(\omega_3\omega_4;\omega_1\omega_2) \\
&+\Gamma^s_{i_1i_2}(\omega_{1'}\omega_{2'};\omega_3\omega_4)\Gamma'^d_{i_1i_2}(\omega_3\omega_4;\omega_1\omega_2)\Big)\sigma^\mu_{\sigma_{1'}\sigma_1}\sigma^\mu_{\sigma_{2'}\sigma_2} \\
+\Big(&3\cdot\Gamma^s_{i_1i_2}(\omega_{1'}\omega_{2'};\omega_3\omega_4)\Gamma'^s_{i_1i_2}(\omega_3\omega_4;\omega_1\omega_2) \\
&+\Gamma^d_{i_1i_2}(\omega_{1'}\omega_{2'};\omega_3\omega_4)\Gamma'^d_{i_1i_2}(\omega_3\omega_4;\omega_1\omega_2\Big)\delta_{\sigma_{1'}\sigma_1}\delta_{\sigma_{2'}\sigma_2}\Bigg\} \\
+\Big\{&(\Gamma\to\tilde{\Gamma}) \text{ and } (\Gamma'\to\tilde{\Gamma}')\Big\}\Bigg).
\end{aligned}
\tag{46}
$$

We recall that energy conservation is implicitly contained in the vertices according to Eq. (39). In order to arrive at this compact result, we exchanged the dunmmy variables $\omega_3 \leftrightarrow \omega_4$ in the last bracket after translating the vertices with vertical lines to ones with horizontal lines and marking them with a tilde. This exchange is possible due to the indistinguishability of the propagators. Also on this level it is obvious that, when dropping the tildes (corresponding to the one-loop scheme), every term has an exact equivalent such that combining them reduces the expression to half its number of terms which can be used to cancel the overall factor $\frac{1}{2}$. If, however, the vertex is not always a full vertex, mapping between the a- and t-channel may play a role and it is crucial to take the tildes into account. Though they seem to appear in a very lucid way here, the t-channel proves that this is not generally the case and it is not possible to account for the correct mappings

a posteriori if one only knows the one-loop equations where this feature is not considered.
The derived combinatorial factors are valid for any bubble function in the p-channel, i.e. irrespective of details of the propagators and vertices.

3.3 Frequency Asymptotics

Our algorithmic implementation is based on the diagrammatic classification of 2PR diagrams according to their high frequency behavior[11]. This section focuses on diagrammatic arguments where we follow the reasoning from Ref. [54] very closely. For the actual implementation, we propose a slightly altered scheme which will further be explained in Sec. 3.5.2.
The philosophy behind the high frequency classification can be stated very compactly: Since the bare interaction is frequency independent, it cannot "forward" the information about the external fermionic frequency ν (ν') into an arbitrary higher order diagram if both legs carrying the frequency index ν (ν') are connected to the same bare vertex[12] – in that case, the entire diagram is independent of the respective fermionic frequency. From Fig. 7, it is clear that both legs with the same fermionic frequency label are always attached to the same vertex, i.e. Γ can only know about ν and Γ' is only given information about ν'. This yields criteria for the asymptotic classification of 2PR-diagrams into four distinct classes:

1. $K^{\Omega}_{1,ij}$: Both legs with the same fermionic frequency argument are connected to the same bare vertex, respectively. Hence, none of the fermionic frequency arguments enters the diagram and it depends only on the bosonic transfer frequency due to energy conservation.

2. $K^{\Omega,\nu}_{2,ij}$: The legs depending on ν are connected to different bare vertices in Γ and the legs depending on ν' are connected to the same bare vertex in Γ'. Hence, only ν enters the diagram.

3. $K^{\Omega,\nu'}_{2',ij}$: The legs depending on ν are connected to the same bare vertex in Γ and the legs depending on ν' are connected to different bare vertices in Γ'. Hence, only ν' enters the diagram.

4. $K^{\Omega,\nu,\nu'}_{3,ij}$: All external legs are connected to different bare vertices. Hence, ν and ν' both enter the diagram.

Moreover, we introduce the generalized notation "$K^{\vec{\omega}}_{n,r,\vec{R}}$" which will come in handy at a later point. This is to be understood as a vertex of the asympotic class $n \in \{1, 2, 2', 3\}$ in the r-channel. The site indices are confined to the vector $\vec{R}$ and the frequency vector $\vec{\omega}$ contains all *necessary* frequency arguments for class n, i.e. $\vec{\omega} = (\Omega)$ if $n = 1$, $\vec{\omega} = (\Omega, \nu)$ if $n = 2$, etc.

From diagrammatics, one can deduce that two external fermion legs of an r-reducible diagram that carry the same fermionic frequency label can only touch different bare vertices if they are connected to a diagrammatic building block that is reducible in a channel $r' \neq r$. This is shown for a simple case in Fig. 9.

From Table 1, it follows that the bosonic transfer frequency $\Omega_{r'\neq r}$ of this channel then depends linearly on the respective external fermionic frequency, ν_r or ν'_r, of the r-reducible vertex. Since

$$\left| G(\nu_2 \pm \tfrac{\Omega_{r'\neq r}}{2}) G(\mp\nu_2 + \tfrac{\Omega_{r'\neq r}}{2}) \right| \xrightarrow{\Omega_{r'\neq r}\to\infty} 0,$$

we can argue that these subdiagrams vanish if the external *fermionic* frequency of the r-channel diagram is taken to infinity. Hence, it is possible to specifically eliminate all diagrammatic contributions from a general vertex that depend on ν_r, ν'_r, respectively, by taking the appropriate fermionic

[11] The classification refers only to the reducible diagrams since the class of totally 2PI diagrams in the parquet approximation contains only the bare interaction which is frequency independent.
[12] The external fermionic legs themselves are amputated and only fix the external argument.

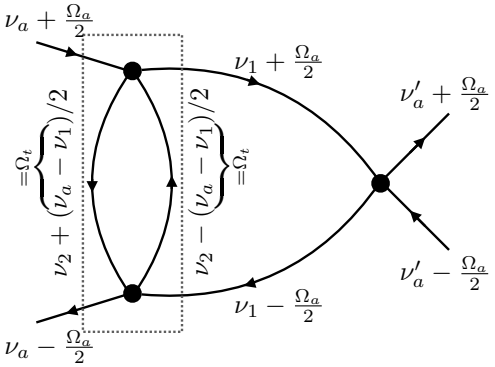

Fig. 9: "Fish-eye diagram" as simple example of how a fermionic frequency can enter a higher order vertex. The boxed subdiagram belongs to the t-channel whereas the overall diagramm belongs to the a-channel. Note that the bosonic tranfer frequency in the subdiagram depends linearly on ν_a: $\Omega_t = \nu_a - \nu_1$. Hence, this diagram vanishes for $\nu_a \to \infty$. Since it is independent of ν'_a, it belongs to the class $K_{2,a}$.

high frequency limits. More precisely:

$$\lim_{\nu\to\infty}\lim_{\nu'\to\infty} B^{\vec{\omega}}_{r,\vec{R}} = K^{\ \Omega}_{1,r,\vec{R}} \tag{47}$$

$$\lim_{\nu'\to\infty} B^{\vec{\omega}}_{r,\vec{R}} = K^{\ \Omega,\nu}_{2,r,\vec{R}} + K^{\ \Omega}_{1,r,\vec{R}} \tag{48}$$

$$\lim_{\nu\to\infty} B^{\vec{\omega}}_{r,\vec{R}} = K^{\ \Omega,\nu'}_{2',r,\vec{R}} + K^{\ \Omega}_{1,r,\vec{R}} \tag{49}$$

$$B^{\vec{\omega}}_{r,\vec{R}} = K^{\ \Omega}_{1,r,\vec{R}} + K^{\ \Omega,\nu}_{2,r,\vec{R}} + K^{\ \Omega,\nu'}_{2',r,\vec{R}} + K^{\ \Omega,\nu,\nu'}_{3,r,\vec{R}}. \tag{50}$$

Conceptually, one could solve this set of equations for all four asymptotic classes. Having individual access to the asymptotic functions, where only K_3 has the full frequency dependence, comes with great algorithmic advantages:
The diagrammatic class $K_3^{\Omega,\nu,\nu'}$ decays when any of the three frequencies is increased. Consequently, its contributions will only play a role in a small frequency range around the origin in three dimensional frequency space[13]. The decay properties for $K_2^{\Omega,\nu}$ and $K_{2'}^{\ \Omega,\nu'}$ are similar with the difference that they do not decay with ν' and ν, respectively, and thus show asymptotic behaviour only in certain directions in frequency space. The K_1^{Ω}-class is completely independent of the fermionic arguments and decays only with Ω. Consequently, though a general reducible vertex is in principle the sum of all diagrammatic classes according to Eq. (50), only certain classes contribute farther away from the origin where K_3 has always decayed. Since the K_2-, $K_{2'}$- and especially the K_1-class can be computed with strongly reduced numerical costs, one can store very exact vertex values for almost arbitrary high frequencies. In practice, we store values for K_3 in a small box around the origin with fixed side length, K_2- and $K_{2'}$ in a two-dimensional array with greater side length and K_1 in a one-dimensional array with the greatest length. Depending on the frequency combination, we compute the vertex values as the sum of all *relevant* asymptotic classes. This idea is schematically shown in Fig. 10.

3.4 Symmetries

3.4.1 Symmetries of the 2- and 4-Point Vertex

At the one-particle level, particle-hole-symmetry has the effect that all two-particle correlators in frequency space are purely imaginary which is a result of their local nature as can be derived by

[13]The fact that the asymptotics are centered around the origin in all three channels is a direct consequence of our frequency label convention - Ref. [54] uses a different convention where the asymptotics are centered around $(0, \pm\nu/2, \pm\nu'/2)$.

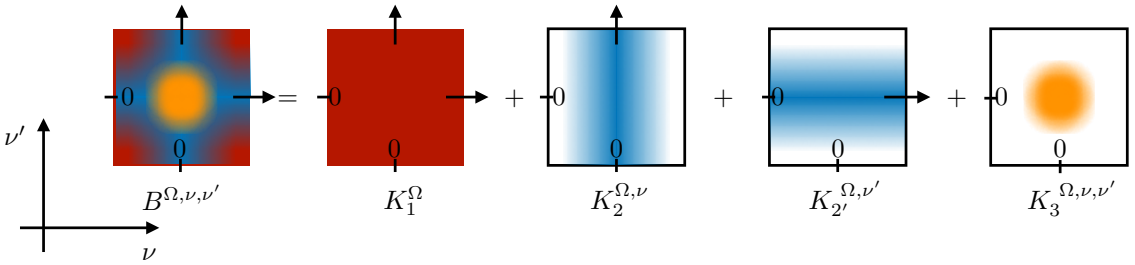

Fig. 10: The asymptotic classes decay in different frequency directions, here sketched for an arbitrary channel and constant bosonic frequency. If a given frequency combination lies in the white area for one of the classes, this class does not contribute. The arrows indicate that the values beyond the square are equal to the values on the edge in this direction. Note: The different colors have been chosen for demonstration and do not encode quantitative information. Different levels of opacity mark the relevant areas and directions of decay of the individual classes though the functional behaviour may be nontrivial in theses areas. For numerical data, see Sec. 3.5.3.

rewriting Eq. (30) on the operator level in imaginary time:

$$\begin{aligned} G(\tau,0) &= -\left\langle \mathcal{T}_\tau \hat{c}_{i,\sigma}(\tau)\hat{c}^\dagger_{i,\sigma}(0)\right\rangle = -\Theta(\tau)\left\langle \hat{c}_{i,\sigma}(\tau)\hat{c}^\dagger_{i,\sigma}(0)\right\rangle + \Theta(-\tau)\left\langle \hat{c}^\dagger_{i,\sigma}(0)\hat{c}_{i,\sigma}(\tau)\right\rangle \\ &= \frac{1}{\beta}\sum_\omega e^{-i\omega\tau}\underbrace{(-1)\left\langle c_{i,\sigma}(i\omega)\bar{c}_{i,\sigma}(i\omega)\right\rangle}_{G(i\omega)}. \end{aligned} \tag{51}$$

For the complex conjugate, one finds in the local case (anti-time-ordering is denoted by $\tilde{\mathcal{T}}_\tau$):

$$\begin{aligned} G^*(\tau,0) &= -\left\langle \mathcal{T}_\tau \hat{c}_{i,\sigma}(\tau)\hat{c}^\dagger_{i,\sigma}(0)\right\rangle^* = -\left\langle \tilde{\mathcal{T}}_\tau \hat{c}_{i,\sigma}(0)\hat{c}^\dagger_{i,\sigma}(\tau)\right\rangle \\ &= -\left\langle \mathcal{T}_\tau \hat{c}_{i,\sigma}(\tau)\hat{c}^\dagger_{i,\sigma}(0)\right\rangle = G(\tau,0). \end{aligned} \tag{52}$$

Using particle-hole symmetry, one finds the identity:

$$\begin{aligned} G(\tau,0) &\overset{\text{p.h.-sym}}{=} -\left\langle \mathcal{T}_\tau \hat{c}^\dagger_{i,\sigma}(\tau)\hat{c}_{i,\sigma}(0)\right\rangle \\ &= -\Theta(\tau)\left\langle \hat{c}^\dagger_{i,\sigma}(\tau)\hat{c}_{i,\sigma}(0)\right\rangle + \Theta(-\tau)\left\langle \hat{c}_{i,\sigma}(0)\hat{c}^\dagger_{i,\sigma}(\tau)\right\rangle = -G(-\tau,0). \end{aligned} \tag{53}$$

Consequently, taking Eqs. (51 - 53) together, one can conclude that $G(i\omega)$ is purely imaginary and antisymmetric in ω which results in the relation:

$$G^*(i\omega) = G(-i\omega) = -G(i\omega).$$

Considering the Schwinger-Dyson equation,

$$G(i\omega) = G_0(i\omega) + G_0(i\omega)\Sigma(i\omega)G(i\omega),$$

it is clear that the above statements about the Greens function (antisymmetry and vanishing real part) must also hold true for the self energy itself.

On the two-particle level, the imaginary time correlation function (for the real space proportionality class $\delta_{i_1 i_{1'}}\delta_{i_2 i_{2'}}$) is defined as:

$$G^{(4)}_{i_1 i_2,\sigma_{1'}\sigma_{2'},\sigma_1\sigma_2}(\tau_{1'}\tau_{2'};\tau_1\tau_2) = -\left\langle \mathcal{T}_\tau[\hat{c}_{i_1,\sigma_1}(\tau_1)\hat{c}_{i_2,\sigma_2}(\tau_2)\hat{c}^\dagger_{i_2,\sigma_{2'}}(\tau_{2'})\hat{c}^\dagger_{i_1,\sigma_{1'}}(\tau_{1'})]\right\rangle. \tag{54}$$

In the $SU(2)$ invariant case, the two-particle propagator only depends on two spins with either $(\sigma_1 = \sigma_{1'} \wedge \sigma_2 = \sigma_{2'})$ or $(\sigma_1 = \sigma_{2'} \wedge \sigma_2 = \sigma_{1'})$. Even though a time reversal transformation flips spin, it is safe to suppress the spin indices in the following because $G_{\uparrow\downarrow} = G_{\downarrow\uparrow}$ and $G_{\uparrow\uparrow} = G_{\downarrow\downarrow}$. Making

analogous manipulations as in the one-particle case, one finds the following relations between the symmetry transformations and complex conjugation:

$$(G^{(4)}_{i_1 i_2}(\tau_{1'}\tau_{2'};\tau_1\tau_2))^* = G^{(4),\text{time-rev.}}_{i_1 i_2}(\tau_{1'}\tau_{2'};\tau_1\tau_2) \tag{55}$$

$$G^{(4),\text{hole}}_{i_1 i_2}(\tau_{1'}\tau_{2'};\tau_1\tau_2) = G^{(4)}_{i_1 i_2}(\tau_1\tau_2;\tau_{1'}\tau_{2'}). \tag{56}$$

This implies in Matsubara frequency space:

$$(G^{(4)}_{i_1 i_2}(\omega_{1'}\omega_{2'};\omega_1\omega_2))^* = G^{(4),\text{time-rev.}}_{i_1 i_2}(-\omega_{1'},-\omega_{2'};-\omega_1,-\omega_2) = \tag{57}$$

$$= G^{(4)}_{i_1 i_2}(-\omega_1,-\omega_2;-\omega_{1'},-\omega_{2'}) \tag{58}$$

$$G^{(4),\text{hole}}_{i_1 i_2}(\omega_{1'}\omega_{2'};\omega_1\omega_2) = (G^{(4)}_{i_1 i_2}(\omega_{1'}\omega_{2'};\omega_1\omega_2))^*. \tag{59}$$

Remarkably, this implies that all two-particle-quantities are purely real in the case of unbroken particle hole symmetry[14]. By amputating the external legs and eliminating all disconnected diagrams from $G^{(4)}$, one obtains the full interaction vertex, $\Gamma(\hat{1}'\hat{2}', \hat{1}\hat{2})$.

In order to derive symmetry relations for the different diagrammatic classes in all three channels, we successively apply the three symmetry operations:

- (a): Simultaneous exchange of both incoming and both outgoing legs
- (b): Complex conjugation (= particle-hole-transformation for p-h-symmetry)
- (c): Time reversal transformation

Operations (a) and (b) can always be used to derive identities for all two-particle quantities such that only a reduced frequency range needs to be computed explicitly. In the special case of particle-hole and time reversal symmetry, all three operations leave the two-particle quantities invariant. In terms of diagrammatics, complex conjugation has the effect of switching the direction of the arrows on all fermionic lines and additionally switching the sign of each frequency. A time reversal transformation also switches the arrows but does not change the signs. Exchanging both incoming and outgoing legs amounts to a π-rotation of the diagram.

Though this procedure is independent of the underlying system, we explicitly use the $SU(2)$ spin symmetry of our vertices, i.e. $\Gamma_{\alpha\beta\gamma\delta} = \Gamma_{\delta\gamma\beta\alpha}$ and $\Gamma_{\alpha\beta\gamma\delta} = \Gamma_{\gamma\delta\alpha\beta}$, such that the three symmetry transformations have no effect in spin space. This allows us to work on the level of the vertices in their final parametrization, $\Gamma^{s/d}_{ij}(\omega_{1'}\omega_{2'};\omega_1\omega_2)$, i.e. without carrying around spin indices.

In the $K_{1,r}$ class of diagrams, one obtains the relations:

$$K^{\Omega}_{1,a,i_1 i_2} = \begin{cases} \overset{(a)}{=} K^{-\Omega}_{1,a,i_2 i_1} \\ \overset{(b)}{=} (K^{-\Omega}_{1,a,i_1 i_2})^* \\ \overset{(c)}{=} K^{\Omega}_{1,a,i_1 i_2} \end{cases} \qquad K^{\Omega}_{1,p,i_1 i_2} = \begin{cases} \overset{(a)}{=} K^{\Omega}_{1,p,i_2 i_1} \\ \overset{(b)}{=} (K^{-\Omega}_{1,p,i_2 i_1})^* \\ \overset{(c)}{=} K^{\Omega}_{1,p,i_2 i_1} \end{cases}$$

$$K^{\Omega}_{1,t,i_1 i_2} = \begin{cases} \overset{(a)}{=} K^{-\Omega}_{1,t,i_2 i_1} \\ \overset{(b)}{=} (K^{\Omega}_{1,t,i_1 i_2})^* \\ \overset{(c)}{=} K^{-\Omega}_{1,t,i_1 i_2} \end{cases}$$

For the classes K_2 and $K_{2'}$, the symmetry operations yield[15]:

[14] A general analysis of the effects that physical symmetries have on the properties of local n-particle Greens functions is presented in Ref. [40] for instance.

[15] Note that K_2 and $K_{2'}$ are interchanged by some operations. In that case we combine the operations such that we find two equivalent expressions for every object of the class K_2

$$K_{2,a,i_1i_2}^{\Omega,\nu} = \begin{cases} \overset{(a)}{=} K_{2',a,i_2i_1}^{-\Omega,\nu} \\ \overset{(b)}{=} (K_{2',a,i_1i_2}^{-\Omega,(-\nu)})^* \\ \overset{(c)}{=} K_{2',a,i_1i_2}^{\Omega,\nu} \\ \overset{(a+b)}{=} (K_{2,a,i_2i_1}^{\Omega,(-\nu)})^* \\ \overset{(a+c)}{=} K_{2,a,i_2i_1}^{-\Omega,\nu} \end{cases} \qquad K_{2,p,i_1i_2}^{\Omega,\nu} = \begin{cases} \overset{(a)}{=} K_{2,p,i_2i_1}^{\Omega,(-\nu)} \\ \overset{(b)}{=} (K_{2',p,i_2i_1}^{-\Omega,\nu})^* \\ \overset{(c)}{=} K_{2',p,i_2i_1}^{\Omega,(-\nu)} \\ \overset{(b+c)}{=} (K_{2,p,i_1i_2}^{-\Omega,(-\nu)})^* \end{cases}$$

$$K_{2,t,i_1i_2}^{\Omega,\nu} = \begin{cases} \overset{(a)}{=} K_{2',t,i_2i_1}^{-\Omega,\nu} \\ \overset{(b)}{=} (K_{2,t,i_1i_2}^{\Omega,(-\nu)})^* \\ \overset{(c)}{=} K_{2,t,i_1i_2}^{-\Omega,\nu} \end{cases}$$

and for the K_3-class:

$$K_{3,a,i_1i_2}^{\Omega,\nu,\nu'} = \begin{cases} \overset{(a)}{=} K_{3,a,i_2i_1}^{-\Omega,\nu',\nu} \\ \overset{(b)}{=} (K_{3,a,i_1i_2}^{-\Omega,(-\nu'),(-\nu)})^* \\ \overset{(c)}{=} K_{3,a,i_1i_2}^{\Omega,\nu',\nu} \end{cases} \qquad K_{3,p,i_1i_2}^{\Omega,\nu,\nu'} = \begin{cases} \overset{(a)}{=} K_{3,p,i_2i_1}^{\Omega,(-\nu),(-\nu')} \\ \overset{(b)}{=} (K_{3,p,i_1i_2}^{-\Omega,(-\nu'),(-\nu)})^* \\ \overset{(c)}{=} K_{3,p,i_1i_2}^{\Omega,\nu',\nu} \end{cases}$$

$$K_{3,t,i_1i_2}^{\Omega,\nu,\nu'} = \begin{cases} \overset{(a)}{=} K_{3,t,i_2i_1}^{-\Omega,\nu',\nu} \\ \overset{(b)}{=} (K_{3,t,i_1i_2}^{\Omega,(-\nu),(-\nu')})^* \\ \overset{(c)}{=} K_{3,t,i_1i_2}^{-\Omega,\nu,\nu'} \end{cases}$$

These relations can be used to significantly lower the numerical costs for the evaluation of the right hand side of the flow equations. In particular, knowing that all reducible vertices on all loop levels are symmetric under exchange of the outer vertices of the corresponding bubble functions, we can entirely dispense with calculating the class $K_{2'}$. Moreover, we use that:

- in K_1, it is sufficient to treat only positive bosonic frequencies,
- in K_2 and $K_{2'}$, it is sufficient to treat only positive frequencies for both, the bosonic and the fermionic, argument,
- in K_3, it is sufficient to treat only positive frequencies in the bosonic and the first fermionic argument. Since the relations also include exchange of the fermionic frequencies, it is furthermore sufficient to consider only those frequencies for the second fermionic argument whose absolute values exceed those of the first fermionic argument.

In fact, there is still room for simplifications: So far we have only argued that taking high frequency limits can cause certain diagrammatic classes to vanish. However, not only the frequency but also the lattice site arguments can have this effect. This can happen in two ways:

1. Since, in the Heisenberg model, $J_{ii} = 0$ is always true from the initial condition, any higher order diagram vanishes when one of its bare interactions is evaluated with both lattice site arguments being equal. This happens for instance in the second and third diagrammatc type of the t-channel (cf. Fig. 25) where one of the vertices touches only a single fermion line – if the frequency class is such that both external fermionic legs attached to this vertex merge in a bare vertex (which is then inevitably evaluated for twice the same lattice index), the whole diagram is always zero regardless of its detailed structure.
2. In the a- and in the p- channel, all vertices are evaluated with the same lattice site arguments. Therefore, all diagrams that do not belong to K_3 vanish when the external site arguments (i_1, i_2) correspond to a combination for which $J_{i_1i_2} = 0$ because in those cases, there is always at least one bare vertex that must be evaluated with a site combination for which it is zero.

These properties are of general nature and persist during all steps of the flow. In Table 2, we list the only diagrammatic classes that do not vanish for external site arguments (i_1, i_2) for which $J_{i_1 i_2} = 0$ (this condition is met for the vast majority of lattice site combinations when only nearest and next-to-nearest neighbor interactions are present in the Hamiltonian). A further source of simplification is the fact that only the spin part of the vertex can be nonzero in the initial condition. Since the spin- and the density part of bubble functions have different constituents (and thus different properties), it is sensible to distinguish between the spin and the density part in the table. All diagrammatic classes not appearing in the table need not be evaluated explicitly.

	a-channel	p-channel		t-channel	
Spin part	K_3	type 1	K_3	type 1	$K_1, K_2, K_{2'}, K_3$
		type 2	K_3	type 2	K_2, K_3
				type 3	$K_{2'}, K_3$
Density part	K_3	type 1	K_3	type 1	K_3
		type 2	K_3	type 2	K_3
				type 3	K_3

Table 2: This table lists the only diagrammatic classes that do not vanish for site-arguments (i_1, i_2) for which $J_{i_1 i_2} = 0$. It is valid at any step of the flow. In the p- and the t-channel, the types refer to the different diagrammatic contributions in these channels (cf. Figs. 8,25) and are labeled in the respective order of appearance in the formulae.

3.4.2 Symmetries and Parametrization of the Kagome Lattice

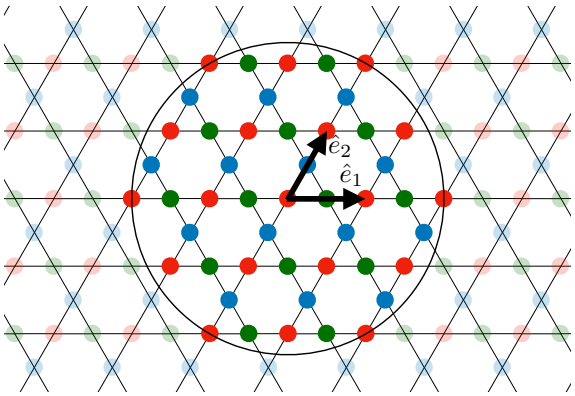

Fig. 11: The Kagome Lattice is a triangluar Bravais Lattice with a three-atomic unit cell. We only treat a finite number of lattice sites. Since the vertices depend only on *relative* real space coordinates if translational symmetries are not broken, the considered sites are defined in a circle centered around an arbitrary site.

The vertices only depend on the spacial distance of two lattice sites i_1 and i_2. Using invariance of the lattice under rotations about $\frac{\pi}{3}$ and translation along the unit vectors, one can always choose i_1 to be the origin such that the two site indices (i_1, i_2) can be replaced by a single effective site i_2'. On the Kagome lattice, where each unit cell contains three atoms, each site is characterized by three coordinates - two coordinates which indicate the unit cell and a third one specifying the lattice site within the given unit cell.
In the following, we use the notation

$$\vec{d} = \begin{pmatrix} a \\ b \end{pmatrix}_c ,$$

where a and b are translations along the unit vectors $\hat{e}_1$ and $\hat{e}_2$, respectively and $c \in \{1, 2, 3\}$ denotes the site within a given unit cell in the following correspondence to the picture: $1 \mathrel{\hat{=}}$ red, $2 \mathrel{\hat{=}}$ blue, $3 \mathrel{\hat{=}}$ green.

In order to obtain the effective site $\vec{i}_2'$, one needs to perform the following three steps:

- Translate the vector $\vec{i}_2$ by the vector that translates $\vec{i}_1$ to the first unit cell.
- Rotate the translated vector $\vec{i}_2$ in the following way: $(\vec{i}_2)^k \to (\hat{T}_{c_1})^{kl}(\vec{i}_2)^l$ with $c_1 \in \{1, 2, 3\}$ labeling the site pointed at by $\vec{i}_1$ within the first unit cell and $\hat{T}_{c_1}$ being defined as:

$$\hat{T}_1 = \begin{pmatrix} 1 & 0 \\ 0 & 1 \end{pmatrix} \qquad \hat{T}_2 = \begin{pmatrix} -1 & -1 \\ 1 & 0 \end{pmatrix} \qquad \hat{T}_3 = \begin{pmatrix} 0 & 1 \\ -1 & -1 \end{pmatrix}$$

.

- Simultaneously, shift the index c_2 in the range $(1, 2, 3)$ according to the rule:

$$\begin{cases} \text{not at all} & \text{for } c_1 = 1 \\ \text{one position in anticyclic sense} & \text{for } c_1 = 2 \\ \text{one position in cyclic sense} & \text{for } c_1 = 3. \end{cases}$$

The resulting new vector $\vec{i}_2'$ is physically equivalent to the initial vector $\vec{i}_2 - \vec{i}_1$ as this procedure amounts to a redefinition of the origin such that $\vec{i}_1 = \begin{pmatrix} 0 \\ 0 \end{pmatrix}_1$.

Another important operation is the inversion of two lattice sites: $\Gamma_{i_1 i_2} \to \Gamma_{i_2 i_1}$. Though this can be viewed as a special case of the above, it is worth pointing out the procedure.
The corresponding transformation starting from a vector $\vec{d} = \begin{pmatrix} a \\ b \end{pmatrix}_c$ is:

- Perform the rotation on the projected vectors: $(\vec{d})^k \to -(\hat{T}_c)^{kl}(\vec{d})^l$ where $\hat{T}_c$ are the matrices defined above.
- Simultaneously, shift the index c in the range $(1, 2, 3)$ according to the rule:

$$\begin{cases} 1 \to 1 \\ 2 \to 3 \\ 3 \to 2. \end{cases}$$

A third observation that can be made is the fact that every distance vector $\vec{d}$ with respect to the origin in the lower part of the plane has an equivalent in the upper part. Hence, it is sufficient to only explicilty consider those index combinations that correspond to lattice sites in the upper half. The relation between two equivalent vectors is a rotation around the origin by π. In terms of coordinates, the vector $\vec{d}'$ in the upper half can be obtained from a vector $\vec{d} = \begin{pmatrix} a \\ b \end{pmatrix}_c$ in the lower half by making the transformation:

$$\begin{pmatrix} a \\ b \end{pmatrix}_c \to \begin{pmatrix} -a \\ -b \end{pmatrix}_c - \begin{cases} \begin{pmatrix} 0 \\ 0 \end{pmatrix}_c & \text{for } c = 1 \\ \begin{pmatrix} 0 \\ 1 \end{pmatrix}_c & \text{for } c = 2 \\ \begin{pmatrix} 1 \\ 0 \end{pmatrix}_c & \text{for } c = 3. \end{cases}$$

In order to find an expression for the distance of an arbitrary site to the reference site at the origin, it is useful to write the distance vector in cartesian coordinates, where:

$$\hat{e}_1 = \begin{pmatrix} 1 \\ 0 \end{pmatrix} \text{ and } \hat{e}_2 = \frac{1}{2}\begin{pmatrix} 1 \\ \sqrt{3} \end{pmatrix}.$$

The distance vector is then given by: $\vec{d} = a \cdot \hat{e}_1 + b \cdot \hat{e}_2 + \vec{\Delta}_c$, where

$$\vec{\Delta}_c = \begin{cases} \vec{0} & \text{for } c = 1 \\ \frac{1}{2} \cdot \hat{e}_2 & \text{for } c = 2 \\ \frac{1}{2} \cdot \hat{e}_1 & \text{for } c = 3 \end{cases}$$

accounts for the appropriate shift according to the color. Hence:

$$\left|\vec{d}\right|^2 = (a + \tfrac{1}{2} \cdot b + \Delta_{c,1})^2 + (\tfrac{\sqrt{3}}{2} \cdot b + \Delta_{c,2})^2.$$

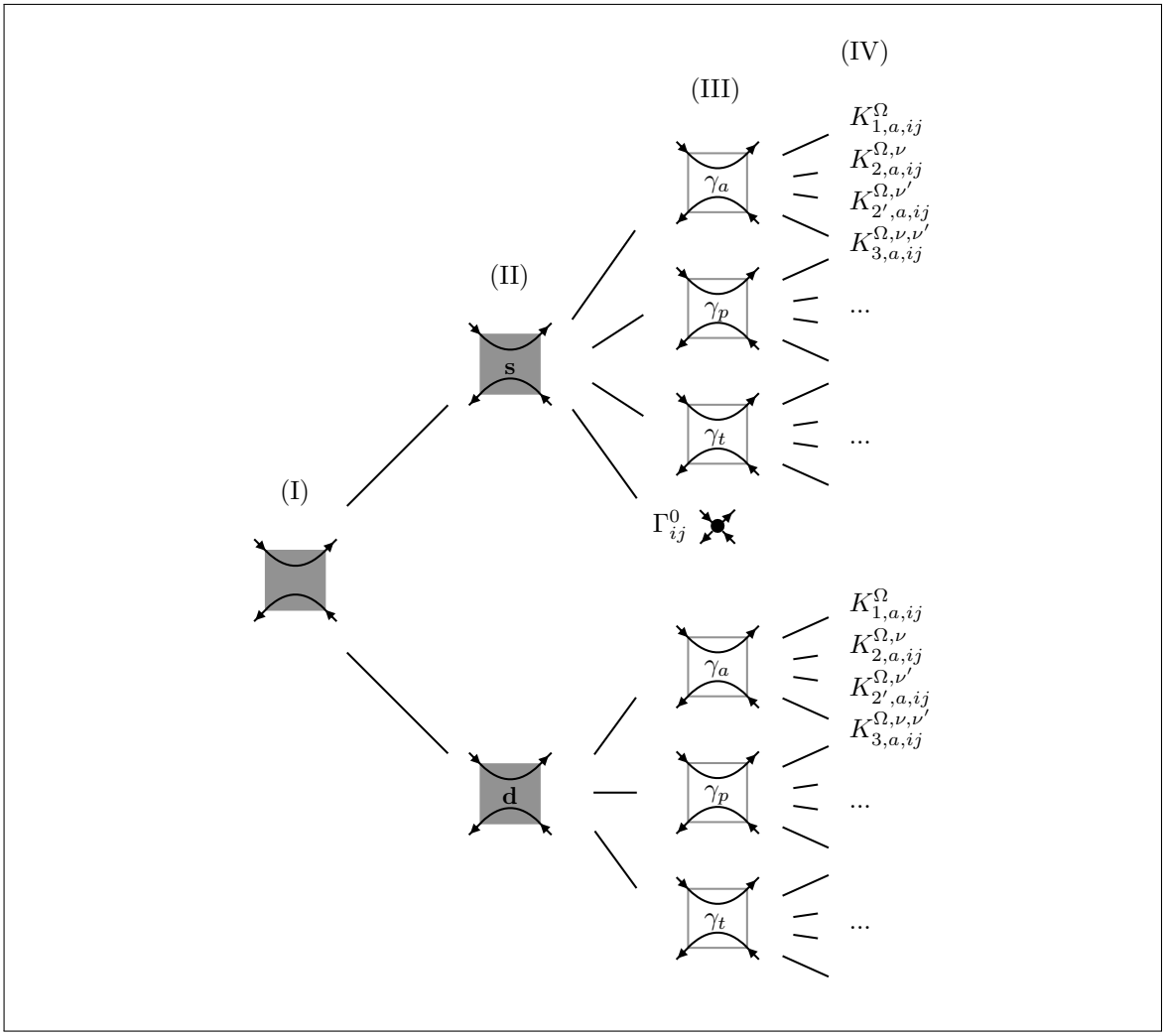

Fig. 12: Implementation of the decomposed vertex: A general vertex on level (I) consists of a spin and a density part (level (II)). Both parts are again decomposed on level (III) according to the channel classification. All 2PR-vertices contain more diagrammatic sub-classes corresponding to the high-frequency decomposition on level (IV). Note that there is no bare vertex in the density channel since it is always zero from the initial conditions and does not change during the flow.

3.5 Algorithmic Implementation

3.5.1 General Vertex

In order to benefit from the channel decomposition and the frequency asymptotics in the vertices, it is crucial that the implementation structure of the vertices satisfies certain requirements. Most prominently, it should allow for:

- Exploitation of channel dependent symmetries in the asymptotic classes (cf. Sec. 3.4.1),
- Uncomplicated and intuitive implementation of the effective loop and bubble functions (cf. Secs. 3.2.1/3.2.2) where the physical input is given by spin and density vertices without any specification as to the channel or the asymptotic decomposition,
- Efficient computation and storage of all individual asymptotic classes.

The most natural way to implement a general vertex with these properties is the structure shown in Fig. 12 which defines four levels of hierarchy. Performing calculations in the one-loop approximation without the channel decomposition (as done in Refs. [39,42] for instance) corresponds to working on level (II) with the vertex values being the sum of all subclasses. However, the calculation of higher

loop orders requires a more efficient parametrization where the high frequency asymptotics play a crucial role. In the following section, we argue that already inclusion of level (III) leads to enhanced accuracy without additional numerical costs and that the last level in the vertex structure allows for improved efficiency.
Our used convention of parametrizing the vertices in a channel-dependent way with one bosonic and two fermionic frequencies as introduced in Sec. 3.1.2 is a choice and different conventions for the frequency arguments are possible. If the parametrization of the vertices does not go beyond level (II), one does not have access to diagrams that are reducible in the individual channels and therefore, there is no way to account for the asymptotic behaviour of single diagrammatic subclasses. In this case, it is advisable to use a convention that does not favor any specific channel and to label *all* vertices with the same set of three frequency arguments that are either all bosonic (most naturally, these are the bosonic transfer frequencies $\Omega_a, \Omega_p, \Omega_t$) or fermionic and are defined in a cube around the origin. However, uniform frequency arguments unavoidably lead to the fact that one either limits the high-frequency content of the vertices in an uncontrolled way or needs to store a greater number of vertex values than necessary. In Fig. 13, we show the frequency points that are considered by defining a cube in purely bosonic (a) and purely fermionic (b) frequency parametrizations (drawn in yellow) and the frequency points that are accounted for when defining a cube of the same size in a mixed and channel-dependent coordinate system with $(\Omega_r, \nu_r, \nu_r')$ along the axes (blue shape). This illustrates that already extending the parametrization by the additional parametrization level (III) can improve accuracy: Certain areas of the yellow cube are not reached by the blue shape, meaning that the vertex values that are stored in this frequency range have little relevance in the specific channel due to the asymptotic behavior. On the other hand, the blue shape exceeds the yellow cube at some points which indicates that there are relevant values beyond the accessible frequency range in a uniform parametrization scheme.
Including level (III) with the three individual mixed frequency conventions ensures that all important contributions from the vertices are taken into account and that this source of error is avoided. Level

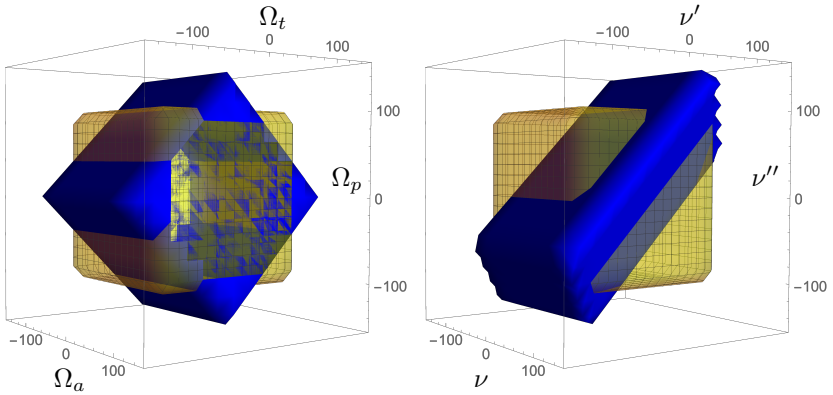

(a) Bosonic coordinate system. (b) Fermionic coordinate system.

Fig. 13: Yellow cube: Frequency points in a cube in a purely bosonic (a) and purely fermionic (b) coordinate system with $(\Omega_a, \Omega_p, \Omega_t)$ and (ν, ν', ν'') along the axes, respectively. Blue shape: Frequency points corresponding to a cube of the same size in a mixed coordinate system with $(\Omega_a, \nu_a, \nu_a')$ along the orthogonal axes, represented in the "pure" coordinate systems (a) and (b).

(IV) exploits the mixed parametrization as it allows to store the different asymptotic classes in different frequency ranges. Knowing that the K_3-class decays fastest, this allows for a very efficient calculation of vertex values for large frequency arguments where only the classes with a reduced frequency dependence, K_1, K_2 and $K_{2'}$, contribute.
Increasing the complexity of the vertex structure comes at the cost of the requirement for more sophisticated functions to efficiently read out the vertex values at different levels of the hierarchy. While in the most general case, the output function on each hierarchy level simply calls all output functions of the next higher level and returns their sum, the situation is more subtle when the vertices are part of bubble functions since the output functions should intrinsically know about the high frequency structure as will become clear in Sec. 3.5.3.
The next section will therefore be devoted to the implementation of bubble functions after which we will come back to the matter of reading out vertices in the context of bubble functions.

3.5.2 Bubble Functions

In correspondence to Sec. 3.2.2, there are two different parametrization levels of bubble functions: The unparametrized one (see left side of Eqs. (46,75,76)) takes two vertices on parametrization level (I) as input and effectively calls another bubble function that takes two vertices on parametrization level (II) as input (see right side of the equations, respectively) and performs the actual Matsubara sum. Consequently, we refer to them as "outer" and "inner" bubble function. Making the connection to the hierarchic structure of the vertex, they can be characterized by the levels between which they operate. Since, by definition, all bubbles in channel r belong the r-reducible diagrams, it will be convenient to introduce the level label ($\mathrm{I}^{(r)}$) which characterizes a vertex on level (I) with the special property that level (III) contains only a contribution in channel r, i.e. there is no further junction between level (II) and the r-reducible vertex on level (III). Let us start at the outer bubble function which is the algorithmic analogue of the bubble functions as they appear in most general flow equations from Fig. 24, and then move to the inner one:

Outer Bubble: Mapping between levels $\mathbf{I} \to \mathbf{I}^{(r)}$
On the "coarsest" parametrization level, the bubble functions should have a very simple form such that the flow equations can be transcribed in one-to-one correspondence from Fig. 24. Thus, they take exactly the information that is needed to describe all bubble functions appearing in the flow equations, which amounts to:

- Two vertices, Γ, Γ', on parametrization level (I),
- Two propagators which can individually be of the type G_Λ, S_Λ or $S_\Lambda + G_\Lambda \dot{\Sigma}_\Lambda G_\Lambda$,
- Information if one the vertices contains only complementary channels (c.f. loop orders $l > 1$). We refer to the variable containting this information as "complement".

In particular, no explicit external arguments (lattice sites and frequencies) are needed since the desired output of this function is the full vertex on level ($\mathrm{I}^{(r)}$) for *all* argument combinations.

Inner Bubble: Mapping between levels II $\to$ IV
As derived in Sec. 3.2.2, the inner bubble function should take combinations of the spin and density part, $\Gamma.\Gamma^s$ and $\Gamma.\Gamma^d$, as input. This function should allow to compute the values for the individual subclasses, i.e. the physical values that are stored as numbers. Following the logic from Ref. [54], the output would be an r-reducible vertex on level (III) – as outlined in Sec. 3.3, we could extract the asymptotic classes by taking appropriate limits in the external arguments of the kind $\nu, \nu' \to \infty$ when performing the Matsbuara sums and subtracting the resulting diagrams from each other in a way such that we are left with only level-(IV)-diagrams[16].
However, this is is the point where we suggest to modify their proposed procedure and to implement the inner bubble function such that it directly yields values for $K^{\vec{\omega}}_{n,r,\vec{R}}$, i.e. objects on level (IV), without the need to take limits and without the necessity to compute diagrams from which we then substract certain contributions that have been computed redundantly[17]. Before explaining our procedure in detail in the next paragraph, let us mention that this is not only a matter of algorithmic elegance but it has a precise practical advantage: The substraction of diagrams can lead to a significant loss of precision since in pf-fRG applications as ours, the values in the different asympotic classes can differ by multiple orders of magnitude with K_1 containing the largest and K_3 containing the smallest values. If the K_2 class is obtained from Eq. (48), where the formerly computed K_1-class is substracted componentwise in the next step, even small relative errors of the Matsubara sum (or integral at $T = 0$) have a substantial impact on the precision of K_2. Directly computing the class-(IV)-diagramms avoids this source of errors and nothing stands in the way of computing all values in all classes with the same relative precision.
In order to explain our algorithmic implementation of the "direct" approach, it is important to bring to the point why the matter of computing only the "needed" contributions is nontrivial and either

[16] See also Ref. [54] for details.
[17] It should be mentioned that the advantage of our algorithmic high frequency implementation over the one proposed in Ref. [54] relies on the fact that we have full access to all subclasses of the vertex at every step of the flow. In different approaches, such as DMF^{2}RG, where the starting point of the flow is obtained from DMFT (e.g. Ref. [49]), our procedure is not always applicable.

requires computing unwanted diagrammatic contributions that are subtracted afterwards or more intricate strategies:
As explained in Sec. 3.3, the asymptotic classification can be boiled down to the two criteria of whether the two pairs of external legs carrying the same fermionic frequency label are connected to the same bare vertex or not. If this is the case for both pairs (corresponding to K_1), the situation is easy because all diagrammatic contributions of a vertex that do not fulfill this condition vanish when the corresponding fermionic frequency is taken to infinity, i.e. taking the limit when performing the Matsubara sum eliminates all unwanted contributions from the vertices.
However, suppose we wish to compute a diagramm of the class K_2 where the external legs on Γ are not connected to the same bare vertex: we would need a way to suppress all contributions of Γ where both legs do touch the same bare vertex. In an r-bubble, these contributions are $K_{1,r}, K_{2',r}$ and the bare vertex Γ^0. This unveals the tricky point: These are precisely the contributions of Γ that do not depend on ν, the fermionic frequency attached to Γ. Hence, there is no way to get a handle on these contributions by modifying the external physical arguments.

The algorithmic implementation of the "direct" approach follows a simple strategy: When calling the inner bubble function, we define an extra argument carrying information about the asymptotic class that is computed which we refer to as "class"[18]. Knowing the two-particle channel in which a bubble is computed, one can deduce from this extra argument not only what channels in the two vertices Γ and Γ' can contribute to the asymptotic class we wish to compute but also what asymptotic subclasses of the relevant channels in Γ and Γ' contribute. Hence, the variable "channel" needs to be passed to the vertex output functions such that they do not return a simple sum of all subclasses but suppress the unwanted parts on which we do not have a handle. For the sake of conceptual coherence, we use this technique for all diagrammatic classes, even for $K_{1,r}$ where taking limits would do the job, such that no frequency limits are necessary in our algorithm. At this point it becomes clear that the actual heart of this approach is not part of the bubble functions themselves but must rather be implemented in the vertex output functions which we will therefore equip with the expertise to return only selected subclasses.
Before coming back to the vertex output functions in the context of bubble functions, there is one more subtlety that needs to be taken care of: On the right side of Eqs. (46,75,76), some vertices carry a tilde, indicating that they have been obtained from mapping a vertex with vertical fermion lines to one with horizontal lines (cf. Sec. 3.1.1). This mapping effectively interchanges the a- and the t-channel. Therefore, this is only relevant when dealing with bubbles in the a- or t-channel and when, in addition, one of the vertices contains only complementary channel contributions. In all other cases, interchanging the two contributions has no effect since they are summed up anyways which is always the case in the one-loop-approximation as mentioned earlier. Algorithmically, we define two additional variables containing information about the channel mapping for the two vertices, "map_Γ" and "$\text{map}_{\Gamma'}$", and one variable "complement" that signals the vertex output function if only complementary channels are considered for one of the vertices. Finally, since this function returns the value of a level-(IV)-object for a specific combination of arguments, we need to specify the external lattice sites and frequencies. All in all, the arguments required for the inner bubble functions are:

- Two vertices, each either $\Gamma.\Gamma^s$ or $\Gamma.\Gamma^d$, (parametrization level (II)),
- Two propagators,
- "complement",
- "class",
- "map_Γ" and "$\text{map}_{\Gamma'}$",
- Frequency and lattice site arguments.

3.5.3 Vertex in Bubble Function

With the structure of the bubble functions being established, it is now straight forward to determine the most sensible structure of the vertex output functions such that they return only the necessary

[18] It should be emphasized that our algorithm never computes a "general" bubble but *always* a specific asymptotic class $K_{n,r}$.

parts. There is no need to define an output function on level (I) since we are never interested in the sum of the spin and the density part of a vertex. Starting at level (II), the arguments and functionalities of the vertex output functions are listed in Table 3. The new argument "side" tells the vertex if it appears in a bubble as Γ or as Γ'. Note that the arguments "mapping" and "complement" are also relevant for the calculation of the second self energy correction. In cases where they are not needed, each output function returns the sum of their subclasses with no contributions being suppressed.

Level	Input	Functionality
(II)	$\vec{\omega}_r, \vec{R}$, channel, side,class, map_{side}, complement	Deduces from the last five arguments which two-particle channels – and if the totally 2PI vertex – in the vertex contribute and calls output functions on level (III) while passing on the arguments that further determine the relevant asymptotic classes.
(III)	$\vec{\omega}_r, \vec{R}$, channel[19], side[20], class[21]	Converts the frequencies to the natural frequencies if "channel" is different from the two-particle channel of the vertex. Calls output functions on level (IV) while suppressing specific asymptotic subclasses if the combination of "side" and "class" forbids them (cf. Sec. 3.3).
(IV)	$\vec{\omega}_r, \vec{R}$	Converts physical arguments to storage address using all symmetry relations and returns vertex value as number.

Table 3: Input and functionality of output functions on the different levels of the vertex hierarchy. The arguments "side", "class", "mapping", and "complement" are only needed when the vertex is part of a bubble function. See Fig. 14 for an example.

When numerically performing the Matsubara sums that appear in the inner bubble function, it is helpful to make the following observation in order to improve performance and accuracy:
In the vertices Γ and Γ' that enter the bubble $B_r^{\Gamma,\Gamma'}$, there are certain contributions that do not depend on the integration variable ν_1. These are:

- the totally 2PI vertex (which is the bare interaction in the parquet approximation)
- the diagrammatic class $K_{1,r}^{\Omega}$ in Γ and Γ'
- the diagrammatic class $K_{2,r}^{\Omega,\nu}$ in Γ
- the diagrammatic class $K_{2',r}^{\Omega,\nu'}$ in Γ'.

All other diagrammatic contributions vanish for large ν_1. From Table 1, one can deduce the maximal interval in which the ν_1-dependent part of the vertices in an r-bubble can give a contribution. However, these values are not static since they depend strongly on what diagrammatic subclasses the vertices Γ and Γ' contain and if the channel mapping from Eqs. (37,38) is relevant. The part of the sum beyond this interval simplifies to a Matsubra sum of two (regularized) propagators that are multiplied by the the product of the constant vertex contributions and depends only on the bosonic transfer frequency of the respective channel. This residual sum can be evaluated with strongly reduced numercial costs, in some instances (for the parts where the self energy has decayed sufficiently far and the effect of the regulator has vanished) even analytically.

[19] Denotes the channel r' to which the given frequencies refer.
[20] If the vertex is used in a bubble function, this argument indicates if this vertex is Γ or Γ' according to the definition in Sec. 3.2.2.
[21] If the vertex is used in a bubble function, this argument indicates what asymptotic class (cf. vertex level (IV)) is computed.

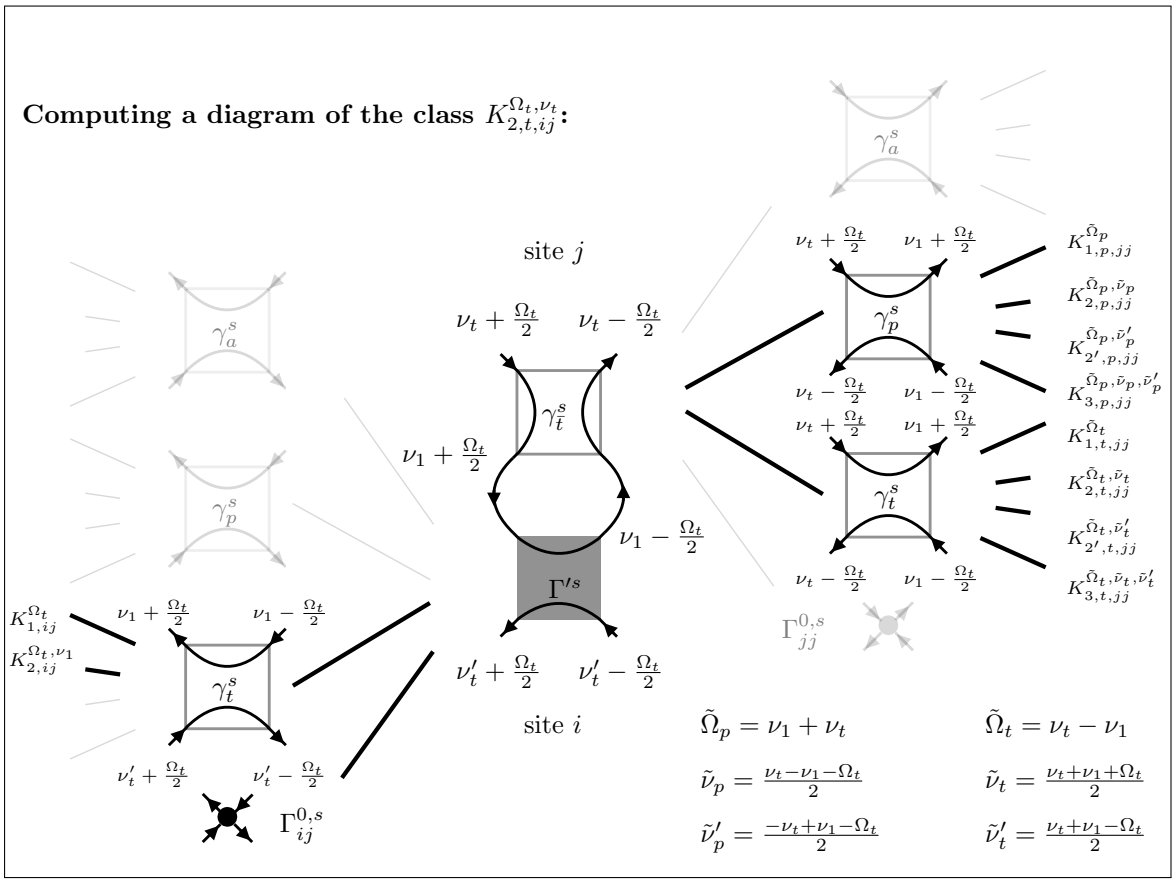

Fig. 14: Example of the algorithm for reading out the vertices in the computation of the diagram $K^{\Omega_t,\nu_t}_{2,t,ij}$ as it appears in the loop extensions in the t-channel. Note that the t-reducible part of the upper vertex is not read out with the initial t-channel arguments due to the channel mapping. The faint parts of the two vertices are suppressed in the "direct" approach. All diagrammatic constituents of this vertex depend on ν_t and are independent of ν'_t.

For all calculations, we use the same frequency discretization which is implemented as a combination of a logarithmic grid (for frequencies $|\omega| < 6.5$ with 16 discretized frequencies) and a linear grid reaching up to $|\omega| = 333.5$ and containing another 224 discretized frequencies. The grid is symmetric around $\omega = 0$ which is not contained itself. The logarithmic part, though small compared to the whole grid, allows for good resolution of the small frequencies (the smallest being $|\omega| = 0.1$) for which the vertex functions are typically quite vivid. For the individual asymptotic classes, we chose the following number of frequency points for each frequency axis: 34 (i.e. $|\omega|_{\max} = 32.7$) for K_3, 160 (i.e. $|\omega|_{\max} = 216.7$) for K_2 and $K_{2'}$ and 240 (i.e. $|\omega|_{\max} = 333.5$) for K_1. These values are such that the respective classes have largely decayed at the frequency bounds. In Fig. 15, we show plots of the K_3 class in all three channels for fixed bosonic frequency ($\Omega = 0.1$) and neigboring lattice sites as these arguments correspond to the greatest values in the vertex function. The fact that the K_3 class has almost completely decayed at the bounds implies that is it sufficient to consider only the other asymptotic classes outside of this frequency range.

Reading out the vertices for continuous frequencies requires interpolation between the values that are stored on the discrete grid. We use simple n-dimensional linear interpolation for the class

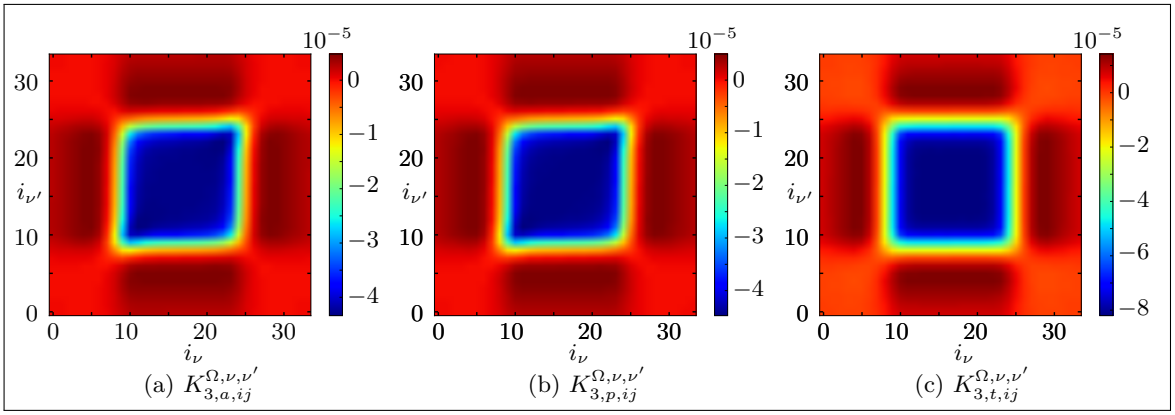

(a) $K^{\Omega,\nu,\nu'}_{3,a,ij}$ (b) $K^{\Omega,\nu,\nu'}_{3,p,ij}$ (c) $K^{\Omega,\nu,\nu'}_{3,t,ij}$

Fig. 15: Plot of the storage array for the K_3 class. The axes refer to the discrete frequency grid indices for the fermionic arguments – in this case we store 34 frequency points in each direction, i.e. $i_\nu = 17 \mathrel{\widehat{=}} |\nu|_{\min}$, where $|\nu|_{\min} = 0.1$ in our case. The values of the vertex function decay towards the bounds such that the K_3 class does not contribute significantly beyond this frequency range. These plots were made at the beginning of the flow with neigboring sites (i, j) and fixed bosonic frequency $\Omega = 0.1$.

K_n as proposed in Ref. [36]. For the class K_2, for example, the interpolation scheme reads:

$$\begin{aligned} K_2^{\Omega,\nu} = &\Big(K_2^{\Omega_<,\nu_<}(\Omega_> - \Omega)(\nu_> - \nu) \\ &+ K_2^{\Omega_>,\nu_<}(\Omega - \Omega_<)(\nu_> - \nu) \\ &+ K_2^{\Omega_<,\nu_>}(\Omega_> - \Omega)(\nu - \nu_<) \\ &+ K_2^{\Omega_>,\nu_>}(\Omega - \Omega_<)(\nu - \nu_<) \Big) \\ &\times \frac{1}{(\Omega_> - \Omega_<)(\nu_> - \nu_<)}, \end{aligned} \tag{60}$$

where $\Omega_{>(<)}$ and $\nu_{>(<)}$ are the frequencies on the discrete frequency mesh that lie directly above (below) the physical frequencies Ω and ν. This scheme is analogous in one and three dimensional frequency space with two and eight summands, respectively.

4 Results

In order to draw physical conclusions from the computed quantities, it is desirable to relate them to physical observables that are accessible in experiment. An important such quantity is the spin-correlation function $\chi_{ij}(\Omega)$ that is given by [36]:

$$\begin{aligned}
\chi_{ij}(\Omega) =& \int_0^\beta d\tau e^{i\Omega\tau} \left\langle T_\tau\{S_i^z(\tau)S_j^z(0)\}\right\rangle \qquad (61)\\
=&\frac{1}{\beta}\int_0^\beta d\delta_\tau \int_0^\beta d\tau e^{i\Omega\tau} \left\langle T_\tau\{S_i^z(\tau+\delta_\tau)S_j^z(\delta_\tau)\}\right\rangle \\
=&\frac{1}{\beta}\sum_{\substack{\omega_{1'}\omega_{2'}\\ \omega_1\omega_2}}\sum_{\alpha\beta\gamma\delta} \underbrace{\int_0^\beta d\delta_\tau e^{i\delta_\tau(\omega_{1'}+\omega_{2'}-\omega_1-\omega_2)}}_{\beta\delta_{\omega_{1'}+\omega_{2'},\omega_1+\omega_2}} \underbrace{\int_0^\beta d\tau e^{i\tau(\Omega+\omega_{1'}-\omega_1)}}_{\beta\delta_{\Omega,\omega_1-\omega_{1'}}} \times \\
&\times \frac{1}{\beta^2}\left\langle \overline{c}_{i,\alpha}(\omega_{1'})c_{i,\beta}(\omega_1)\overline{c}_{j,\gamma}(\omega_{2'})c_{j,\delta}(\omega_2)\right\rangle \frac{1}{4}\sigma^z_{\alpha\beta}\sigma^z_{\gamma\delta} \\
=&\frac{1}{4\beta}\sum_{\omega_{1'},\omega_{2'}}\sum_{\alpha\beta\gamma\delta}\left\langle \overline{c}_{i,\alpha}(\omega_{1'}-\tfrac{\Omega}{2})c_{i,\beta}(\omega_{1'}+\tfrac{\Omega}{2})\overline{c}_{j,\gamma}(\omega_2+\tfrac{\Omega}{2})c_{j,\delta}(\omega_2-\tfrac{\Omega}{2})\right\rangle \sigma^z_{\alpha\beta}\sigma^z_{\gamma\delta}, \qquad (62)
\end{aligned}$$

where we exploited time translation invariance ($\tau \to \tau + \delta_\tau$) in the second line to impose energy conservation. Moreover, the z-direction has been chosen arbitrarily which is possible due to $SU(2)$ symmetry. According to the definitions in Eqs. (30,31), performing all Wick contractions and evaluating the sums yields:

$$\chi_{ij}(\Omega) = \tfrac{1}{4\beta^2}\sum_{\omega_{1'}}\sum_{\substack{\alpha\beta\\ \gamma\delta}}\sigma^z_{\alpha\beta}\sigma^z_{\gamma\delta}\Bigg(\delta_{\gamma\beta}\delta_{\delta\alpha}\delta_{ij}\beta$$

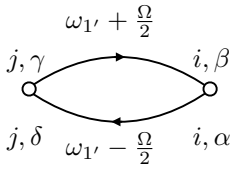

$+$

$+\sum_{\omega_2}\delta_{ij}$

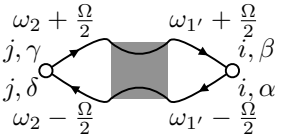

$-\sum_{\omega_2}$

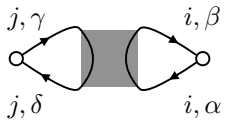

$\Bigg)$

$$= \tfrac{1}{4\beta^2}\sum_{\omega_{1'}}\Bigg(\beta\overbrace{\sum_{\substack{\alpha\beta\\ \gamma\delta}}\sigma^z_{\alpha\beta}\sigma^z_{\beta\alpha}}^{2}$$

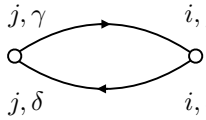

$\delta_{ij} + \overbrace{\sum_{\substack{\alpha\beta\\ \gamma\delta,\omega_2}}\sigma^z_{\alpha\beta}\sigma^z_{\gamma\delta}\sigma^\mu_{\delta\alpha}\sigma^\mu_{\beta\gamma}}^{-2}$

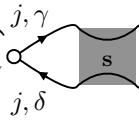

δ_{ij}

$+ \overbrace{\sum_{\substack{\alpha\beta\\ \gamma\delta,\omega_2}}\sigma^z_{\alpha\beta}\sigma^z_{\gamma\delta}\delta_{\delta\alpha}\delta_{\beta\gamma}}^{2}\delta_{ij}$

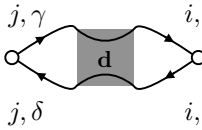

$- \overbrace{\sum_{\substack{\alpha\beta\\ \gamma\delta,\omega_2}}\sigma^z_{\alpha\beta}\sigma^z_{\gamma\delta}\sigma^\mu_{\beta\alpha}\sigma^\mu_{\gamma\delta}}^{4}$

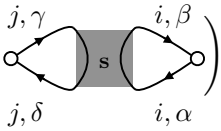

$\Bigg).$

Collecting everything, the formula for the spin-correlation function reads:

$$\begin{aligned}\chi_{ij}(\Omega) =& \frac{1}{4\beta}\sum_{\omega_{1'}} 2\cdot G(\omega_{1'}-\tfrac{\Omega}{2})G(\omega_{1'}+\tfrac{\Omega}{2})\delta_{ij} \\ &+ \frac{1}{4\beta^2}\sum_{\omega_{1'}}\sum_{\omega_2} G(\omega_{1'}-\tfrac{\Omega}{2})G(\omega_{1'}+\tfrac{\Omega}{2})G(\omega_2-\tfrac{\Omega}{2})G(\omega_2+\tfrac{\Omega}{2})\times \\ &\times\Big\{-2\cdot\Gamma^s_{ii}(\omega_2-\tfrac{\Omega}{2},\omega_{1'}+\tfrac{\Omega}{2};\omega_{1'}-\tfrac{\Omega}{2},\omega_2+\tfrac{\Omega}{2})\delta_{ij} \\ &+2\cdot\Gamma^d_{ii}(\omega_2-\tfrac{\Omega}{2},\omega_{1'}+\tfrac{\Omega}{2};\omega_{1'}-\tfrac{\Omega}{2},\omega_2+\tfrac{\Omega}{2})\delta_{ij} \\ &-4\cdot\tilde{\Gamma}^s_{ij}(\omega_{1'}+\tfrac{\Omega}{2},\omega_2-\tfrac{\Omega}{2};\omega_{1'}-\tfrac{\Omega}{2},\omega_2+\tfrac{\Omega}{2})\Big\}. \end{aligned} \tag{63}$$

The tilde on the last vertex can be dropped since the correlation function is always computed with the full vertex such that the tilde does not have an effect. Though diagramatically very reminiscent of the $K^{\Omega}_{1,r}$-class diagrams in the a and t-channel, the spin-correlation function in its spin-density parametrized form cannot immediately be obtained from the vertex values in the $K^{\Omega}_{1,r}$-class by a relation of the form $K^{\Omega}_{1,r,ij} \propto \chi_{r,ij}(\Omega)$ as opposed to the argument made in Ref. [54] for unparametrized diagrams. A simple way to understand this is to remember that $J_{ii} = 0$ in the Heisenberg model: When diagrams like the last one appear in the $K^{\Omega}_{1,r}$-class of any channel (where the end-points are bare vertices), they are either zero due to their site-index structure or they contain a summation over site indices, unlike the diagram that we wish to extract. It is worth noting that even in the case $J_{ii} \neq 0$ we would not be better off since with our classification of diagrams, even in that case we would not be able to extract only those diagrams without site-summations which prevents direct access to the correlation function in general and thus requires its separate evaluation. Ultimately, we are interested in the $\vec{k}$-space resolved static susceptibility which is given by the Fourier transform of the spin-correlation function in real space at $\Omega = 0$ [36, 45]:

$$\chi(\Omega=0,\vec{k}) = \frac{1}{3}\sum_{i_c\in\{1,2,3\}}\sum_j e^{i\vec{k}(\vec{R}_i-\vec{R}_j)}\chi_{ij}(0), \tag{64}$$

where the first sum denotes the sum over all atoms in the unit cell of an arbitrary site i and $\vec{R}_i, \vec{R}_j$ are vectors[22] corresponding to the sites i and j.
The susceptibility can easily be tracked during the flow and yields valuable information about the phase of the system. If the initial parameters are such that the systems has a magnetically ordered ground state, the susceptibility will diverge at specific vectors $\vec{k}$ as the energy scale is lowered. The position of these vectors reveals the kind of magnetic order by which the ground state is characterized. However, there are certain parameter regimes where the susceptibility shows no sign of divergence throughout the entire flow. These symmetry-preserving states are associated with spin liquid phases. In Fig. 16, we show an approximate phase diagram that contains four magnetically ordered states, as well as two spin liquid phases. It is plotted as function of the angle $\alpha = \arctan\left(\frac{J_2}{J_1}\right)$. One spin liquid phase is obtained for $J_2 \approx 0$ ("Heisenberg point") and the other one for $J_1 \approx 0$.

The magnetically ordered phases themselves are not accessible in the fRG scheme – we can only observe the divergencies as signs of phase transitions from a disordered to an ordered phase. The spin liquid phases, however, allow for further investigations: The main quantity of interest is the spacial decay of the spin-correlation since it allows to draw conclusions about the type of spin liquid. As mentioned in the introduction, the spin-correlation of a gapped Z_2-spin liquid phase would decay exponentially, $\propto \exp(-\frac{x}{\xi})$, with spacial distance x and correlation length ξ. The correlation length being accessible from the numerical data, one can determine the energy gap.
A gapless $U(1)$ spin liquid, on the other hand, would be identified by an algebraic decay of the form $\propto \frac{1}{x^d}$ with $d \approx 4$ [12]. Consequently, the long-distance correlations are much stronger than in gapped spin liquids.

[22] We recall that an index i is our notation for a vector $\vec{R}_i$ pointing site i which is parametrized by three coordinates.

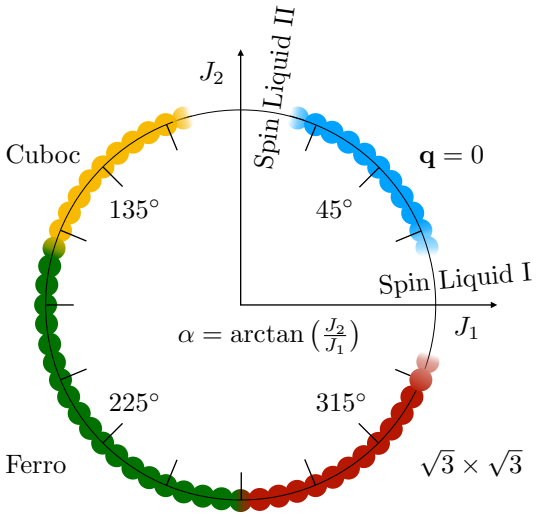

Fig. 16: Approximate phase diagram for the KHM as function of the angle $\alpha = \arctan\left(\frac{J_2}{J_1}\right)$ as obtained for example in Refs. [20, 47] (the exact positions of the boundaries are not consistent between different techniques).

4.1 Numerical Results

4.1.1 One-Loop Results

In Fig. 17, we present contour and surface plots of the susceptibility which show the characteristic diverging peaks shortly before the phase transition to the four ordered phases. In this figure, the susceptibility was computed from the 1-loop-renormalized vertex at the last Λ-integration step before the phase transition. The first (second) Brillouin zone is indicated with solid (dashed) lines in the contour plots. This way, it is easy to read off the vectors $\vec{k}$ at which the susceptibility diverges at the transition to the ordered phases[23]. Fig. 18 tracks the value of $\chi(\vec{k})$ at precisely these points down to the phase transition at specific values Λ_c (visible as divergencies in the curve or pronounced peaks) at which magnetic order sets in.
All calculations in the main part of this thesis have been performed with a correlation area of 181 sites which still allows for acceptable computation times at higher loop orders.

[23] These are: $\vec{k}_{\mathbf{q}=0} = \begin{pmatrix} 0 \\ \frac{4\pi}{\sqrt{3}} \end{pmatrix}, \vec{k}_{\text{cuboc}} = \begin{pmatrix} 0 \\ \frac{2\pi}{\sqrt{3}} \end{pmatrix}, \vec{k}_{\text{ferro}} = \begin{pmatrix} 0 \\ 0 \end{pmatrix}, \vec{k}_{\sqrt{3}\times\sqrt{3}} = \begin{pmatrix} 0 \\ \frac{8\pi}{3} \end{pmatrix}$.

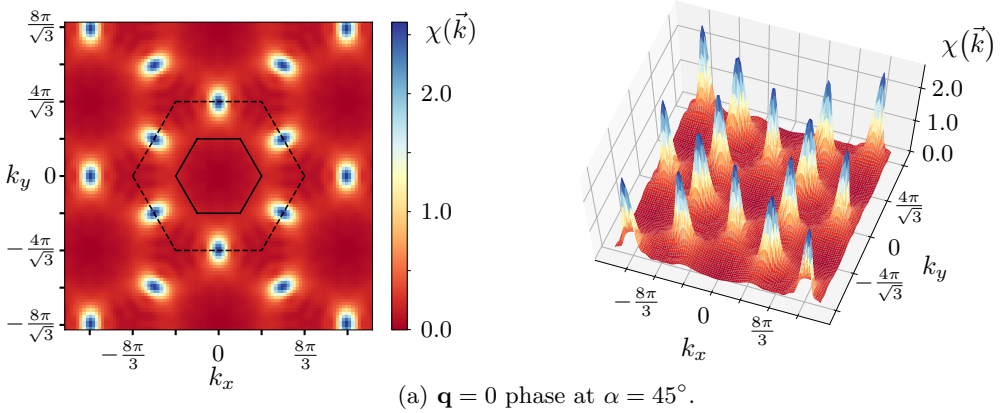

(a) $\mathbf{q} = 0$ phase at $\alpha = 45°$.

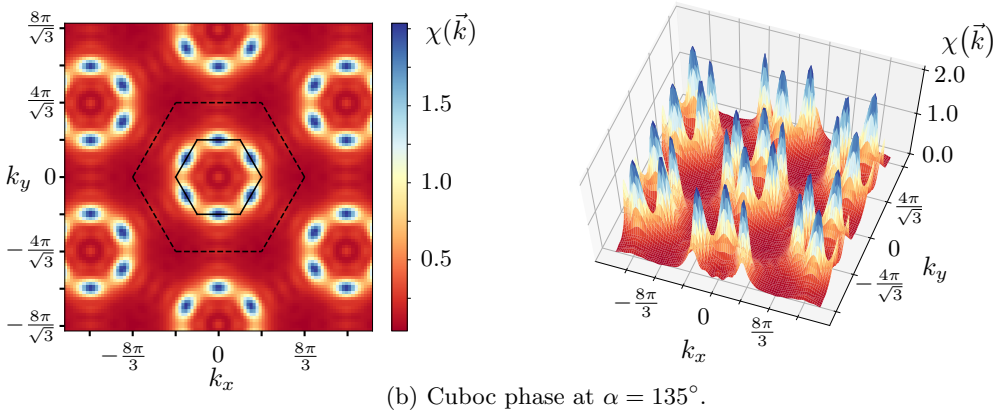

(b) Cuboc phase at $\alpha = 135°$.

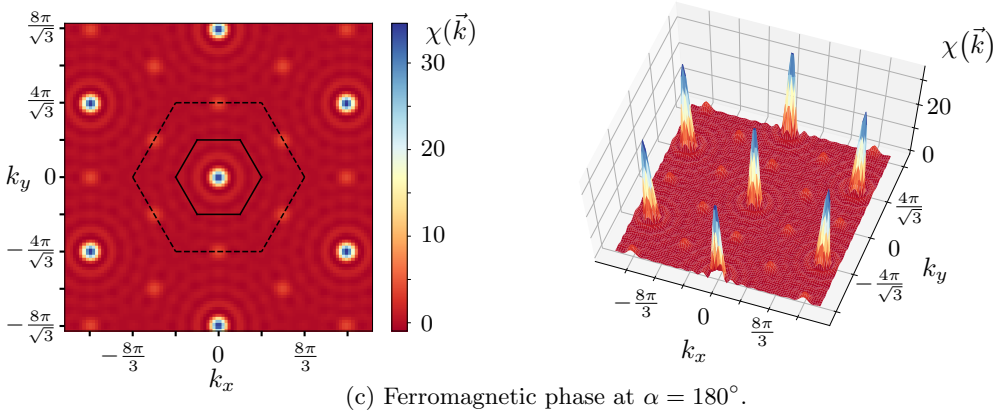

(c) Ferromagnetic phase at $\alpha = 180°$.

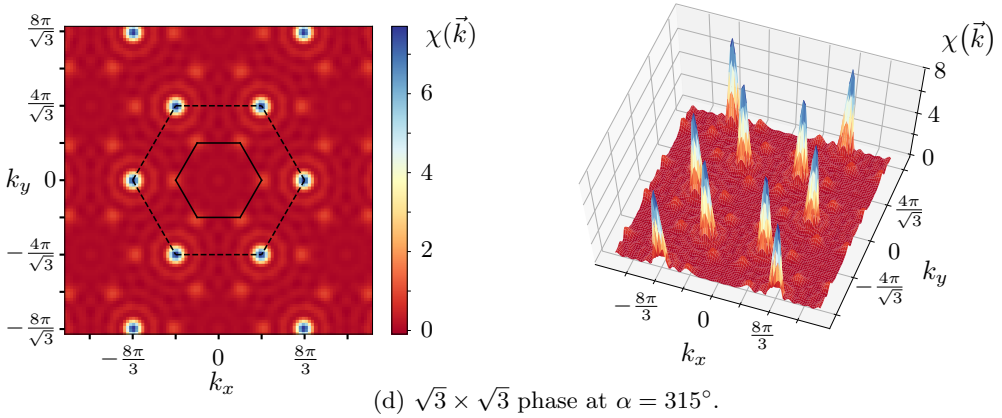

(d) $\sqrt{3} \times \sqrt{3}$ phase at $\alpha = 315°$.

Fig. 17: Contour plots (left) and surface plots (right) of the susceptibility shortly before the phase transition to the four different magnetically ordered phases. They were computed from the vertex in the one-loop flow.

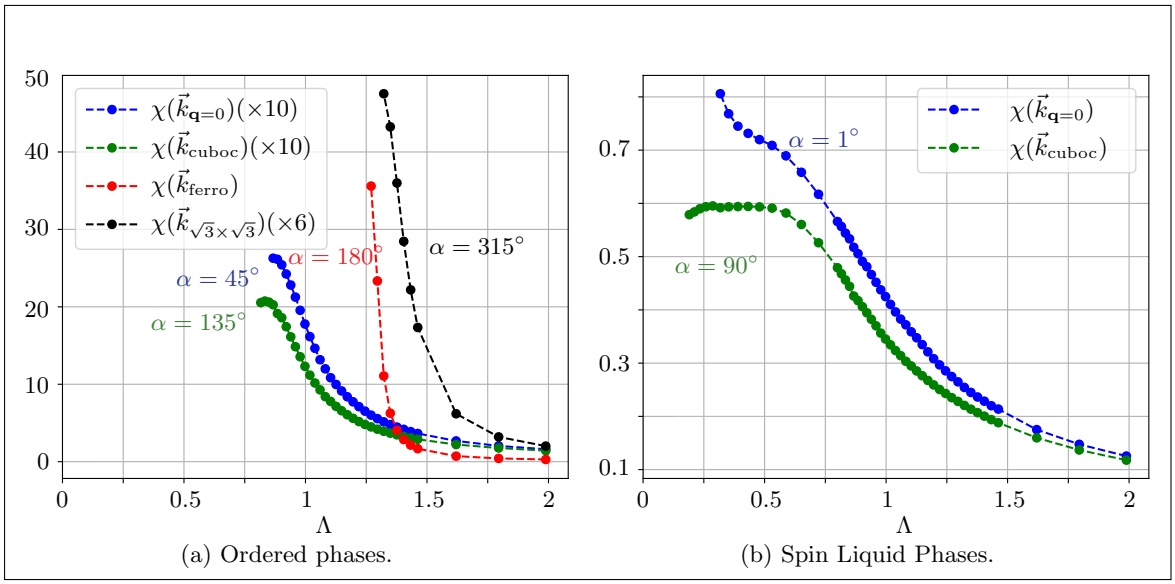

(a) Ordered phases. (b) Spin Liquid Phases.

Fig. 18: One-loop flow of the peaks in the susceptibility $\chi(\vec{k})$.

For the spin liquid regimes, the susceptibility looks quite different. Since no symmetry is broken, is it in principle possible to integrate the flow equation down to $\Lambda = 0$. In practice, our calculations for these phases end at some $\Lambda > 0$ below which the effects of the discrete frequency mesh does not allow for reliable data any more. The surface plots at the endpoints of the flow are shown in Fig. 19 for the two different spin liquid phases.

As mentioned before, it is of special interest to gain information about the kind of spacial decay that the spin-correlations exhibit. This information can directly be extracted from $\chi_{ij}(\Omega = 0)$ which we plotted in Fig. 20 as a function of distance, $x = |\vec{R}_i - \vec{R}_j|$, on a logarithmic scale and for the two different spin liquid phases.

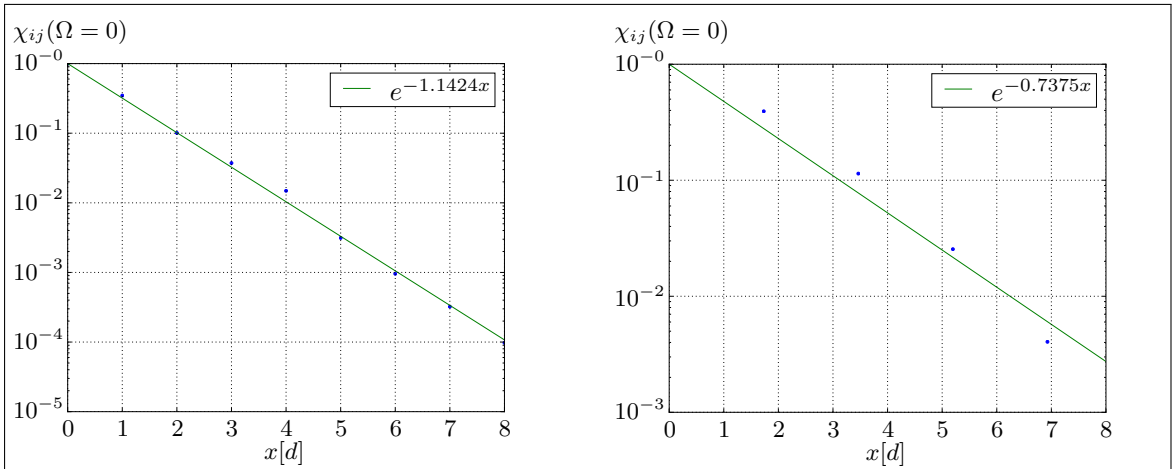

(a) Spin Liquid I at $\alpha = 1°$ and $\Lambda = 0.95$ along J_1-couplings, i.e. in the direction $\hat{n} = \hat{e}_1$.

(b) Spin Liquid II at $\alpha = 90°$ and $\Lambda = 0.35$ along J_2-couplings, i.e. in the direction $\hat{n} = \frac{2}{\sqrt{3}}(\hat{e}_2 - \frac{1}{2}\hat{e}_1)$.

Fig. 20: Real space decay of the spin-spin correlation, $\chi_{ij}(\Omega = 0)$. Spacial distance x is given in units of the nearest neighbor site distance $d = \frac{1}{2}|\hat{e}_i|$. The solid line is an exponential fit to the data.

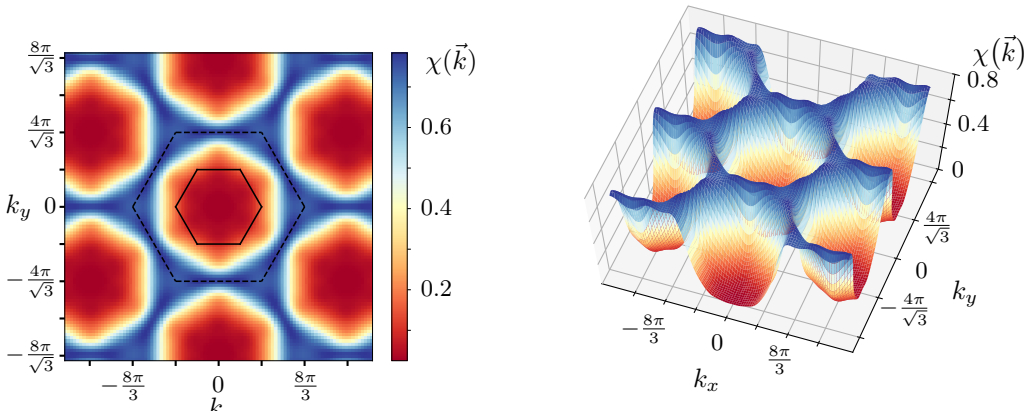

(a) Spin Liquid I close to the Heisenberg point, $\alpha = 1°$.

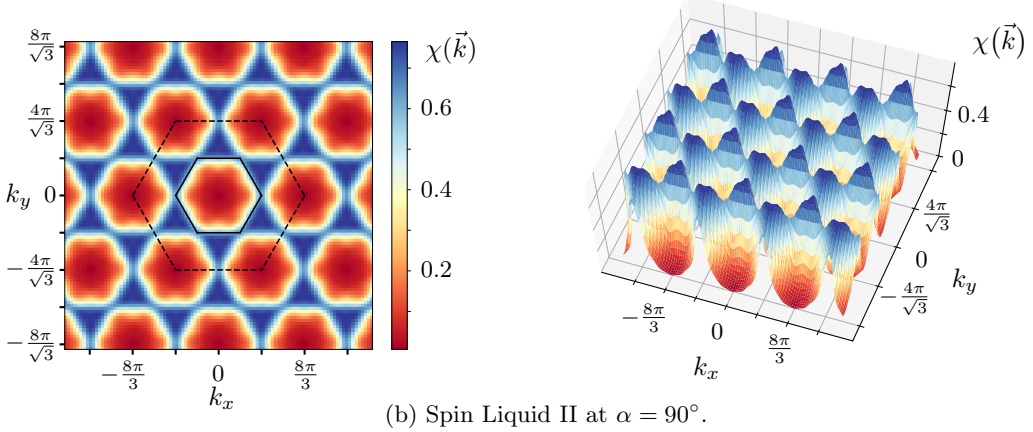

(b) Spin Liquid II at $\alpha = 90°$.

Fig. 19: Contour plots (left) and surface plots (right) of the susceptibility for the two different spin liquid phases. The susceptibility was computed at the end of the flow.

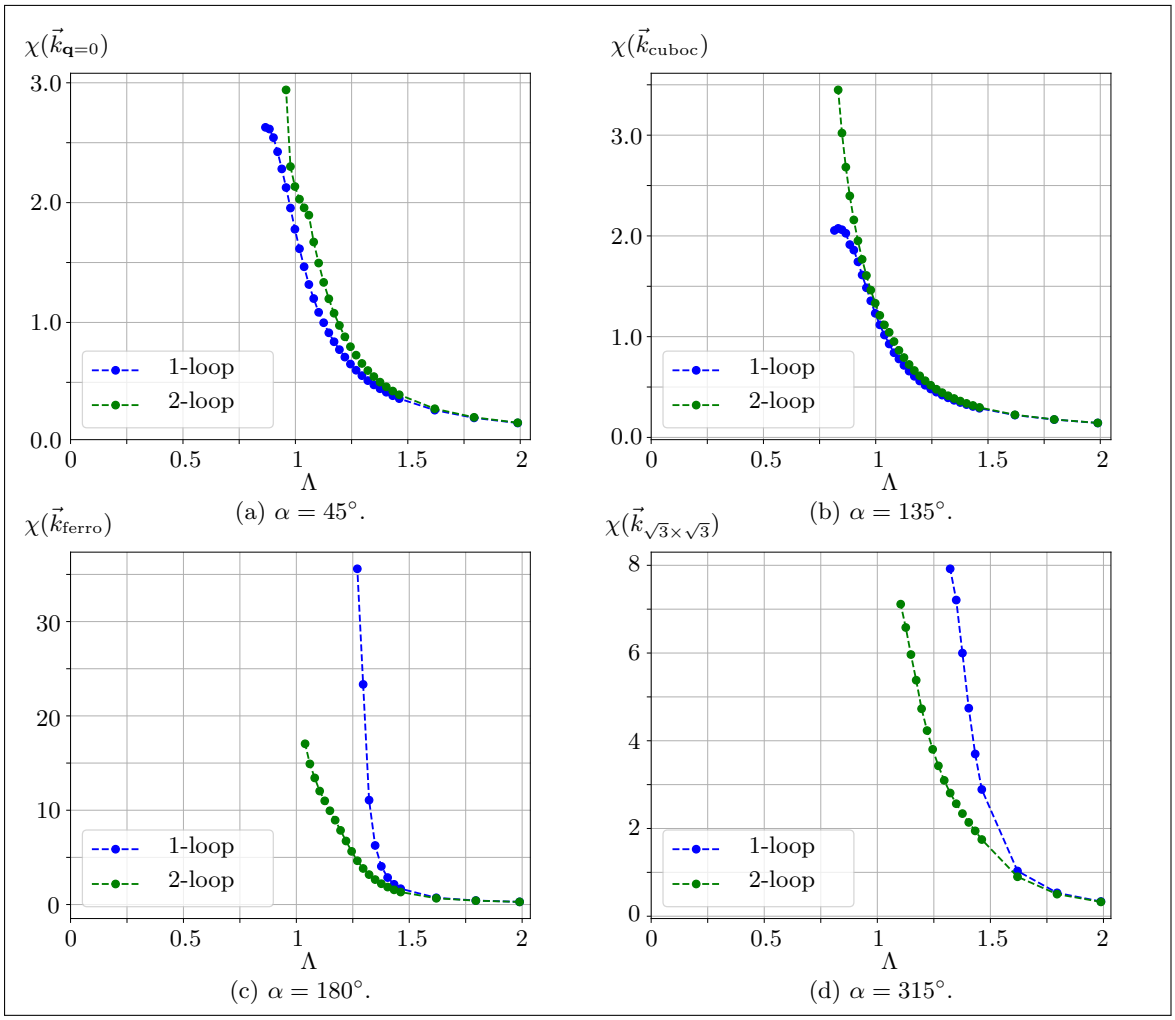

(a) $\alpha = 45°$. (b) $\alpha = 135°$. (c) $\alpha = 180°$. (d) $\alpha = 315°$.

Fig. 21: Two-loop flow of $\chi(\vec{k})$ deep in the ordered phases.

4.1.2 Two-Loop Results

Even though the algorithm described in this thesis is in principle applicable to arbitrary loop orders, computation times make higher loop orders quite costly. Within the scope of this thesis, we therefore limit ourselves to the investigations of two-loop corrections, leaving the analysis of higher loop orders for future analyses. The two-loop results are presented in this section.
It is primarily interesting how the boundaries of the phase diagram are affected by the second loop orders. Since the qualitative features from Figs. 17 and 19 are unchanged at higher loop orders, we do not show the corresponding contour and surface plots but focus on the more interesting flow of $\chi(\vec{k})$ at the relevant vectors $\vec{k}$. In Fig. 21, we show this flow towards the four ordered phases.

Figs. 22 and 23 show the flow of $\chi(\vec{k})$ for selected angles at the boundaries in the phase diagram where previous fRG studies have not been conclusive [5, 47] or do not match with the analysis from different methods as DMRG [20].

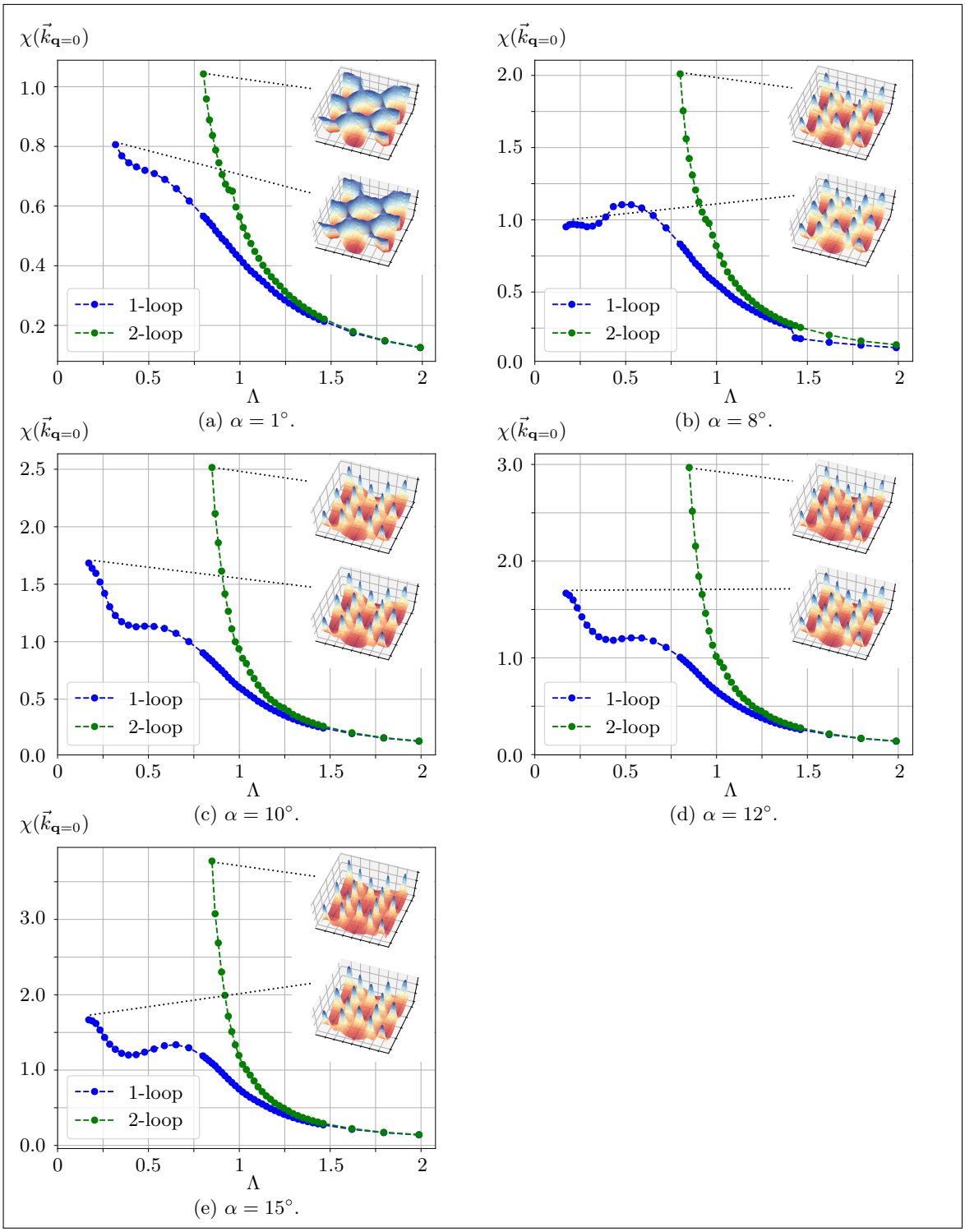

(a) $\alpha = 1°$. (b) $\alpha = 8°$.

(c) $\alpha = 10°$. (d) $\alpha = 12°$.

(e) $\alpha = 15°$.

Fig. 22: Flow of $\chi(\vec{k})$ at $\vec{k} = \vec{k}_{\mathbf{q}=0}$ for different angles α at the boundary of the $\mathbf{q} = 0$ phase.

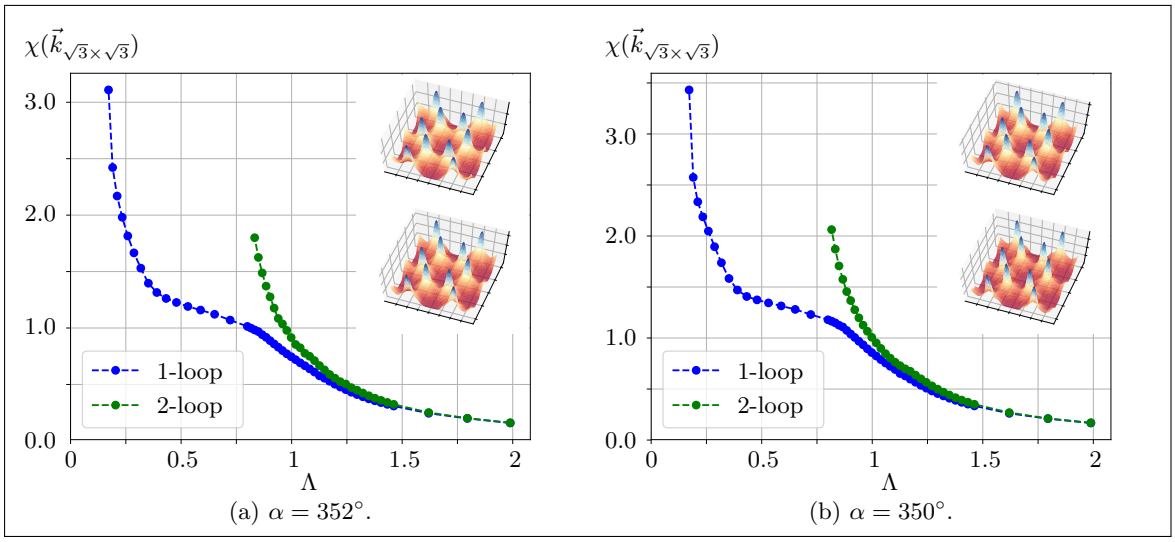

(a) $\alpha = 352°$. (b) $\alpha = 350°$.

Fig. 23: Flow of $\chi(\vec{k})$ at $\vec{k} = \vec{k}_{\sqrt{3}\times\sqrt{3}}$ for different angles α at the boundary of the $\sqrt{3} \times \sqrt{3}$ phase.

4.2 Discussion

Let us interpret the results from Secs. 4.1.1 and 4.1.2 and put them into perspective with previous works.
In the one-loop case, the different magnetically ordered phases can be identified by the characteristic shapes of the susceptibility in Fig. 17. We reproduce the four magnetically ordered phases that have been obtained in previous studies with different methods (e.g. Refs. [5, 20, 47]). In particular, the order of the critical values Λ_c at which the susceptibility diverges in these phases is in agreement with the fRG-results from Ref. [47], see Fig. 18a. Note that we amplified some of the curves for better visibility. The ordered phases at $\alpha = 45°$ ($\mathbf{q} = 0$) and $\alpha = 135°$ (cuboc) show less pronounced peaks which can be explained by a smaller magnetization in theses phases as compared to the other two magnetic phases [47].
The susceptibility in the non-magnetic case has no diverging peaks. The plots for both spin liquid phases in Fig. 19 were taken at the value of Λ down to which we computed the flow. In principle, the flow can be continued to $\Lambda = 0$ since no phase transition (and thus no divergence in the susceptibility) occurs (cf. Fig. 18b). In practice, however, our flow stops at some $\Lambda > 0$ where the discreteness of the frequency mesh prevents us from obtaining reliable data for smaller values of the flow parameter. This issue should be resolved for future projects where an adaptive grid may be useful.
By comparing the contour plots of the two spin liquid phases, it is easy to see their resemblance: The pattern in the contour plot from SL II is the essentially same as the one from SL I, rotated about $\frac{\pi}{6}$ and strechted by a factor $\frac{1}{\sqrt{3}}$. This can be understood by looking at the real space Kagome lattice and realizing that the distance between next-to-nearest neighbors is by the factor $\sqrt{3}$ larger than the one between next neighbors. Since the two spin liquids phases arise around the limits $J_2 = 0$ (i.e. only nearest neighbor interaction for SL I) and $J_1 = 0$ (i.e. only next-to-nearest neighbor interaction for SL II), it is intuitive that the susceptibilities in reciprocal space are related by the factor $\frac{1}{\sqrt{3}}$.

The real space decay of the susceptibility (Fig. 20) is best fitted by an exponential decay, though we emphasize that the plot for SL I was obtained at quite large Λ since our plots showed an increasingly random distribution at later points in the flow. Nonetheless, this is strong indication for Z_2 gapped spin liquid ground states for which we determined correlation lengths (in units of neighboring spin distance) of $\xi = 1.1424$ for SL I and $\xi = 0.7375$ for SL II. Since most numerical studies have focused on the SL I phase, we compare our value to the literature values for SL I:
The fRG analysis in Ref. [47] finds $\xi = 0.98$ while DMRG methods find $\xi \approx 0.8$ [17], $\xi \approx 1.0$ [6], and $\xi \approx 1.5$ [55] such that our value is perfectly in line with the reference values that all hint at very short ranged spin-spin correlations.

In the literature, however, the phase diagram from fRG studies is quantitatively not in total agreement with other methods – especially DMRG predicts slightly different locations of the phase boundaries. We shall focus on this point more thoroughly with the example of the phase transition from the Spin Liquid I-phase around the Heisenberg point to the $\mathbf{q} = 0$-phase:
While one-loop fRG in Ref. [47] predicts this boundary to be located at $\alpha \approx 35°$, DMRG detects the boundary at $\alpha \approx 11°$ [20]. We computed the flow of the susceptibility for several angles in the range $\alpha \in [1°, 15°]$ in order to investigate the effect of two-loop corrections, hoping for indication if higher loop orders may be able to reconcile the disagreeing results. In agreement with Ref. [47], our one-loop flow remains smooth throughout the entire flow for all angles in this range. However, adding two-loop corrections changes the flow such that the tendency for magnetic order is enhanced, see Fig. 22. In this figure, we plotted the flow of the highest points of $\chi(\vec{k})$ for the one- and two-loop scheme with an inset that shows the susceptibility at the last computed steps of the flows. When the curves become to steep, we are not able to integrate any further and more refined integration schemes with an adaptive step size would be needed to continue the flow. Even though the curve in the two-loop scheme at $\alpha = 1°$ becomes quite steep (which may hint at a phase transition that is certainly unexpected in this regime), the inset shows that no peaks and thus no magnetic order is developed as far as we can compute the flow with our current numerical integration technique.
This is different for the other angles in this figure where surface plots of the susceptibility show a clear tendency towards order in the $\mathbf{q} = 0$-phase. However, while the peaks never diverge in the one-loop scheme, they grow quite fast in the two-loop corrected flow. The greater the angle, the

more does the two-loop corrected curve deviate from the one-loop curve, strongly hinting at a phase transition. This makes it plausible that higher order correction indeed shift the one-loop-fRG results towards the reference values from the cited DMRG studies.

We make a similar observation close to the transition from the SL I phase to the $\sqrt{3} \times \sqrt{3}$-ordered phase. Fig. 23 again shows the flow of the highest point in the susceptibility. While fRG predicts the phase boundary to lie at $\alpha \approx 333°$ [47], the analysis from DMRG in Ref. [20] yields a value of $\alpha \approx 354°$. Our results at two angles within the range of discrepancy (at $\alpha = 352°, 350°$) show a one-loop flow that stays smooth for a long time and shows a sign of divergence only very late in the flow where the reliability of our data is poor due to effects from the discreteness of the frequency mesh. The two-loop corrected results, however, diverge a lot earlier in the flow, indicating that these angles of the phase diagram may indeed correspond to an ordered phase as predicted by DMRG [20]. The surface plots of the susceptibility (see insets in Fig. 23) show the clear signature of the $\sqrt{3} \times \sqrt{3}$-ordered phase.

5 Summary and Outlook

In this thesis, we presented our algorithm for a pf-mfRG analysis of the Heisenberg model on the Kagome lattice with nearest and next-to-nearest neighbor interactions. The difference with respect to former fRG algorithms (as in Ref. [39]) is the implementation of two additional vertex parametrization levels which allows for an efficient vertex parametrization by accounting for the frequency asymptotics of the vertex functions [54]. We used our algorithm to compute the phase diagram of the ground state in the KHM at $T = 0$ and reproduced the results from previous fRG studies [47]. Furthermore, we obtained second-order results at the points of the phase diagram where previous fRG studies were in disagreement with the results from other methods, especially DMRG (see Sec. 4.2 for the references that we considered). Our results show that two-loop corrections significantly alter the quantitative predictions concerning the transition points in the phase diagram. The presented data awakens the hope that higher order corrections my indeed lead to a better quantitative agreement of fRG studies with the DMRG reference values.
In addition, our findings confirm the predicition from former fRG studies regarding the Z_2-nature of the spin liquid ground state. Clearly, the goal is to explore the effects of higher order corrections in future projects which could not be considered on a structured way in the scope of this thesis due to time limitations that conflicted with computation times. Preliminary results for third-order corrections, however, seem to yield curves that lie between the first and the second order result. The hope is that the curves converge in the next few loop orders.
In order to find an estimate for the reliablity of the quantitative results, some technical points might be interesting to consider in future projects.
As a check, it would be helpful to explicitly show the regulator-independence of the mfRG flow. One possibility for another regulator that could be implemented is a smooth version of the widely used Litim regulator:

$$(G_{0,\Lambda}^{\text{Litim}})^{-1}(\omega) = i\,\text{sgn}(\omega)\max(|\omega|,\Lambda) \xrightarrow{smoothen} i\omega - i(\omega-\Lambda)e^{-\left(\frac{|\omega|}{\Lambda}\right)^2}. \tag{65}$$

It is expected that different realizations of the regulator lead to quite different quantitative results at low loop orders but converge to the same values when the loop number is increased.
Moreover, it would be interesting to implement the susceptibility as its own independent flow equation in the multiloop scheme as suggested in Ref. [22] and implemented in Ref. [48] for the 2D-Hubbard model. This would allow for a better understanding of the quantitative validity of the standard pf-fRG procedure where the susceptibility has so far always been computed from flowing vertices as "post-processed" quantity.

These being technical perspectives, it seems promising to apply the pf-mfRG algorithm to further models that exhibit magnetic frustration. In recent years, pf-fRG studies have also been pursued in 3D materials [16] with interesting examples being Heisenberg models on the hyperkagome [5] and the pyrochlore lattice [15]. These systems are numerically challenging and other methods fail here: Monte Carlo methods struggle with the sign problem and DMRG, which is well-suited for 1D and has successfully been generalized to 2D for certain systems, is generally not applicable in 3D. The functional renormalization group, however, is in principle not limited to a certain dimensionality and has proven successful. Since previous studies have not implemented multiloop corrections and the quantitative results therefore always depend on the choice of regulator, the pf-mfRG scheme could be used to improve the quantitative accuracy for this kind of systems.

In conclusion, it is probably safe to say that there are many remaining questions in the field of frustrated magnetism where pf-mfRG could help to complete the picture and understand interesting effects which makes this method very promising for future research in the field.

6 Acknowledgement

I am greatly indebted to Prof. Matthias Punk who – after arousing my fascination for Many body physics in his CMP lectures – proposed this exciting topic to me and supported me troughout the process of this thesis in many ways. I very much appreciated his open door and his general openness for discussions, be it about technical details or the "big" physical picture, from which I learned a lot. This made this year very enjoyable and triggered my lasting interest in this field.
Moreover, I am very thankful for the incredible support from Fabian Kugler who gave me valuable insights into (multiloop) fRG and shared very helpful ideas for the algorithmic implementation in countless discussions, e.g. by making me aware of the benefits from the high frequency asymptotics or pointing out helpful literature.
Many thanks also to Prof. Jan von Delft who showed great interest in my project from the beginning, initiated the collaboration with other fRG-practicioners in his group and supported me in discussions from which I always drew great motivation.
Furthermore, I would like to express my appreciation for the discussions with Prof. Yasir Iqbal who drew my attention to the discrepancies between former fRG studies and other methods and provided helpful ideas.
Thanks to all members of the chair for the warm and stimulating atmosphere that I enjoyed every day.

Appendices

A Two-particle Vertex Flow Equations in the mfRG Scheme

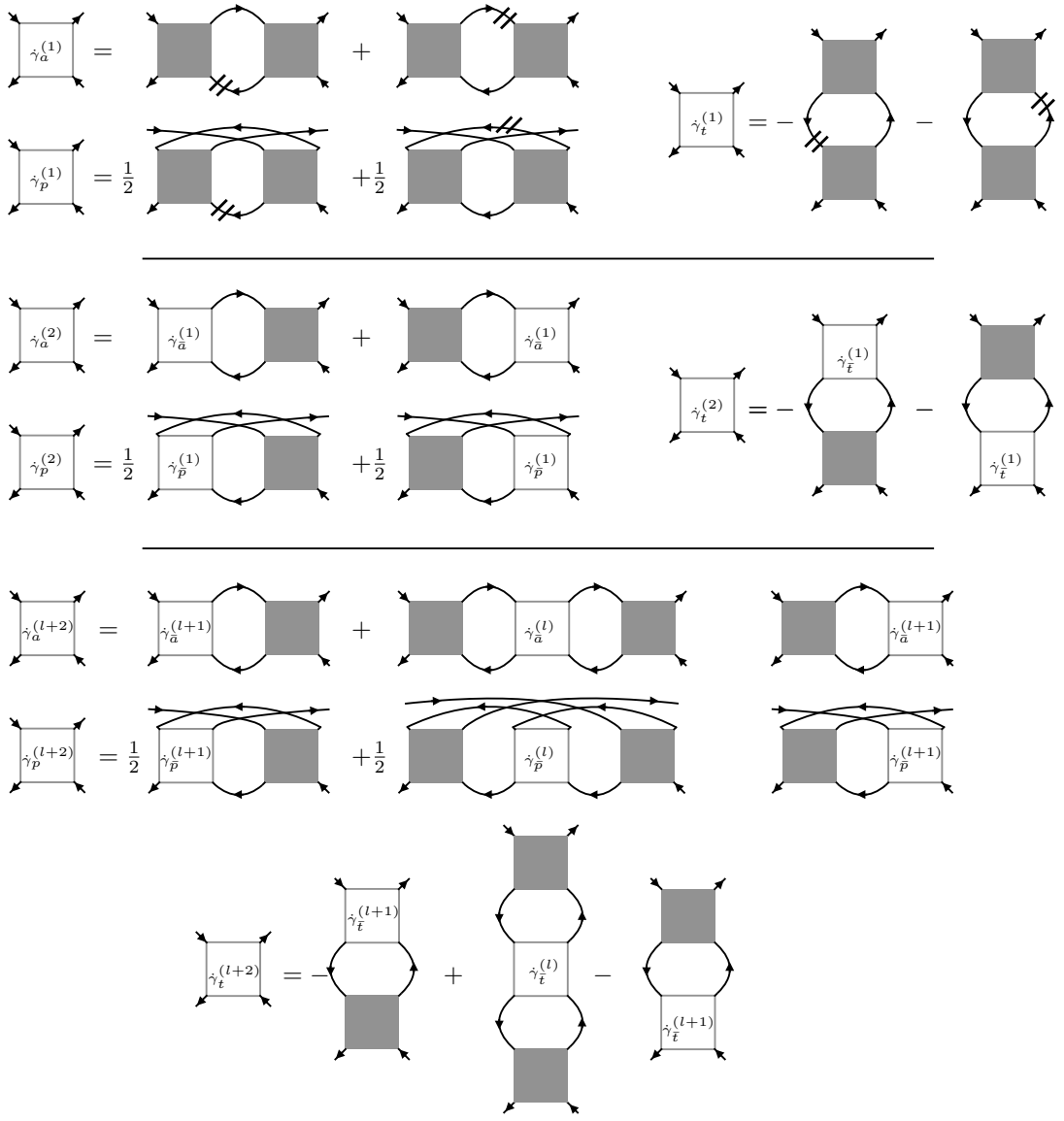

Fig. 24: Two-particle vertex flow equations in the mfRG scheme for the first, second and $(l+2)$th loop order. Double dashed lines denote the differentiated propagator $\partial_\Lambda G_\Lambda$. These diagrams relate to Eq. (23) by $\dot{\gamma}_r = \sum_l \dot{\gamma}_r^{(l)}$. Adopted from Ref. [23].

B Vertex Spin Parametrization

In correspondence to the real space parametrization in Eq. (33), it would be straightforward to introduce the spin parametrization of the vertex in the following way:

$$\Gamma_{i_1 i_2}(1'2';12) = \left\{\Gamma^x_{i_1 i_2}(\omega_{1'}\omega_{2'};\omega_1\omega_2)\delta_{\sigma_{1'}\sigma_1}\delta_{\sigma_{2'}\sigma_2} + \Gamma^y_{i_1 i_2}(\omega_{1'}\omega_{2'};\omega_1\omega_2)\delta_{\sigma_{2'}\sigma_1}\delta_{\sigma_{1'}\sigma_2}\right\}. \tag{66}$$

Let us make clear how this is related to the parametrization from Ref. [39] as introduced in the main text:

$$\Gamma_{i_1 i_2}(1'2';12) = \left\{ \Gamma^s_{i_1 i_2}(\omega_{1'}\omega_{2'};\omega_1\omega_2) \underbrace{\sigma^\mu_{\sigma_{1'}\sigma_1}\sigma^\mu_{\sigma_{2'}\sigma_2}}_{2\delta_{\sigma_{1'}\sigma_2}\delta_{\sigma_{2'}\sigma_1}-\delta_{\sigma_{1'}\sigma_1}\delta_{\sigma_{2'}\sigma_2}} + \Gamma^d_{i_1 i_2}(\omega_{1'}\omega_{2'};\omega_1\omega_2)\delta_{\sigma_{1'}\sigma_1}\delta_{\sigma_{2'}\sigma_2} \right\}. \tag{67}$$

By comparing proportionalities, one can make the identification:

$$\Gamma^x = -\Gamma^s + \Gamma^d \tag{68}$$
$$\Gamma^y = 2\Gamma^s \tag{69}$$

In order to see that both approaches are equivalent (i.e. a translation between the two is possible at any step of the flow), we examplarily compute the combinatorial factors for an a-bubble in the "x-y-parametrization" and demonstrate the equivalence to the bubble as computed in the "spin-density-parametrization".
In symbolic notation, we obtain:

$$B_a = \underbrace{GG\Gamma^x\Gamma^x}_{B^x}\delta_{\sigma_{1'}\sigma_1}\delta_{\sigma_{2'}\sigma_2} + \underbrace{GG(\Gamma^y\Gamma^x + \Gamma^x\Gamma^y + \Gamma^y\Gamma^y)}_{B^y}\delta_{\sigma_{1'}\sigma_2}\delta_{\sigma_{2'}\sigma_1}. \tag{70}$$

Substituting relations (68) and (69) in order to eliminate Γ^x and Γ^y yields:

$$B^x = GG(\Gamma^s\Gamma^s - \Gamma^s\Gamma^d - \Gamma^d + \Gamma^d\Gamma^d) \tag{71}$$
$$B^y = GG(4\Gamma^s\Gamma^s + 2(\Gamma^d\Gamma^s + \Gamma^s\Gamma^d)) \tag{72}$$

Using relations (68) and (69) again in order to tranlate B^x and B^y to B^s and B^d, we finally arrive at:

$$B^s = GG(2\Gamma^s\Gamma^s + \Gamma^d\Gamma^s + \Gamma^s\Gamma^d) \tag{73}$$
$$B^d = GG(3\Gamma^s\Gamma^s + \Gamma^d\Gamma^d), \tag{74}$$

which is precisely what we obtain for the a-bubble in the spin-density parametrization (see Appendix C). Hence, Eqs. (68) and (69) hold also for the bubble functions themselves. This calculation is completely analogous in the other channels and the same idea can straight forwardly be used for the self energy. Since all vertices are built up iteratively from bubble functions, these relations must hold for any vertex such that the parametrizations can always be switched. For practical purposes, the spin-density parametrization is much more convenient, though, since at $\Lambda \to \infty$, Γ^s is directly proportional to the *spin* interaction J_{ij} from the Hamiltonian and density vertex Γ^d is simply zero. The term "density" vertex is related to the fact that it describes a term proportional to $\delta_{\sigma_{1'}\sigma_1}\delta_{\sigma_{2'}\sigma_2}$ which means that both pseudofermion operators with the same site index (stemming from the same spin operator $\vec{S}_i$) also carry the same spin index. This leads to a term $\propto \underbrace{\hat{c}^\dagger_{i,\alpha}\hat{c}_{i,\alpha}}_{\hat{n}_{i,\alpha}}\underbrace{\hat{c}^\dagger_{j,\beta}\hat{c}_{j,\beta}}_{\hat{n}_{j,\beta}}$ which describes an effective density-density interaction.

C Derivation of Parametrized Bubble Functions in the t- and a-Channel

Bubbles in the t-channel
This procedure of determining the combinatorial factors can be used in all three channels. In the t-channel, the bubble is defined as:

$$B_t(\Gamma,\Gamma')_{\hat{1}'\hat{2}',\hat{1}\hat{2}} = -\sum_{\hat{3}\hat{2}} \Gamma(\hat{4}\hat{2}',\hat{3}\hat{2})\Gamma'(\hat{1}'\hat{3},\hat{1}\hat{4})G^\Lambda(\omega_3)G^\Lambda(\omega_4).$$

In this definition, a factor of (-1) is included which reflects the crossing symmetry between the a-channel and the t-channel. With the inclusion of this minus sign, the flow equation for the vertex

becomes simply the sum of the Λ-derivatives of all three bubbles without any additional signs. Using this definition, the site-parametrization yields:

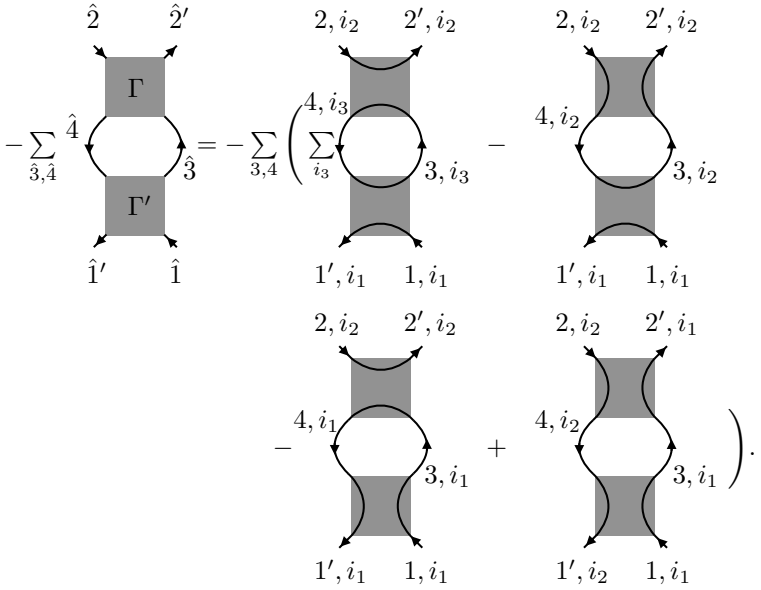

By inspection, it is clear that the first three diagrams belong to the proportionality class $\delta_{i_1 i_{1'}} \delta_{i_2 i_{2'}}$ whereas only the fourth one connects the lattice sites differently.
Inserting the spin-parametrized vertices, one obtains for the three individual contributions:

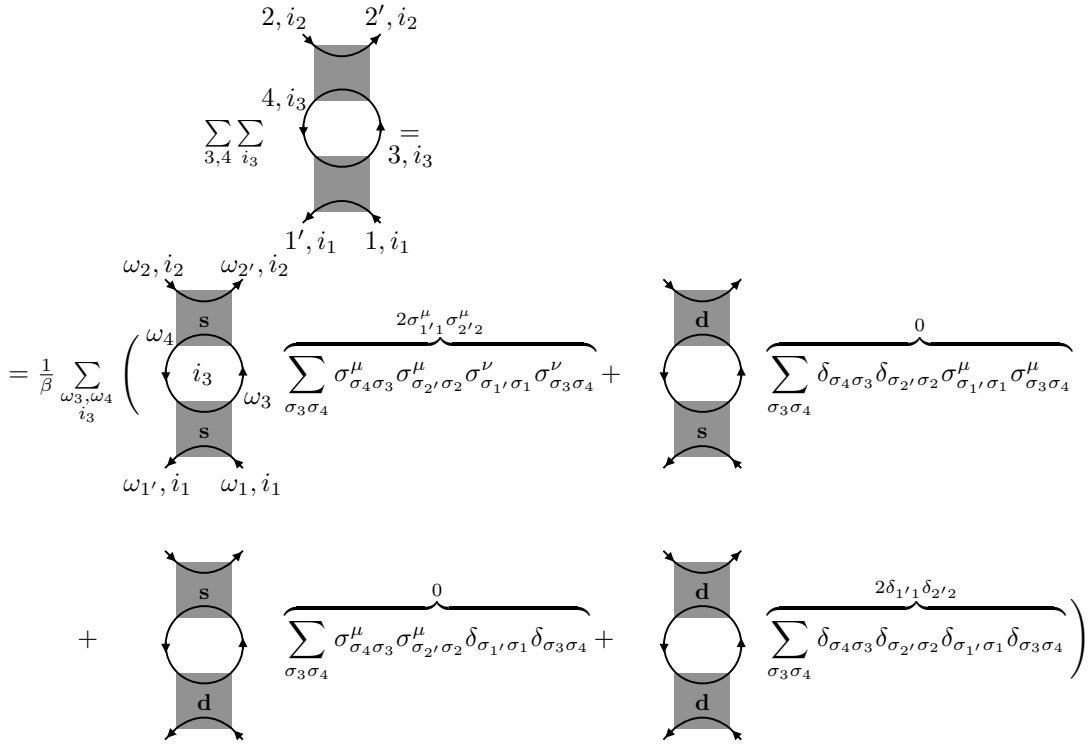

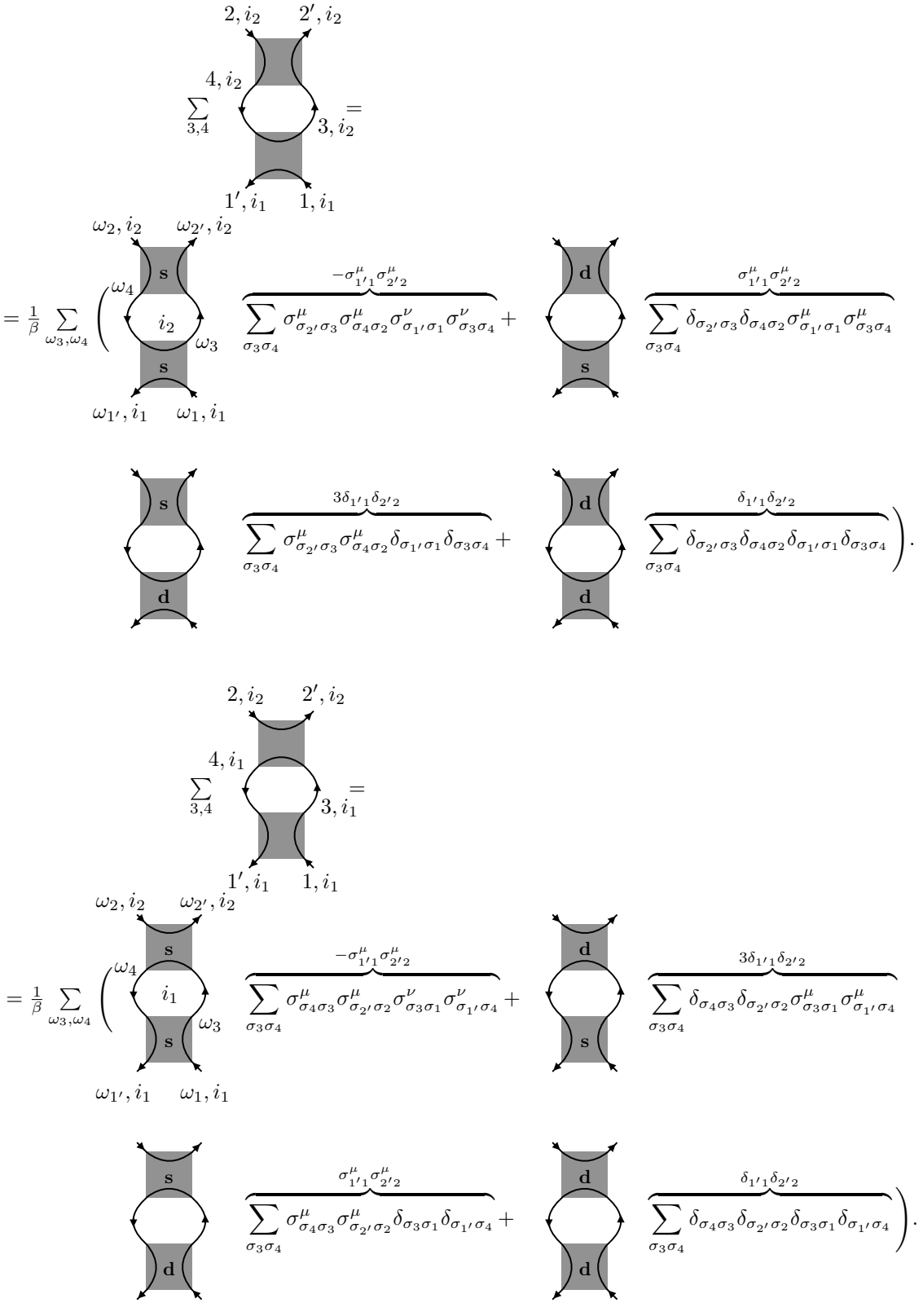

The resulting effective rule for the terms proportional to $\delta_{i_1 i_{1'}} \delta_{i_2 i_{12}}$ in bubbles of the t-channel is depicted in Fig. 25.

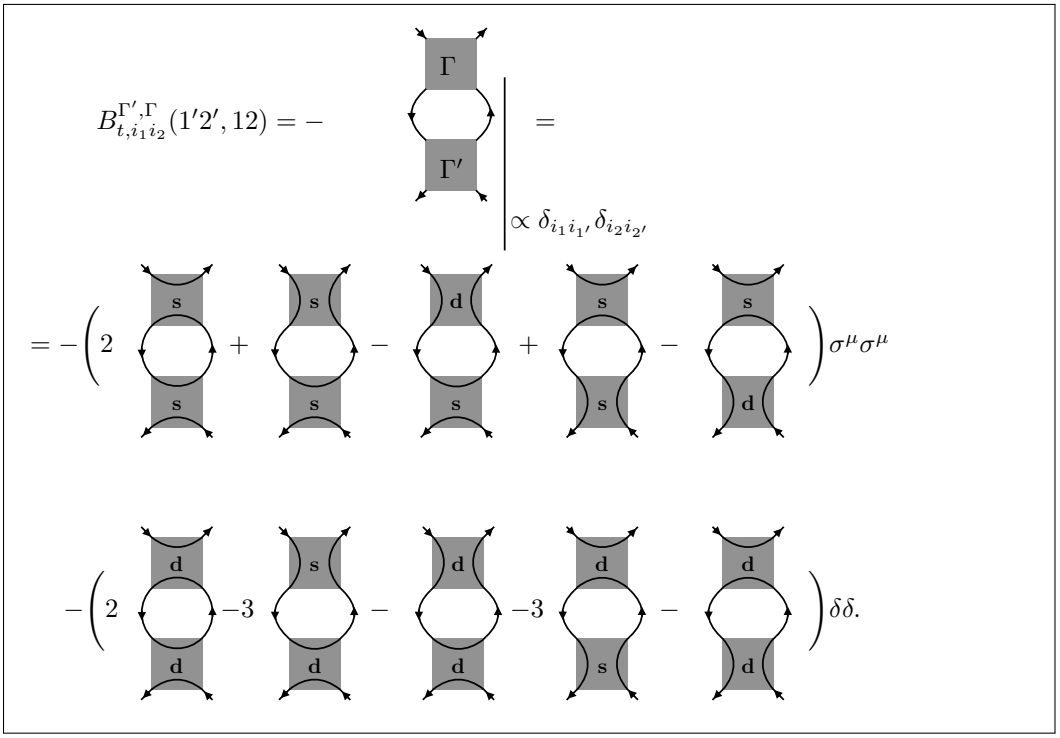

Fig. 25: Effective rule for bubbles in the t-channel.

In terms of mathematical objects it reads:

$$
\begin{aligned}
B^{\Gamma,\Gamma'}_{t,i_1i_2}(1'2',12) = -\frac{1}{\beta}\sum_{\omega_3,\omega_4} G(\omega_3)G(\omega_4)\Bigg\{ &\Big(2\cdot\sum_{i_3}\Gamma^s_{i_3i_2}(\omega_4\omega_{2'};\omega_3\omega_2)\Gamma'^s_{i_1i_3}(\omega_{1'}\omega_3;\omega_1\omega_4)\\
&+\tilde\Gamma^s_{i_2i_2}(\omega_{2'}\omega_4;\omega_3\omega_2)\Gamma'^s_{i_1i_2}(\omega_{1'}\omega_3;\omega_1\omega_4) - \tilde\Gamma^d_{i_2i_2}(\omega_{2'}\omega_4;\omega_3\omega_2)\Gamma'^s_{i_1i_2}(\omega_{1'}\omega_3;\omega_1\omega_4)\\
&+\Gamma^s_{i_1i_2}(\omega_4\omega_{2'};\omega_3\omega_2)\tilde\Gamma'^s_{i_1i_1}(\omega_3\omega_{1'};\omega_1\omega_4) - \Gamma^s_{i_1i_2}(\omega_4\omega_{2'};\omega_3\omega_2)\tilde\Gamma'^d_{i_1i_1}(\omega_3\omega_{1'};\omega_1\omega_4)\Big)\sigma^\mu_{\sigma_{1'}\sigma_1}\sigma^\mu_{\sigma_{2'}\sigma_2}\\
&+\Big(2\cdot\sum_{i_3}\Gamma^d_{i_3i_2}(\omega_4\omega_{2'};\omega_3\omega_2)\Gamma'^d_{i_1i_3}(\omega'_1\omega_3;\omega_1\omega_4)\\
&-3\cdot\tilde\Gamma^s_{i_2i_2}(\omega_{2'}\omega_4;\omega_3\omega_2)\Gamma'^d_{i_1i_2}(\omega_{1'}\omega_3;\omega_1\omega_4) - \tilde\Gamma'^d_{i_2i_2}(\omega_{2'}\omega_4;\omega_3\omega_2)\Gamma^d_{i_1i_2}(\omega_{1'}\omega_3;\omega_1\omega_4)\\
&-3\cdot\Gamma^d_{i_1i_2}(\omega_4\omega_{2'};\omega_3\omega_2)\tilde\Gamma'^s_{i_1i_1}(\omega_3\omega_{1'};\omega_1\omega_4) - \Gamma^d_{i_1i_2}(\omega_4\omega_{2'};\omega_3\omega_2)\tilde\Gamma'^d_{i_1i_1}(\omega_3\omega_{1'};\omega_1\omega_4)\Big)\delta_{\sigma_{1'}\sigma_1}\delta_{\sigma_{2'}\sigma_2}\Bigg\}.
\end{aligned}
\tag{75}
$$

The first three lines are the three different kinds of diagrams that become the new spin vertex and the last three lines are the three different kinds of diagrams forming the new density vertex.

Bubbles in the a-channel

Bubbles in the a-channel are defined as:

$$B_a(\Gamma,\Gamma')_{\hat 1'\hat 2',\hat 1\hat 2} = \sum_{\hat 3\hat 4}\Gamma(\hat 1'\hat 4,\hat 3\hat 2)\Gamma'(\hat 3\hat 2',\hat 1\hat 4)G^\Lambda(\omega_3)G^\Lambda(\omega_4).$$

Straightforwardly employing the real space parametrization yields:

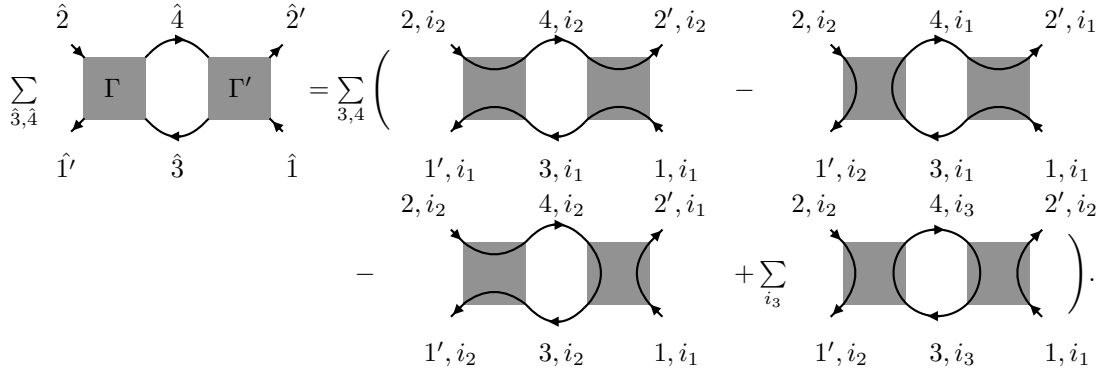

Note that the diagrams of the a-channel are related to those of the t-channel by crossing symmetry, e.g. by the exchange of two ingoing legs. Also the real space parametrization introduced above is nothing but an explicit implementation of the fermionic anti-symmetry under the exchange of two ingoing legs. Knowing that three of the four diagrams in the t-channel belong to the proportionality class $\delta_{i_1 i_2}\delta_{i_{1'} i_{2'}}$, it is intuitive that there is only one "remaining" site-resolved bubble diagram in the a-channel that is proportional to $\delta_{i_1 i_2}\delta_{i_{1'} i_{2'}}$. Inserting the spin parametrization leads to:

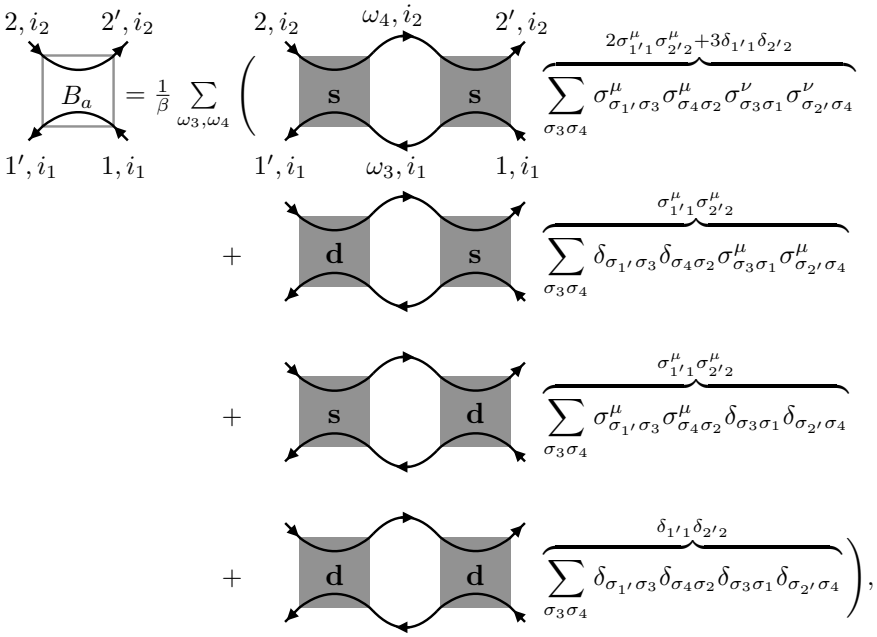

Thus, one can derive the effective rule for general bubble functions in the a-channel as shown in Fig. 26.

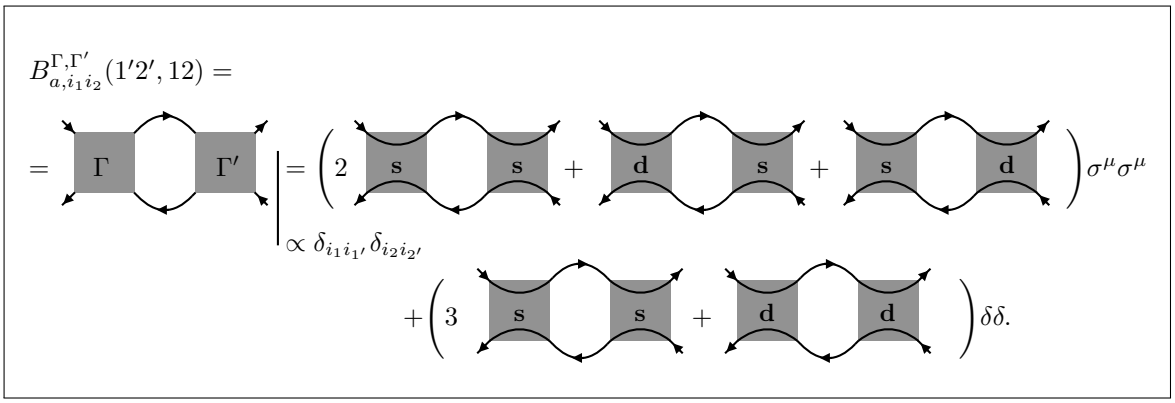

Fig. 26: Effective rule for bubbles in the a-channel.

In full mathematical detail, this corresponds to:

$$B^{\Gamma,\Gamma'}_{a,i_1i_2}(1'2',12) = \frac{1}{\beta}\sum_{\omega_3,\omega_4} G(\omega_3)G(\omega_4) \times \Big\{ \Big(2\cdot\Gamma^s_{i_1i_2}(\omega_{1'}\omega_4;\omega_3\omega_2)\Gamma'^s_{i_1i_2}(\omega_3\omega_{2'};\omega_1\omega_4)$$
$$+\Gamma^d_{i_1i_2}(\omega_{1'}\omega_4;\omega_3\omega_2)\Gamma'^s_{i_1i_2}(\omega_3\omega_{2'};\omega_1\omega_4)+\Gamma^s_{i_1i_2}(\omega_{1'}\omega_4;\omega_3\omega_2)\Gamma'^d_{i_1i_2}(\omega_3\omega_{2'};\omega_1\omega_4)\Big)\sigma^\mu_{\sigma_{1'}\sigma_1}\sigma^\mu_{\sigma_{2'}\sigma_2}$$
$$+\Big(3\cdot\Gamma^s_{i_1i_2}(\omega_{1'}\omega_4;\omega_3\omega_2)\Gamma'^s_{i_1i_2}(\omega_3\omega_{2'};\omega_1\omega_4)+\Gamma^d_{i_1i_2}(\omega_{1'}\omega_4;\omega_3\omega_2)\Gamma'^d_{i_1i_2}(\omega_3\omega_{2'};\omega_1\omega_4)\Big)\delta_{\sigma_{1'}\sigma_1}\delta_{\sigma_{2'}\sigma_2}\Big\}. \tag{76}$$

D Numerical Consistency Checks

There are multiple tests that can be used to ensure self consistency and accuracy of the numerical results. One of these tests consists of computing the fRG flow separately in the different channels with bare propagators at every step of the flow. The RPA diagrams that are produced in this scheme can be compared to analytical results in the following manner:
It is straight forward to compute the polarization function $\chi_r(i\Omega)$ in the discrete Matsubara formalism. Since the Hamiltonian lacks a kinetic term, the result is particularly simple, e.g. in the case of the a/t-channel:

$$\chi_{a/t}(i\Omega_m) = \frac{1}{\beta}\sum_{\omega_n}\frac{1}{i\omega_n+\mu}\frac{1}{i(\omega_n+\Omega_m)+\mu} = \frac{-1}{4T}\delta_{\Omega_m,0}. \tag{77}$$

In the p-channel, the polarization function is given by:

$$\chi_p(i\Omega_m) = \frac{1}{\beta}\sum_{\omega_n}\frac{1}{i\omega_n+\mu}\frac{1}{i(-\omega_n+\Omega_m)+\mu} = \frac{1}{4T}\delta_{\Omega_m,0}. \tag{78}$$

Since in this formalism, the temperature can be interpreted as a low-energy cutoff similarly to Λ in the fRG flow, one can make a one-to-one correspondence between Λ and the temperature T. To identify the conversion factor, one can compute $\chi_r(\Omega)$ at $T=0$ in the sharp cutoff scheme. For the a/t-channel:

$$\chi_a(\Omega) = \frac{1}{2\pi}\int_{-\infty}^{\infty} d\omega \frac{\Theta(|\omega|-\Lambda)\Theta(|\omega+\Omega|-\Lambda)}{i\omega\cdot i(\omega+\Omega)} = \begin{cases} \frac{-1}{\pi|\Omega|}\log\Big(1+\frac{|\Omega|}{\Lambda}\Big) & \text{for } \Omega\neq 0 \\ \frac{-1}{\pi\Lambda} & \text{for } \Omega = 0, \end{cases} \tag{79}$$

and in the p-channel:

$$\chi_p(\Omega) = \frac{1}{2\pi}\int_{-\infty}^{\infty} d\omega \frac{\Theta(|\omega|-\Lambda)\Theta(|-\omega+\Omega|-\Lambda)}{i\omega\cdot i(-\omega+\Omega)} = \begin{cases} \frac{1}{\pi|\Omega|}\log\Big(1+\frac{|\Omega|}{\Lambda}\Big) & \text{for } \Omega\neq 0 \\ \frac{1}{\pi\Lambda} & \text{for } \Omega = 0. \end{cases} \tag{80}$$

As opposed to $\chi_a(i\Omega_m)$ in Eq. (77) which is zero for $\Omega \neq 0$, this function decays slowly on both sides as $|\Omega|$ is increased. However, one can observe that the dependence on the cutoff parameter is equivalent in both functions at $\Omega = 0$ such that one can make the identification:

$$\Lambda = \frac{4T}{\pi}.$$

In the a- and p-channel where the bubble functions do not include summations over site indices, this allows to compute the RPA-result analytically at $\Omega = 0$ for any Λ during the flow. Reducing the considerations to only the spin-part of the vertices, this yields:

$$\Gamma^{\Lambda,\mathrm{RPA}}_{r,i_1i_2}(\Omega_r = 0) = \Gamma^0_{i_1i_2} + \Gamma^0_{i_1i_2} \cdot \chi^\Lambda_r(0) \cdot \Gamma^{\Lambda,\mathrm{RPA}}_{r,i_1i_2}(\Omega_r = 0) \tag{81}$$

$$= \frac{\Gamma^0_{i_1i_2}}{1 - \Gamma^0_{i_1i_2} \cdot \chi^\Lambda_r(0)}, \tag{82}$$

where no fermionic frequency arguments appear since all constituents belong to the diagrammatic classes Λ_{irr} or K^Ω_{1,r,i_1i_2}. Inserting $\chi^\Lambda_r(0)$ from Eq. (79) as function of the flow parameter $\Lambda = \frac{4T}{\pi}$, yields an analytic expression for the flow of RPA-diagrams in the a- and p-channel. Observing that the second summand in Eq. (81) is proportional to $K^{\Lambda,\Omega=0}_{1,r,i_1i_2}$, one can check that the following equivalence holds within the range of validity of the geometric series (i.e. $|\Gamma^0_{i_1i_2} \cdot \chi^\Lambda_r(0)| < 1$):

$$K^{\Lambda,\Omega=0}_{1,r,i_1i_2} = \frac{\Gamma^0_{i_1i_2}}{1 - \Gamma^0_{i_1i_2} \cdot \chi^\Lambda_r(0)} - \Gamma^0_{i_1i_2} = \frac{\Gamma^0_{i_1i_2}}{1 - (-2) \cdot \Gamma^0_{i_1i_2} \cdot \frac{1}{\pi\Lambda}} - \Gamma^0_{i_1i_2}, \tag{83}$$

where the left hand side is obtained by reading out the values of $K^{\Lambda,\Omega=0}_{1,r,i_1i_2}$ during the flow, the term in the middle is obtained by plugging in the numerically computed value of a bare bubble at Λ and the right term is computed purely analytically. The factor (-2) in the right term of Eq. (83) stems from the combinatorial factors that appear in the a- and p-channel where the signs are such that the above result is valid in both channels. Note that accurate results can only be obtained if the initial Λ is chosen big enough or if one computes the initial condition for $K^{\Lambda,\Omega=0}_{1,r,i_1i_2}$ analytically at $\Lambda = \Lambda_{\mathrm{init}}$. Moreover, it is important to remark that Eq. (83) holds only if one sets all density interactions to zero which corresponds to spinless particles.

Another precision and consistency test for spinless particles (with all density parts of the vertices set to zero) consists of setting $J_{ij} = J$ for all (i, j) and checking that

$0 =$ 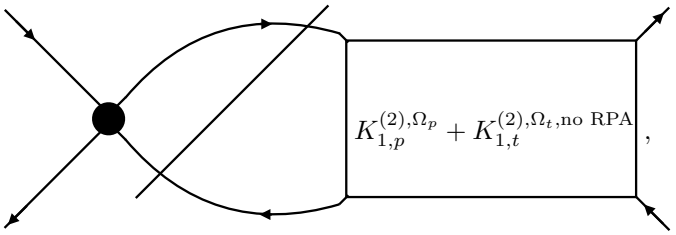

,

where the diagonal line represent the Λ-derivative of the propagators with the Leibniz rule. The vertex functions $K^{(2),\Omega_p}_{1,p}$ and $K^{(2),\Omega_t,\text{no RPA}}_{1,t}$ are computed at lowest order, i.e. at second order in the bare interaction and the term with the site-summation from the t-channel diagramm is left out. The bosonic frequencies Ω_p and Ω_t depend on the a-channel-frequency arguments and can be computed by making use of the conversion table. This identity holds only since the interaction is local and only if particle-hole symmetry is present, such that $G(i\omega) = -G(-i\omega)$, as can be seen by translating

this diagram to an analytic expression with the sharp regulator, i.e.

$$\begin{aligned}\propto \Big\{ & S(-\Lambda)G(-\Lambda+\Omega_a)(K_{1,p}^{\omega-\Lambda+\frac{\Omega_a}{2}} + K_{1,t}^{-\omega-\Lambda+\frac{\Omega_a}{2}}) \\ & +S(\Lambda)G(\Lambda+\Omega_a)(K_{1,p}^{\omega+\Lambda+\frac{\Omega_a}{2}} + K_{1,t}^{-\omega+\Lambda+\frac{\Omega_a}{2}}) \\ & +G(-\Lambda-\Omega_a)S(-\Lambda)(K_{1,p}^{\omega-\Lambda-\frac{\Omega_a}{2}} + K_{1,t}^{-\omega-\Lambda-\frac{\Omega_a}{2}}) \\ & +G(\Lambda-\Omega_a)S(\Lambda)(K_{1,p}^{\omega+\Lambda-\frac{\Omega_a}{2}} + K_{1,t}^{-\omega+\Lambda-\frac{\Omega_a}{2}}) \Big\},\end{aligned}$$

where we have suppressed in the notation that the K_r diagrams refer to the lowest order and that the RPA-contribution from the t-channel is neglected.

Making use of the identity $K_{1,p}^{(2),\Omega_p} = K_{1,p}^{(2),-\Omega_p} = -K_{1,t}^{(2),-\Omega_p,\text{no RPA}}$ (for the site-independent interaction J), one sees that the first and the last line, as well as the second and third line cancel out pairwise. Exactly the same test can be made for this fish-eye-like diagram in the p-channel in which case one deals with K_a instead of K_p.

References

[1] P. Anderson. Resonating valence bonds: A new kind of insulator? *Materials Research Bulletin*, 8(2):153 – 160, 1973.

[2] L. Balents. Spin liquids in frustrated magnets. *Nature*, 464:199 EP –, 03 2010.

[3] J. Berges, N. Tetradis, and C. Wetterich. Non-perturbative renormalization flow in quantum field theory and statistical physics. *Physical Review B*, 363(4-6):223–386, Jun 2002.

[4] N. E. Bickers and S. R. White. Conserving approximations for strongly fluctuating electron systems. ii. numerical results and parquet extension. *Phys. Rev. B*, 43:8044–8064, Apr 1991.

[5] F. L. Buessen and S. Trebst. Competing magnetic orders and spin liquids in two- and three-dimensional kagome systems: Pseudofermion functional renormalization group perspective. *Phys. Rev. B*, 94:235138, Dec 2016.

[6] S. Depenbrock, I. P. McCulloch, and U. Schollwöck. Nature of the spin-liquid ground state of the $s = 1/2$ heisenberg model on the kagome lattice. *Phys. Rev. Lett.*, 109:067201, Aug 2012.

[7] J.-C. Domenge, P. Sindzingre, C. Lhuillier, and L. Pierre. Twelve sublattice ordered phase in the $J_1 - J_2$ model on the kagomé lattice. *Phys. Rev. B*, 72:024433, Jul 2005.

[8] A. Eberlein. Fermionic two-loop functional renormalization group for correlated fermions: Method and application to the attractive hubbard model. *Phys. Rev. B*, 90:115125, Sep 2014.

[9] T. Enss, V. Meden, S. Andergassen, X. Barnabé-Thériault, W. Metzner, and K. Schönhammer. Impurity and correlation effects on transport in one-dimensional quantum wires. *Phys. Rev. B*, 71:155401, Apr 2005.

[10] T. Han, S. Chu, and Y. S. Lee. Refining the spin hamiltonian in the spin-$\frac{1}{2}$ kagome lattice antiferromagnet $\mathrm{zncu_3(OH)_6cl_2}$ using single crystals. *Phys. Rev. Lett.*, 108:157202, Apr 2012.

[11] Y.-C. He, M. P. Zaletel, M. Oshikawa, and F. Pollmann. Signatures of dirac cones in a dmrg study of the kagome heisenberg model. *Phys. Rev. X*, 7:031020, Jul 2017.

[12] M. Hermele, Y. Ran, P. A. Lee, and X.-G. Wen. Properties of an algebraic spin liquid on the kagome lattice. *Phys. Rev. B*, 77:224413, Jun 2008.

[13] Y. Huh, M. Punk, and S. Sachdev. Vison states and confinement transitions of $\mathbb{z}_2$ spin liquids on the kagome lattice. *Phys. Rev. B*, 84:094419, Sep 2011.

[14] Y. Iqbal, F. Becca, S. Sorella, and D. Poilblanc. Gapless spin-liquid phase in the kagome spin-$\frac{1}{2}$ heisenberg antiferromagnet. *Phys. Rev. B*, 87:060405, Feb 2013.

[15] Y. Iqbal, T. Müller, P. Ghosh, M. J. P. Gingras, H. O. Jeschke, S. Rachel, J. Reuther, and R. Thomale. Quantum and classical phases of the pyrochlore heisenberg model with competing interactions. *Phys. Rev. X*, 9:011005, Jan 2019.

[16] Y. Iqbal, R. Thomale, F. Parisen Toldin, S. Rachel, and J. Reuther. Functional renormalization group for three-dimensional quantum magnetism. *Phys. Rev. B*, 94:140408, Oct 2016.

[17] H. C. Jiang, Z. Y. Weng, and D. N. Sheng. Density matrix renormalization group numerical study of the kagome antiferromagnet. *Phys. Rev. Lett.*, 101:117203, Sep 2008.

[18] C. Karrasch. *The functional renormalization group for zero-dimensional quantum systems in and out of equilibrium.* PhD thesis, RWTH Aachen, 2010.

[19] A. A. Katanin. Fulfillment of ward identities in the functional renormalization group approach. *Phys. Rev. B*, 70:115109, Sep 2004.

[20] F. Kolley, S. Depenbrock, I. P. McCulloch, U. Schollwöck, and V. Alba. Phase diagram of the J_1-J_2 heisenberg model on the kagome lattice. *Phys. Rev. B*, 91:104418, Mar 2015.

[21] P. Kopietz, L. Bartosch, and F. Schütz. *Introduction to the Functional Renormalization Group*. Introduction to the Functional Renormalization Group. Springer, 2010.

[22] F. B. Kugler and J. von Delft. Derivation of exact flow equations from the self-consistent parquet relations. *New Journal of Physics*, 20(12):123029, Dec 2018.

[23] F. B. Kugler and J. von Delft. Multiloop functional renormalization group for general models. *Phys. Rev. B*, 97:035162, Jan 2018.

[24] F. B. Kugler and J. von Delft. Multiloop functional renormalization group that sums up all parquet diagrams. *Phys. Rev. Lett.*, 120:057403, Jan 2018.

[25] P. A. Lee. From high temperature superconductivity to quantum spin liquid: progress in strong correlation physics. *Reports on Progress in Physics*, 71(1):012501, dec 2007.

[26] J. B. Marston and C. Zeng. Spin-peierls and spin-liquid phases of kagomé quantum antiferromagnets. *Journal of Applied Physics*, 69(8):5962–5964, 1991.

[27] P. Mendels and F. Bert. Quantum kagome frustrated antiferromagnets: One route to quantum spin liquids. *Comptes Rendus Physique*, 17(3):455 – 470, 2016.

[28] L. Messio, S. Bieri, C. Lhuillier, and B. Bernu. Chiral spin liquid on a kagome antiferromagnet induced by the dzyaloshinskii-moriya interaction. *Phys. Rev. Lett.*, 118:267201, Jun 2017.

[29] W. Metzner, M. Salmhofer, C. Honerkamp, V. Meden, and K. Schönhammer. Functional renormalization group approach to correlated fermion systems. *Rev. Mod. Phys.*, 84:299–352, Mar 2012.

[30] F. Mila. Quantum spin liquids. *European Journal of Physics*, 21(6):499–510, nov 2000.

[31] G. Misguich. Quantum spin liquids. *arXiv e-prints*, page arXiv:0809.2257, Sep 2008.

[32] G. Misguich, D. Serban, and V. Pasquier. Quantum dimer model on the kagome lattice: Solvable dimer-liquid and ising gauge theory. *Phys. Rev. Lett.*, 89:137202, Sep 2002.

[33] M. Punk. Lecture notes in: Condensed matter field theory. Ludwig-Maximilians-Universität München, 2016/17.

[34] M. Punk. Lecture notes in: Topology in condensed matter physics. Ludwig-Maximilians-Universität München, 2017.

[35] M. Punk, D. Chowdhury, and S. Sachdev. Topological excitations and the dynamic structure factor of spin liquids on the kagome lattice. *Nature Physics*, 10(4):289–293, mar 2014.

[36] J. Reuther. *Frustrated Quantum Heisenberg Antiferromagnets: Functional Renormalization-Group Approach in Auxiliary-Fermion Representation*. PhD thesis, Karlsruher Instituts für Technologie, 2011.

[37] J. Reuther and R. Thomale. Functional renormalization group for the anisotropic triangular antiferromagnet. *Phys. Rev. B*, 83:024402, Jan 2011.

[38] J. Reuther, R. Thomale, and S. Trebst. Finite-temperature phase diagram of the heisenberg-kitaev model. *Phys. Rev. B*, 84:100406, Sep 2011.

[39] J. Reuther and P. Wölfle. J_1-J_2 frustrated two-dimensional heisenberg model: Random phase approximation and functional renormalization group. *Phys. Rev. B*, 81:144410, Apr 2010.

[40] G. Rohringer. *New routes towards a theoretical treatment of nonlocal electronic correlations*. PhD thesis, Vienna University of Technology, 2013.

[41] G. Rohringer, H. Hafermann, A. Toschi, A. A. Katanin, A. E. Antipov, M. I. Katsnelson, A. I. Lichtenstein, A. N. Rubtsov, and K. Held. Diagrammatic routes to nonlocal correlations beyond dynamical mean field theory. *Rev. Mod. Phys.*, 90:025003, May 2018.

[42] M. Rück and J. Reuther. Effects of two-loop contributions in the pseudofermion functional renormalization group method for quantum spin systems. *Phys. Rev. B*, 97:144404, Apr 2018.

[43] S. Sachdev. Kagome- and triangular-lattice heisenberg antiferromagnets: Ordering from quantum fluctuations and quantum-disordered ground states with unconfined bosonic spinons. *Phys. Rev. B*, 45:12377–12396, Jun 1992.

[44] S. Sachdev. Quantum magnetism and criticality. *Nature Physics*, 4:173 EP –, 03 2008.

[45] S. Sachdev. *Quantum Phase Transitions*. Cambridge University Press, 2 edition, 2011.

[46] M. P. Shores, E. A. Nytko, B. M. Bartlett, and D. G. Nocera. A Structurally Perfect S = 1/2 Kagomé Antiferromagnet. *Journal of the American Chemical Society*, 127(39):13462–13463, 2005. doi: 10.1021/ja053891p.

[47] R. Suttner, C. Platt, J. Reuther, and R. Thomale. Renormalization group analysis of competing quantum phases in the J_1-J_2 heisenberg model on the kagome lattice. *Phys. Rev. B*, 89:020408, Jan 2014.

[48] A. Tagliavini, C. Hille, F. B. Kugler, S. Andergassen, A. Toschi, and C. Honerkamp. Multiloop functional renormalization group for the two-dimensional Hubbard model: Loop convergence of the response functions. *SciPost Phys.*, 6:9, 2019.

[49] C. Taranto, S. Andergassen, J. Bauer, K. Held, A. Katanin, W. Metzner, G. Rohringer, and A. Toschi. From infinite to two dimensions through the functional renormalization group. *Phys. Rev. Lett.*, 112:196402, May 2014.

[50] F. Wang and A. Vishwanath. Spin-liquid states on the triangular and kagomé lattices: A projective-symmetry-group analysis of schwinger boson states. *Phys. Rev. B*, 74:174423, Nov 2006.

[51] X.-G. Wen. Mean-field theory of spin-liquid states with finite energy gap and topological orders. *Phys. Rev. B*, 44:2664–2672, Aug 1991.

[52] X.-G. Wen. Quantum orders and symmetric spin liquids. *Phys. Rev. B*, 65:165113, Apr 2002.

[53] X.-G. Wen. *Quantum Field Theory of Many-Body Systems:From the Origin of Sound to an Origin of Light and Electrons*. Oxford Graduate Texts. OUP Oxford, 2004.

[54] N. Wentzell, G. Li, A. Tagliavini, C. Taranto, G. Rohringer, K. Held, A. Toschi, and S. Andergassen. High-frequency asymptotics of the vertex function: diagrammatic parametrization and algorithmic implementation. *arXiv e-prints*, page arXiv:1610.06520, Oct 2016.

[55] S. Yan, D. A. Huse, and S. R. White. Spin-liquid ground state of the s = 1/2 kagome heisenberg antiferromagnet. *Science*, 332(6034):1173–1176, 2011.

7 Eigenständigkeitserklärung

Hiermit erkläre ich, die vorliegende Arbeit selbständig verfasst zu haben und keine anderen als die in der Arbeit angegebenen Quellen und Hilfsmittel benutzt zu haben.

München, den 12. September 2019